Design of non conventional Synchronous Reluctance machine

Publisher copyright

(Article begins on next page)

04 August 2020

Politecnico di Torino

Doctoral Thesis

Design of non conventional Synchronous Reluctance machine

Author:
Matteo Gamba

Supervisor:
Prof. Gianmario Pellegrino,
Prof. Alfredo Vagati

A thesis submitted in fulfillment of the requirements
for the degree of Electrical Engineer

in the

Politecnico di Torino Department of Energy
DENERG

Contents

Dedicated to my Parents...

Chapter 1

Motivation and Content

Synchronous reluctance (SyR) and Permanent magnet Synchronous Reluctance (PM-SyR) machines represent an answer to the growing emphasis on higher efficiency, higher torque density and overload capability of ac machines for variable-speed applications. Their high performance is particularly attractive in electric traction and industry applications. The content of the Thesis is summarized here in the form of key questions initially posed by this field of research, and of the answers that the Thesis gives to such questions. The content of the Thesis is also graphically summarized in Fig.1.1.

1.1 Developed Design Tool: SyRE

SyRE is an open source software, that permits the design of SyR motors and PM-SyR motors with the help of optimization strategies that use genetic algorithms. The key goals of SyRE are:

- Helping non-expert designers;

- Permitting the design of non-conventional motors, not yet covered by comprehensive design equations.

I personally contributed to the definition and implementation of different rotor geometries in SyRE, and to the routines for FEA evaluation of the motor designs, used to evaluate the performance of optimal machines or manual designs. This part is treated in Chapter 6. Examples of non conventional motor designs are presented: Fractional Slot Winding (FSW) SyR motors (Chapter 7) and PM-SyR with mild-overlapped windings (Chapter 8).

1.2 SyR and PM-SyR motors with Super-Premium Efficiency

The SyR technology represents a convenient solution to obtain high efficiency machines at reduced cost and high reliability. The manufacturing costs are comparable to other existing technologies such as induction motors. Different SyR and PM-SyR machines with different ratings and applications were designed, for comparison with induction motors having equal frame. An accurate comparison between Induction motors, SyR and PM-SyR machines is reported, with reference to the IE4 and IE5 efficiency specifications that could become mandatory in the next years.

1.3 Design of Traction motor for urban mobility: the THOR Project

First of all, the traction motor of the Toyota Prius 2010 is presented and used as benchmark for the field of traction motors. PM-SyR machines are compared to the benchmark using design equations and FEA. A mathematical approach of general validity is proposed and FEA validated. Last, a Ferrite-SyR motor for a light quadricycle was designed, prototyped and tested. This activity was part of the regional project THOR (POR FESR 2007/2013).

1.4 Non-Conventional SyR motors

Three studies are classified under the term "*Non-Conventional*" machines:

- *Line-Start SyR motor*: is a special SyR machine designed for constant speed applications, line supplied. The rotor flux barriers are filled with aluminum, to obtain a squirrell cage that resembles the one of an induction motor. The manufacturing costs are comparable to those of the induction motor, and the efficiency is higher. Two prototypes were realized and tested.

- *FSW-SyR*: tooth-wound coils and fractional slot per pole combinations were investigated. They are of interest because they permit a simplification and higher degree of automatization of the manufacturing process. However, FSW-SyR machines are known for their high torque ripple, low specific torque and power factor. The number of slots per pole was optimized to maximize the torque density. Dealing with the torque ripple, a lumped parameters model was used together with optimization in SyRE. A design with minimized ripple was obtained, comparable to a distributed winding machine in this respect. This design was prototyped and tested.

- *Mild Overlapped SyR*: this study shows a new winding configuration applied to SyR and PM-SyR machines. The proposed case is in the direction to find a hybrid solution between distributed winding and tooth winding motors, that permits to reduce costs and improve performances. One limitation of this solution is that only number of pole pairs equal to five or higher are feasible, and this reduces the applicability of the solution to classical industry applications, where one to three pole pairs are normally used.
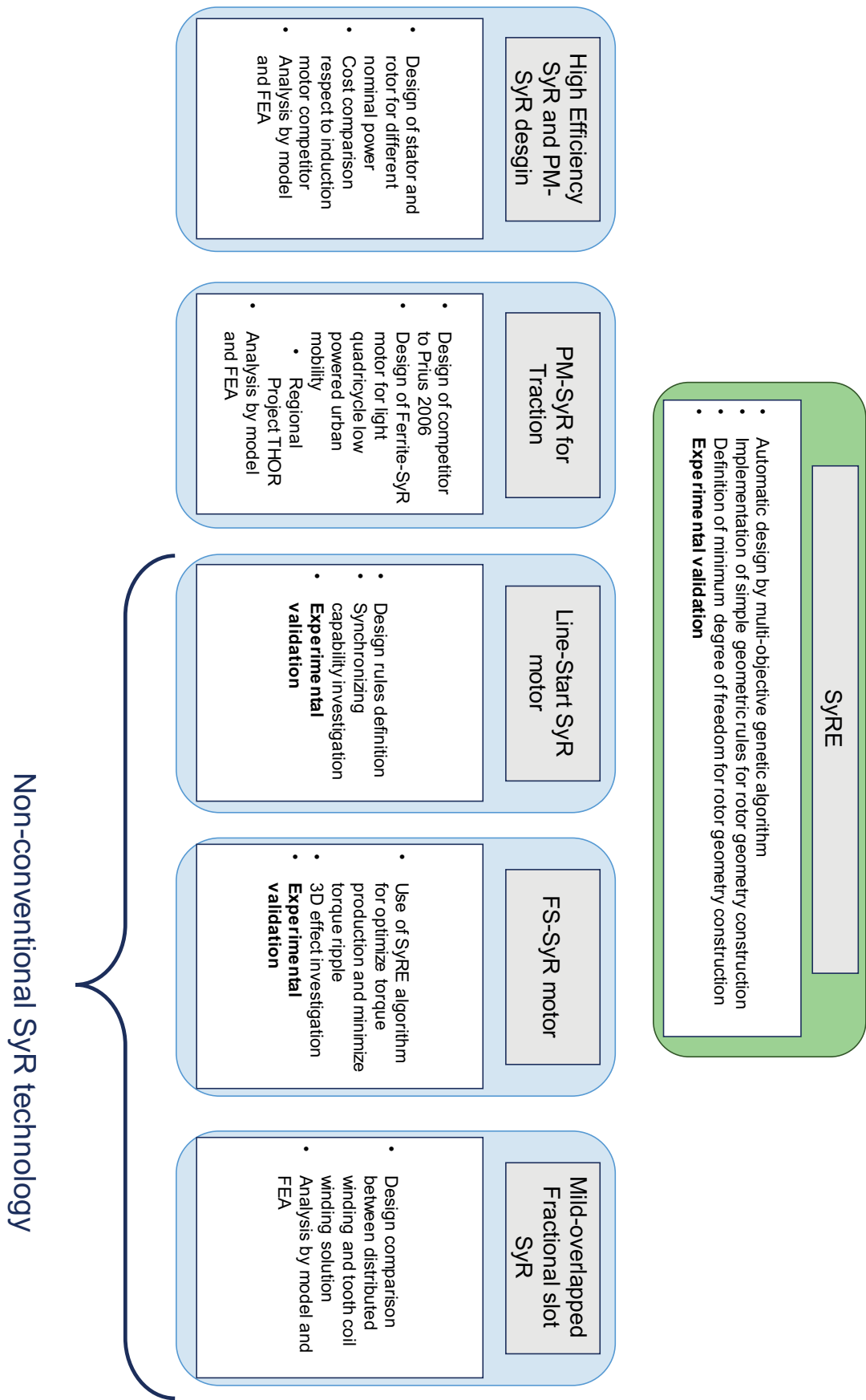
FIGURE 1.1: Block diagram of the PhD Activity

Chapter 2

Design of SyR and PM/Reluctance Machine

2.1 Historical Perspectives on Synchronous Reluctance motors

Synchronous Reluctance machines were discovered many years ago, around the early 60's, even if the theory of anisotropic filed structure go back to the 1923 where Doherty and Nickle published a paper that derived the power/torque versus angle relationship [1], Kusko in 1926 shows a first design of synchronous reluctance motor with multi barriers structure. Honsinger [2] in 1957 developed some of the first consistent theory on the design of multi barrier synchronous reluctance machines. The commercial applications of this motors are for open loop V-Hz solutions in textile industry. Where several of this machines could be operated in synchronism excited in parallel by one inverter. The improvement in the solid state inverter technology leads researchers to the design of variable speed drive machines. Synchronous reluctance motor can represent a viable alternative to the induction motor, especially in the field of sensorless controls. The performances of Synchronous machines were really poor compare to the induction ones. A design campaign, on synchronous reluctance motors is done, in order to improve anisotropy and consequently torque density and efficiency. During this period, the axially laminated solutions were studied. Theoretically, this solutions permit to maximize the magnetic anisotropy of the machine, with benefits on power factor and torque density, but they are quite problematic in terms of iron losses [3]. Vagati [4], presents the design of high performance transversally laminated motors. This solution permits to improve the torque density and power factor with iron losses comparable to an equal size induction motor.

Bianchi in [5], [6] shows an accurate design of the operating limit of SyR technology and the flux weakening (FW) behavior, with attention on the estimation of iron losses in FW conditions.

Synchronous Reluctance with transversally laminated rotor (SyR) is attractive for its robustness, high overload capability and its low cost. The main difference between an IM and SyR motor as shown in Fig.2.1 is on the rotor side. The stator is transversally laminated with distributed winding configuration like in an IM. In many solutions shown in literature [7], in the design of SyR machines are used the same stators of the induction motors. Permanent Magnet Synchronous reluctance motors can simply obtained inserting permanent magnets inside the flux barriers. The resulting configuration is called PM assisted SyR motor (PM-SyR, sometimes PMASR). Other times, in a more general way, It is called Interior Permanent Magnet (IPM) motor.

In [8] is shown that increasing the anisotropy it is possible to reduce the PM flux for achieving a Constant Power Speed Range. This is an important result for PM-SyR motors. If the reluctance component is properly design it is possible the use of weaker magnet like ferrite, with cost benefits. In this direction are also working some Big company like ABB. In [9], it is shown the use of Ferrite Magnet in multi-barrier IPM motors for reach IE5 efficiency class.

Synchronous reluctance machines are generally called cold rotor motors, because they present no Joule losses on the rotor side, this permits with accurate design to improve the efficiency respect to field exited synchronous machines and IMs. In the last five years also some of the great industries in the filed of electric machines and drives: Siemens and ABB, have start to show data-sheet on synchronous reluctance and PM-SyR. The reason for this new attention on synchronous reluctance technology is related to the progressively improvement, in the last years of the efficiency request by IEC (International Electrotechnical Committee). The IE4 (mandatory for machine over 7,5kW) and recently, the IE5 (not mandatory at the moment) that require a reduction of 20% of losses respect to the IE4 impose for market reasons the improvement of the motors performances.
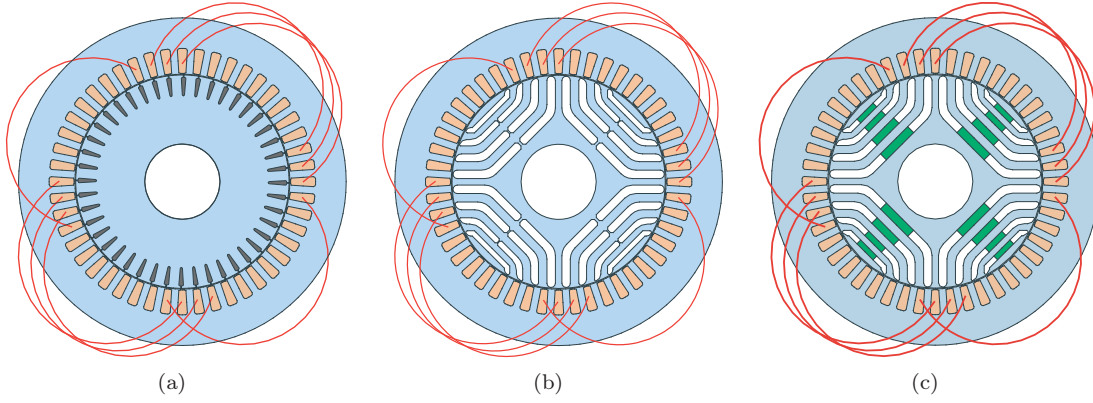
FIGURE 2.1: (a) Sketch of four poles Induction Motor; (b) SyR motor; PM-SyR
motor

2.2   Main design Rules of SyR and PM-SyR machines

2.2.1   Magnetic model and torque

Let us refer to a four pole machine, like the one shown in Fig.2.2. The general theory of reluctance
machines identifies two different rotor paths. One is a lower reluctance path, commonly identified as
d-axis, Fig.2.2a, flux lines flow in the rotor path parallel to the iron flux guide. The other one is a
high reluctance path, usually q-axis, flux lines flows perpendicularly to the flux barriers, Fig.2.2b. The
rotor is commonly designed with several flux barriers in order to obstacle flux flow along the q-axis.
however iron bridges remains, at the airgap and along the q-axis to mechanically sustain the rotor. A
portion of flux flows along this bridges reducing the machine torque production and power factor.
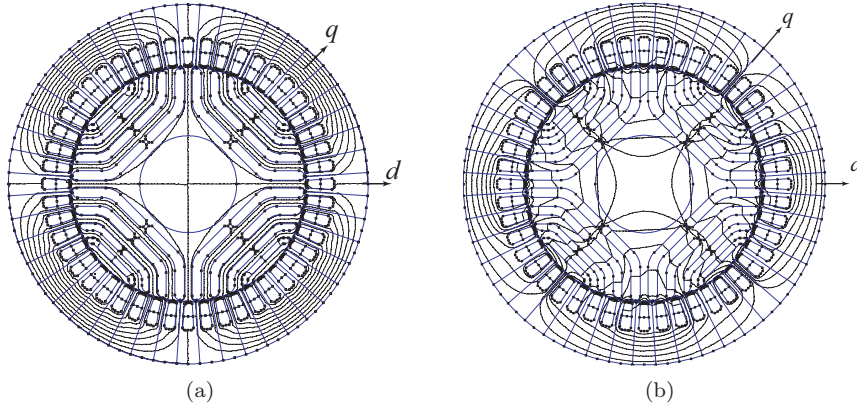
FIGURE 2.2: (a) d axis flux path; (b) q axis flux path

At first, the simple magnetic model of an IPM machine is considered (2.1).

$$\bar{\lambda} = \begin{bmatrix} L_d & 0 \\ 0 & L_q \end{bmatrix} i_{dq} + \begin{bmatrix} \lambda_m \\ 0 \end{bmatrix} = \bar{\lambda}_r + \bar{\lambda}_m \tag{2.1}$$

The flux linkage vector $\bar{\lambda}$ is the superposition of a magnet flux vector $\bar{\lambda}_m$ and a reluctance flux
vector $\bar{\lambda}_r$. Superposition of r and m flux linkages in (2.1) is not exact, due to magnetic saturation. The
simplified model (2.1)-(2.2) is however usefully adopted here for the sake of clarity. All non-ideality
will be included in the design stage. Under such assumptions, electromagnetic torque (2.2) is found,
consisting of a magnet torque component plus a reluctance torque component.

$$T = \frac{3}{2}p\left(\lambda_m i_d + (L_d - L_q)i_d i_q\right). \tag{2.2}$$

In order to maximize the reluctance torque, it is necessary to maximize $L_d - L_q$. About L_d this can be obtained with small airgap, properly design iron yoke and poles number. L_q must be minimized properly design number and size of the flux barriers. In a preliminary way the design procedure of SyR machine can be summarized in the following steps:

- Stack size, cooling & electric current loading;

- stator/ rotor split, core/ copper split;

- rotor optimization;

2.2.2 Design guidelines

The electric loading is set indirectly by the Joule loss per stack outer surface, substituting in (2.3) the current loading definition (2.4), than (2.4) shows the relation between current loading and K_j.

$$K_j = \frac{Joule loss}{stack cylinder surface} = \frac{\frac{3}{2} R_s i_o^2}{2 \pi R L} \tag{2.3}$$

Where R_s is the stator resistance @ rated temperature, i_o the rated current.

$$K_j = \pi \rho \frac{K_{end}}{k_{cu} A_{slots}} x^2 R \left(\frac{A_s}{k_w} \right)^2 \tag{2.4}$$

where $x = r/R$ is the split ratio, A_{slots} is the total slots area, k_{Cu} the net copper / slot area, $K_{end} = \frac{L + L_{end}}{L}$ end winding factor, ρ copper resistivity [Ω m].
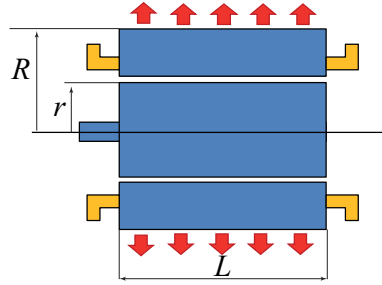
FIGURE 2.3: illustration of K_j meaning

The reason for the choice of the constant K_j is illustrated in Tab.2.1, where it is possible to see that the use of K_j is less stack size dependent, when the machine dimensions change.

TABLE 2.1: Trend in motor quantities as a function of stack dimensions L and D, with different loading assumptions

	J_s [A/mm^2]	K_j [W/m^2]	A_s [A/m]
Stack surface [m^2]	-	$D L$	-
Volume [m^3]	-	$D^2 L$	-
Copper Loss	$J_s^2 D^2 L$	$K_j D L$	$A_s^2 L$
J_s[A/mm^2]	const	$1/\sqrt{D}$	$1/\sqrt{D}$
K_j[W/m^2]	D	const	$1/D$
A_s	D	$\sqrt{D}$	const
Torque [Nm]	$D^3 L$	$D^{2.5} L$	$D^2 L$
TRV [Nm/m^3]	D	$\sqrt{D}$	const
Copper temperature	Grow with D	Const	Decrease with D

The adopted formulation, for the torque estimation is shown Fig.2.4. The use of the magnetic loading permits to express torque and power factor performances, without the introduction of the number of turns. The magnetizing component can be expressed considering the airgap flux density and the saturation level in the iron by (2.5), and by the d axis current loading, that represents the

current component that is necessary to spend for magnetizing the machine. The combination of the
two terms in (2.5) leads to (2.6).

$$\lambda_{md} = 2\, r\, L\, \frac{N_s}{p}\, k_w, b\, B_{fe}; \qquad \lambda_{md} = 2\, \mu_0\, \frac{r^2 L}{g}\, k_w\, \frac{N_s}{p^2}\, A_d \tag{2.5}$$

$$A_d = \frac{\pi}{\mu_0}\, b\, B_{fe} \left(\frac{g}{a} \right) \tag{2.6}$$
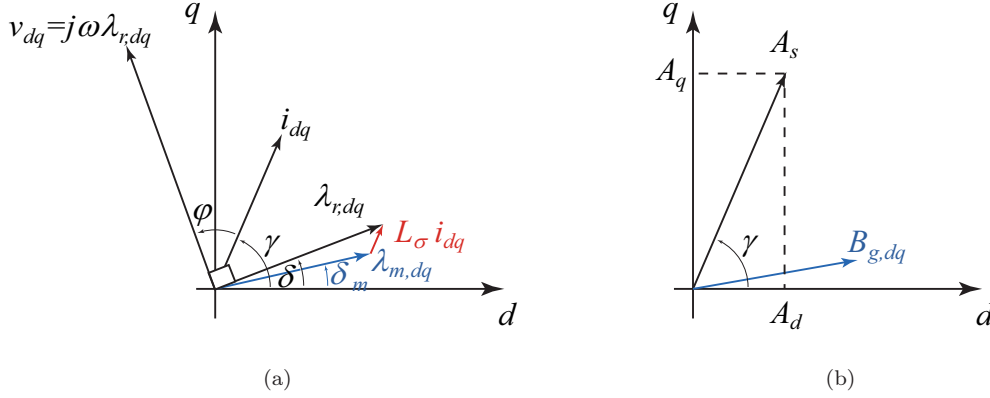
FIGURE 2.4: (a) dq vector diagram in flux linkage ; (b) dq vector diagram in magnetic
loading and current loading

Than the q-axis component responsible of the torque production can be evaluated by the difference
of the A_s evaluated inverting (2.4) and (2.6), $A_q = \sqrt{A_s^2 - A_d^2}$. Torque can be evaluated starting from
the general definition (2.2), no permanent magnets are present at this time, than the torque can be
expressed as in (2.7).

$$T_{syr} = \frac{3}{2}\, p\, \left(L_{md} - L_{mq} \right) i_d\, i_q = \frac{3}{2}\, p \left(1 - \frac{L_{mq}}{L_{md}} \right) L_{md}\, i_d\, i_q = \frac{3}{2}\, p\, K_{dq}\, \lambda_{md}\, i_q \tag{2.7}$$

Where $K_{dq} = 1 - \frac{L_{mq}}{L_{md}}$ is the reluctance torque factor. Than substituting the current loading
definition for i_q and (2.5) for λ_{md} is possible to write the torque in function of the electric and
magnetic loading (2.8). In (2.8) the product $\pi\, r^2\, L$ represents the rotor volume, than the TRV_{syr} in
(2.9) is the torque per rotor volume.

$$T_{syr} = \pi\, r^2 L\, K_{sat}\, K_{dq}\, b\, B_{fe}\, A_q \tag{2.8}$$

where K_{sat} is a iron saturation factor, generally placed equal to 0.7, this takes into account the mmf
drops in the iron.

$$TRV_{syr} = K_{sat}\, K_{dq}\, b\, B_{fe}\, A_q \tag{2.9}$$

Consider the iron ribs in the torque production is quite complicated, if complete formulation is
desired. Only FE Analysis can take into account their effect with the saturation level related to
the working point. For analytic solution it is necessary to solve a complete permeance network (on
q-axis is enough if no cross saturation is considered). The impact of iron ribs can be evaluated with
(2.11). Than considering (2.10) and the current loading definition, after some manipulation (2.11) is
the torque lost in the ribs, function of few geometric parameters and the current loading.

$$\phi_{ribs} = 2\, B_{ribs} S_{ribs}\, L \qquad \Rightarrow \qquad \lambda_{ribs} = 2\, \frac{4}{\pi}\, \frac{k_w N_a}{2p}\, B_r\, w_s\, L \tag{2.10}$$

$$T_{ribs} = \frac{3}{2}\, \lambda_{ribs}\, i_q = 2\, B_{ribs} S_{ribs}\, L\, r\, A_d \tag{2.11}$$

According to the vector diagram the IPF is evaluated with (2.12), the flux angle δ is calculated
with (2.13).
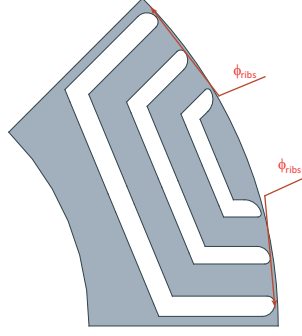
FIGURE 2.5: ribs flux over rotor section, simplified model

$$IPF = sin(\gamma - \delta) \tag{2.12}$$

$$\delta = atan\left(\frac{L_{q,pu}}{L_{d,pu}}\frac{A_q}{A_d} + \frac{\lambda_{ribs}}{\lambda_{md}\left(1 + \frac{L_{\sigma,pu}}{L_{md,pu}} + \frac{L_{zz,pu}}{L_{md,pu}}\right)}\right) \tag{2.13}$$

In a correct design it is necessary to minimize the width of the iron ribs, according to the centrifugal stress limit and design an air quantity in the machine that takes into account the d-axis saturation. According to the rotor cross section shown in Fig2.10a, the air length on the rotor is defined as in (2.14). The length of the iron flux guide on the rotor side is evaluated by (2.15).

$$l_a = \sum_{k=1}^{n_{lay}} l_k \tag{2.14}$$

$$l_{fe} = r - r_{shaft} - l_a \tag{2.15}$$

In order to correctly design the d-axis is necessary to place on the rotor the same iron presents on the stator. Considering that usually the flux guides not work at the same flux density, is necessary to design l_{fe} 20-25% bigger than l_y. In Fig.2.6 are shown two solutions: the first in Fig.2.8a, that satisfies the condition $l_{fe} = l_y$ and the second in Fig.2.6b that do not satisfy the previous condition. The $K_{fe,rot}$ shown in Fig.2.8 is defined in (2.16).

$$K_{fe,rot} = \frac{l_{fe}}{l_y} \tag{2.16}$$

where l_y is the stator yoke length, see Fig.2.10a.

It is possible to see that the wrong design of the iron quantity leads to higher saturation of the rotor flux guides, see Fig.2.7 that decrease the d-axis flux linkage Fig.2.8a. The reduction of the d-axis component reduce the torque production, see Fig.2.8. The design of the rotor iron quantity is in conclusion related to the iron yoke on the stator.

2.2.3 PM's fix the reluctance part

The design of the PMs contribution is a trade off between costs and performances. In the following it will be considered the case of the characteristic current condition, where the characteristic current is equal to the rated current. This solution is illustrated in Fig.2.9. The q axis flux linkage component is compensated by the PM-contribution. The formula that summarize this point is (2.17), where i_{ch} is the characteristic current assumed equal to the rated or nominal current. Formula (2.17) permits to maximize the Constant Power Speed Range for the characteristic current, obtaining flat power vs speed behavior in the flux weakening region. The design of the PM quantity is possible according to a linearized model, [10], disregarding cross saturation, as will be illustrated in chapter 2.2.1 or by FEA in chapter 3.3. The addition of permanent magnets work in the direction of increase the power factor, with benefits in the reduction of the converter size. The relation between PMs quantity and characteristic current is shown in Fig.2.9b, with formula (2.17). This solution permits to obtain the maximum CPSR at the rated current.
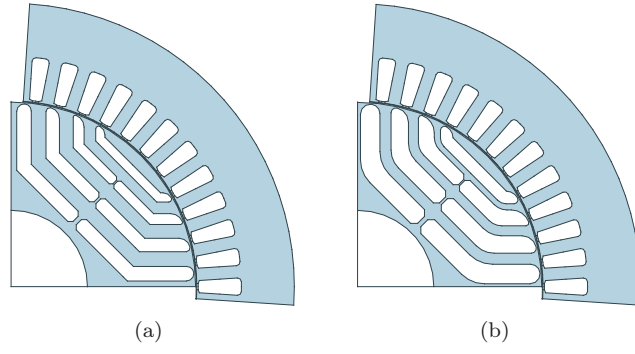
FIGURE 2.6: (a) motor designed with $K_{fe,rot} = 1,2$; (b) motor designed with $K_{fe,rot} = 0,7$
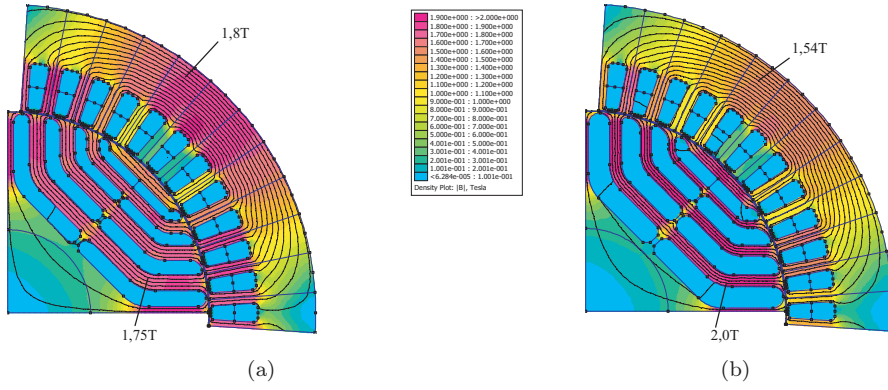
FIGURE 2.7: Flux density Map for: (a) $K_{fe,rot} = 1,2$; (b) $K_{fe,rot} = 0,7$
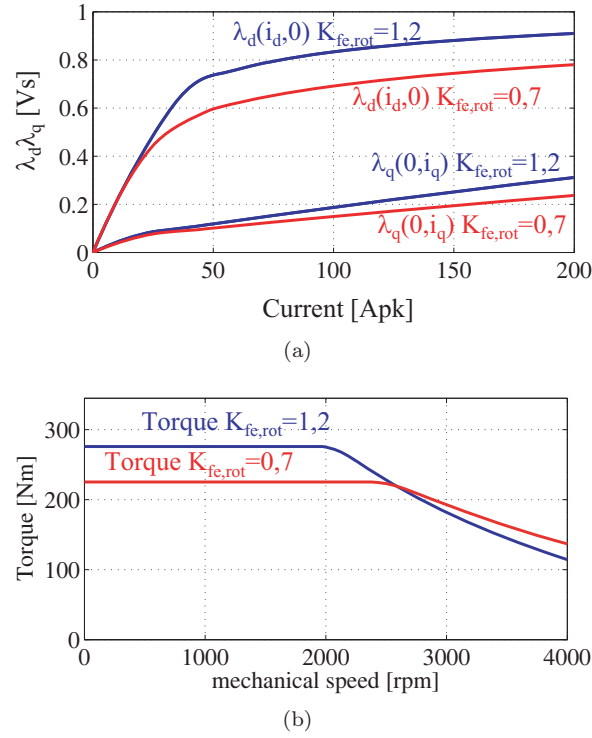
FIGURE 2.8: (a)$\lambda_{d,q}(i_d, i_q)$ SyR with $K_{fe,rot} = 1,2$ blue curve and $K_{fe,rot} = 0,7$ red curve ; (b) torque vs speed $K_{fe,rot} = 1,2$ blue curve and $K_{fe,rot} = 0,7$ red curve

$$\lambda_{PM} = L_q\, i_{ch} \tag{2.17}$$
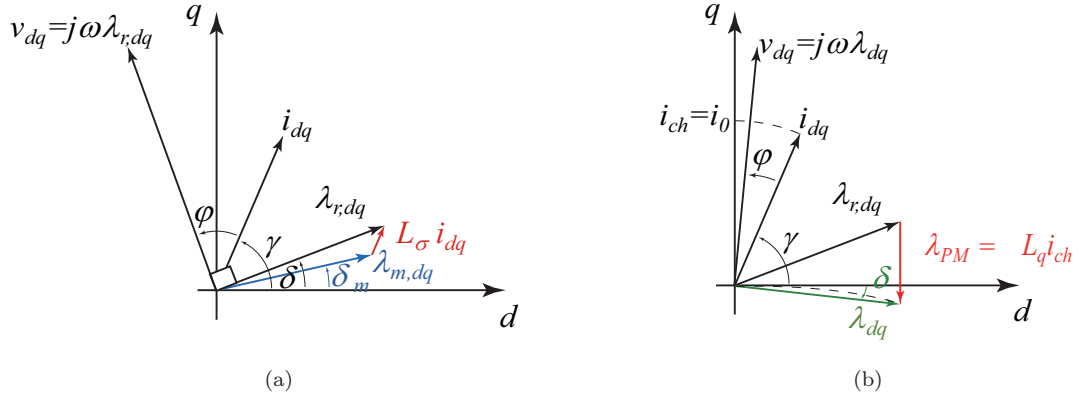
FIGURE 2.9: (a) vector diagram SyR configuration; (b) vector diagram PM-SyR

The permanent magnet torque component (2.18), like in the previous paragraph T_{PM} can be expressed in function of the airgap flux density related to PMs and d-axis current loading, equation (2.20) can be obtained substituting the definition of λ_{PM} (2.19) in (2.20).

$$T_{PM} = \frac{3}{2}\, p\, \lambda_{PM}\, i_d \tag{2.18}$$

$$\lambda_{PM} = 2p\, \lambda_{1,pole} \quad \Rightarrow \quad \lambda_{PM} = 2\frac{\pi r}{p}\, L\, N_s\, k_w\, B_{g,PM} \tag{2.19}$$

$$T_{PM} = \pi\, r^2\, L\, B_{g,PM}\, A_d \tag{2.20}$$

$$TRV_{PM} = B_{g,PM}\, A_d \tag{2.21}$$

The airgap flux density can be evaluated with a linear permenace network on the q-axis. In Fig.2.10 is shown the permeance network and the geometric data used for obtaining the various permeance components shown in Fig.2.10b.
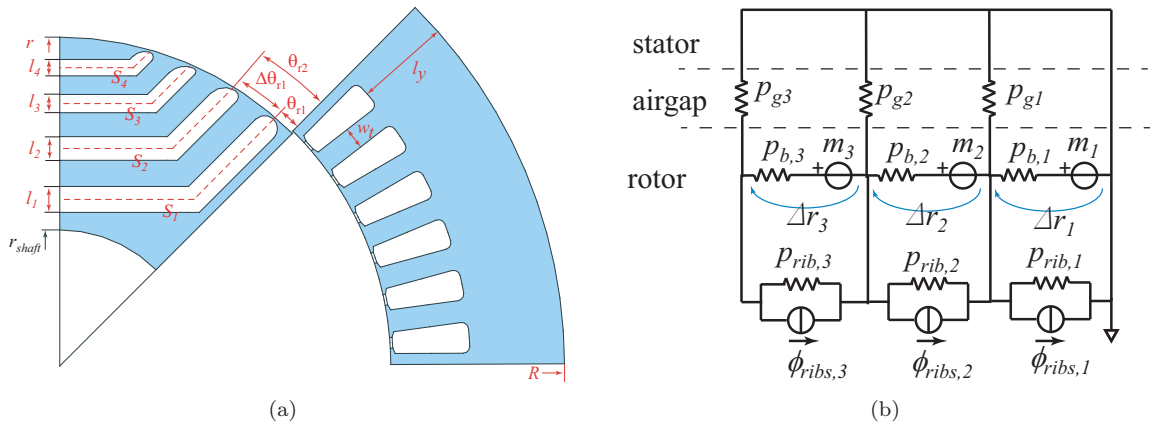
FIGURE 2.10: (a) cross section with main geometric indications ; (b) q-axis permeance network with magnet

The airgap permeances are evaluated by (2.22). With (2.23) is calculated the barrier permeance. For simplify the analysis, barriers are considered completely filled with magnet.

$$P_{g,k} = \frac{\mu_0 \, r \, \theta_{r,k}}{g} \qquad k = 1 : n_{lay} \tag{2.22}$$

$$P_{b,k} = \frac{\mu_0 \, S_k \, L}{l_k} \qquad k = 1 : n_{lay} \tag{2.23}$$

For taking into account the iron ribs, (2.22) and (2.23) become (2.24) and (2.25), that are used in the linear system (2.26). The solution of (2.26) permits to evaluate the rotor magnetic potential and consequently the airgap flux density.

$$P_{beq,k} = \frac{\mu_0 \, L}{l_k} \left(\mu_{ribs} \frac{S_{ribs}}{S_k} \frac{l_k}{l_{ribs}} + 1 \right) \qquad k = 1 : n_{lay} \tag{2.24}$$

$$m_{eq,k} = \frac{B_r \, l_k}{\mu_0} \left(\frac{S_k - \frac{B_{ribs}}{B_r} S_{ribs}}{S_k + \mu_{ribs} \frac{S_{ribs}}{l_{ribs}} l_k} \right) \qquad k = 1 : n_{lay} \tag{2.25}$$

$$\begin{bmatrix} P_{beq,1} + P_{beq,2} + P_{g,1} & -P_{b,2} & 0 \\ -P_{beq,2} & P_{g,2} + P_{beq,2} + P_{beq,3} & -P_{beq,3} \\ 0 & -P_{beq,3} & P_{beq,3} + P_{g,3} \end{bmatrix} \begin{bmatrix} r_1 \\ r_2 \\ r_3 \end{bmatrix} \begin{bmatrix} P_{beq,1} & 0 & 0 \\ -P_{beq,1} & P_{beq,2} & 0 \\ 0 & -P_{beq,2} & P_{beq,3} \end{bmatrix} \begin{bmatrix} m_{eq,1} \\ m_{eq,2} \\ m_{eq,3} \end{bmatrix} \tag{2.26}$$

Finally the airgap flux density is evaluated with (2.27). The result shown in Fig.2.11 does not take into account the slots opening, for correcting (2.27) it is used an equivalent airgap length, bigger than the geometric length (Carter factor K_c).

$$B_{g,PM,k} = \frac{\mu_0}{g_{kc}} \, r_k \qquad g_{kc} = K_c \, g \tag{2.27}$$
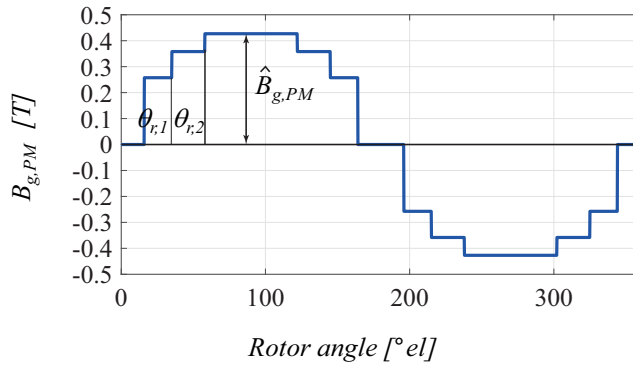
FIGURE 2.11: $B_{g,PM}$ function of rotor position

In order to satisfy (2.17) it is necessary to evaluate the q-axis inductance, as shown in (2.28). The q-axis inductance is the sum of three components, the slot leakage inductance, the circulating component L_{cq} and flow through L_{fq} inductance. The slot leakage inductance can be evaluated with formulation illustrated in [11], L_{cq} and L_{fq} here summarized in (2.29) and (2.30) are detailed in [4].

$$L_q = L_\sigma + L_{cq} + L_{fq} \tag{2.28}$$

$$L_{cq} = \frac{6}{\pi^2} \frac{a}{g} \mu_0 \, L \, \frac{(k_w \, N_s)^2}{p} \left[1 - \frac{4}{\pi} \sum_{k=1}^{n_{lay}} f_k^2 \Delta\theta_r \right] \tag{2.29}$$

$$L_{fq} = \frac{6}{\pi^2} \frac{a}{g} \mu_0 \, L \, \frac{(k_w \, N_s)^2}{p} \left[\frac{4}{\pi} \sum_{k=1}^{n_{lay}} p_{bk} \, (\Delta f_k)^2 \Delta\theta_r \right] \tag{2.30}$$

2.3 Summary of the SyR design procedure

The design of a SyR machines, see Fig.2.12, starts with the definition of the external frame and the allowable Joule loss per outer surface, function of the maximum winding temperature. The next step is the definition of the stator/rotor split and core/copper split in order to obtain a reasonable trade-off between torque production and power factor. The air quantity in rotor is chosen to obtain a $K_{fe,rot} = 1.2 \div 1.25$ that permits a similar iron saturation on the rotor side and on the stator yoke. At this step if the target torque and power factor are satisfied the design of the SyR machine is finished. PM-SyR motor starts at the end of the design of the best SyR machines. The addition of the permanent magnets is related to the definition of the characteristic current. In general I_{ch} is assumed equal to the rated current, than it is necessary to satisfy (2.17). The B'_r is the fictitius PM remanence, used in the case of flux barriers fulfilled with magnets. The B'_r value represents a minimum value of PM remanence that is necessary in order to satisfy (2.17). If B'_r is too small respect to commercial magnets it is possible to use higher remanence magnets reducing the magnet volume, this point will be clarified in the next.
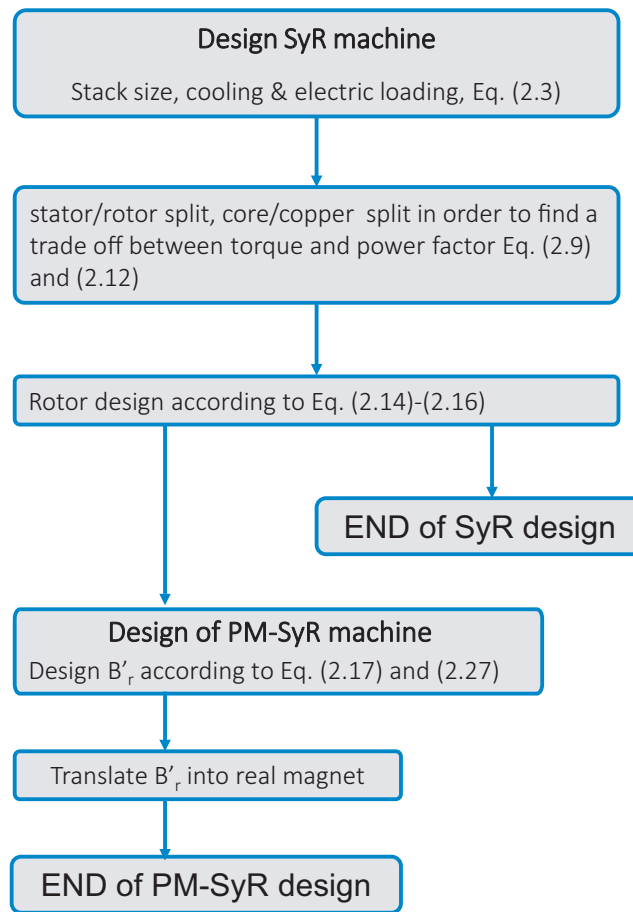
FIGURE 2.12: SyR machine design procedure

Chapter 3

Replacement of IE3 Induction Motor for Variable Speed Applications

3.1 Motors under comparison

In the following it will be shown the design of three machines that reach the IE4 and IE5 efficiency class. The final results are shown for all the cases, the adopted design procedure, instead is detailed, only for H160. In order to initially simplify the comparison, the design starts from a commercial induction motors for general purpose applications. The machines are four poles with a base speed of 1500rpm (50Hz). The stator and iron are the same of the Induction Motors (IM). The airgap length is also the same, this mean that the rotor airgap radius does not change. The results reported in Tab.3.1, and in Fig.3.1 show that the induction motor presents an efficiency around the IE3 class. Changing only the rotor construction, with SyR-A is possible to touch on the IE4 class. Passing to PM-SyR-A it is possible to overstep IE4 and go near to the IE5 class. This first result shows that SyR machines permit to increase the efficiency, but for go over the IE4 is necessary to add magnets or re-design the machines in the direction of maximum efficiency (SyR-D and PM-SyR-D). Properly design the machines for maximizing the efficiency, see Fig.3.1b, it is possible to overcame the IE4 with SyR technology (+1.06% respect to IM). The addiction of magnets lead to go over the IE5 class. It is important to underline that also the solutions SyR-D and PM-SyR-D presents the same stack length and stator radius of the original IM.

TABLE 3.1: Power and efficiency results of induction motor vs SyR and PM-SyR

H	pole pair	speed [rpm]	$P_{shaft}[kW]$	η_{IM}	η_{SyR-A}	$\eta_{PM-SyR-A}$	η_{SyR-D}	$\eta_{PM-SyR-D}$
H132	2	1500	18.5 (IE4 94.3%, IE5 95.2%)	92.7	93.53	94.32	95.07	95.87
H160	2	1500	40.7 (IE4 95.3%, IE5 96.1%)	94.6	95.21	95.78	95.61	96.54
H180	2	1500	75 (IE4 96%, IE5 96.6%)	94.6	95.8	96.5	96.16	96.94
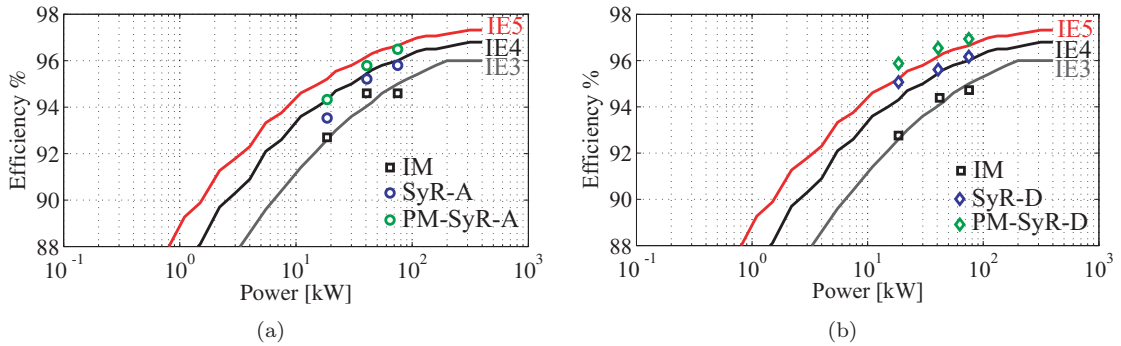
FIGURE 3.1: (a) Efficiency comparison between IM and SyR-A (equal stator to IM) ; (b) Efficiency comparison between SyR-A (equal stator to IM) and SyR-D (Design for efficiency maximization)

3.2   Design for efficiency improvement

Using the equations detailed in Chap 1.2.2 it is realized the $b-x$ plane shown in Fig.3.2. In this case the plane is referred to constant shaft power and not to constant K_j. The d-axis, current loading is evaluated in order to satisfy the magnetic loading $b\,B_{fe}$. The q-axis component of the current loading A_q is calculated in order to satisfy the request torque, directly calculated from the shaft power. The speed is constant and equal to the base speed (1500 rpm in this case). The efficiency locus on the $b-x$ plane and the iso power factor locus on the same plane are shown in Fig.3.1a,b. The initial (SyR-A) and final (SyR-D) design are shown in Fig.3.3. As expected the efficiency increase reducing the airgap radius. The reduction of the airgap radius increase the slot area and consequently reduce the Joule losses that are dominant respect to the iron losses. Iron losses are practically constant because the iron volume does not change significantly. The different designed stators are shown in Fig.3.4, the costs change, see Fig3.4b, because the increment of the Copper component leads cost from 199US\$ for SyR-A to 221US\$ for SyR-D with an increment of 10.5%.

FIGURE 3.2: (a) efficiency locus at constant P_{shaft}; (b) isopower factor locus at constant P_{shaft}

FIGURE 3.3: Cross section of stator and rotor, for the initial design SyR-A and the final design SyR-D

The reduction of power factor badly affects the size of the converter. On the other hand the relatively lower variation of the power factor and the commercial step size of the converters lead to the result that changing the motor cross section not necessarily means change the inverter size.

3.3   Permanent Magnet Assistance

The benefits of the insertion of permanent magnets are outlined previously and detailed in literature [12]. The main benefit of PMs are not only on torque production but also on Power profile. The output power is maintained the same of the SyR cases. This is because the machines are designed

FIGURE 3.4: (a) stator cross section for SyR-A and SyR-D; (b) cost comparison of
SyR-A and SyR-D

with reference to the nominal power.The main hypothesis, in the power evaluation is that the nominal power is also the base power. Stator resistance is avoided, than nominal power is evaluated by (3.1). This equation is referred to condition called *Natural Compensation* represented in Fig.3.5. The rated voltage can be approximately evaluated by $V_{rated} = \omega \lambda$, where for the flux calculation is used (2.5); than the current is expressed in function of the Current loading (3.2).

$$P_b = \frac{3}{2} V_{rated} I_{ch} \sin(\gamma) \tag{3.1}$$

$$P_b = \omega_{mech} L \pi r^2 b B_{fe} \sqrt{A_d^2 + A_q^2} \sin(\gamma) \tag{3.2}$$
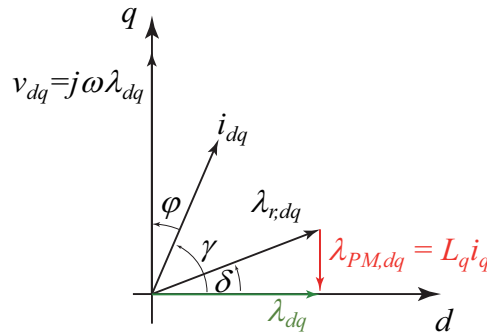
FIGURE 3.5: PM assistance, Natural Compensation

Where A_d represents the current loading along the d-axis, related to the magnetizing flux component. A_q in the torque component. Model and FE results are compared in Tab.3.2. It is possible to appreciate that for reaching the power performances, it is feasible the use of lower remanence PMs. B_r' value is referred to full-filling the barriers with magnets. Than reducing the magnet volume, it is possible to use magnets with commercial value of B_r. The difference between the model and FEA is also on the geometry. The model use simplified rotor geometry construction, with flux barrier with circular section, this leads to over estimate the magnet volume. Solutions using Ferrite and Neodymium magnets are shown in Fig.3.7. The value of B_r is referred to hot condition at 100°C. The magnets section illustrated in Fig.3.7 is in the ratio of the B_r values, the performances of the two machines are equivalent.

The power and Torque vs speed profiles shown in Fig3.8 put in evidence, that the addition of the permanent magnet quantity permits to improve the torque and power density of 20%. PM-SyR machine presents a Constant Power Speed Range behavior, that is a desirable working performance for variable speed drive applications. The nominal torque and power are generated, respectively for SyR-D with 158A and PM-SyR-D with 130A. PM-SyR solution absorbs 82% of the SyR current, with

a reduction of 33% of the Joule losses. The benefit on the efficiency are previously shown in Fig3.1, making feasible the IE5 class. Tab.3.3 exhibits the mass quantity of iron, copper and magnet. Costs are summarized in Fig3.9 the introduction of permanent magnets increase costs as expected. On the other hand the use of Ferrite magnets permit to reduce the costs, obtaining the same performances that are feasible with stronger magnets. Considering for example PM - SyR-D the costs pass from 220US$ for SyR solution to 373US$ (+68%) for PM-Neo and 273US$(+23%) for PM-Ferrite. This evident variation leads to the fact that PM-SyR technology permits to improve the efficiency with a reasonable increment in costs. This can happen because the optimized reluctance performance leads to use weaker magnet like ferrite that are world wide diffuse. The market price of Ferrite is actually eighteen times lower than Neodymium.

FEA results shown in Tab.3.2 can be obtained with few simulations. The procedure is illustrated in Fig3.6, flux barriers are completely filled with fictitious magnet with remanence B'_r. The PMs flux linkage is evaluated varying B'_r, than with (3.3) is calculated the flux in the iron ribs and by (3.4) is calculated the B'_r necessary to compensate the q-axis flux at the characteristic current loading A_{ch}.

$$\lambda_{ribs} = \frac{\lambda_{m2}\, B'_{r1}}{B'_{r1} - B'_{r2}} - \frac{\lambda_{m1}\, B'_{r2}}{B'_{r1} - B'_{r2}} \tag{3.3}$$

$$B'_r = \frac{B'_{r1} - B'_{r2}}{\lambda_{m1} - \lambda_{m2}} \left(\lambda_{rq,A_{ch}} - \lambda_{ribs} \right) \tag{3.4}$$

TABLE 3.2: Comparison between model and FEA

	Model	FEA
$P_b[kW]$	40,7	40,7
$\gamma[el^\circ]$	78	65
$B_r[T]$	0,18	0,22
$V_{mag}[m^3]$	$9,01\,10^{-4}$	$6,37\,10^{-4}$
$\omega_{mech}[rpm]$	1500	1500
$A_{ch}[A/m]$	$3,657\,10^4$	$3,798\,10^4$
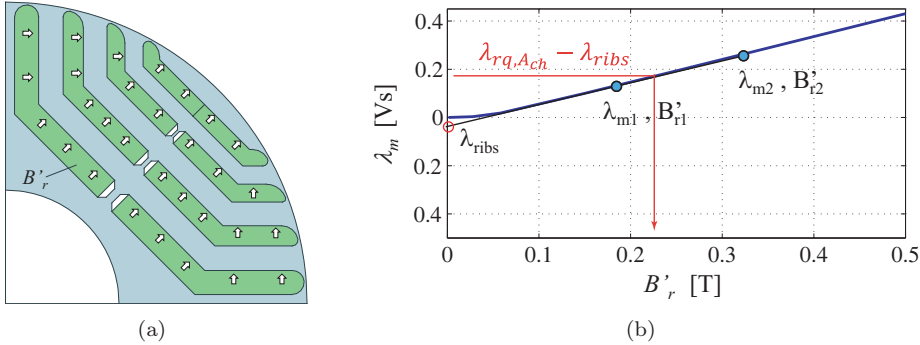
FIGURE 3.6: (a) rotor cross section with barriers completely filled with fictitious magnet B'_r; (b) PMs flux vs fictitious B'_r

TABLE 3.3: Mass value of the active material in machines under analysis for H160

	SYR-A	PM-SyR-Neo-A	PM-SyR-Ferrite-A	SYR-D	PM-SyR-Neo-D	PM-SyR-Ferrite-D
Copper Mass [kg]	17.02	17.02	17.02	23.24	23.24	23.24
Iron Mass [kg]	104.89	104.89	104.89	104.58	104.58	104.58
Magnet Mass [kg]	0	1.64	10.52	0	1.64	10.52
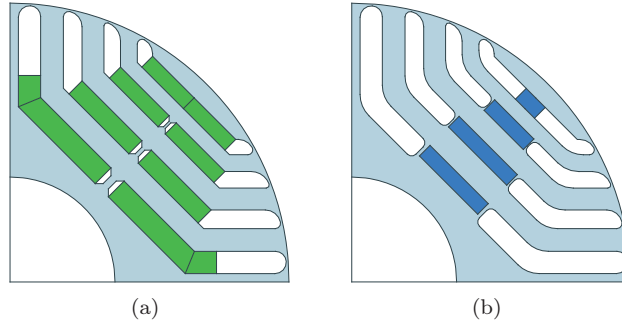
FIGURE 3.7: (a) Ferrite Magnet $B_r = 0,35T$; (b) Neo Magnet $B_r = 1,08T$
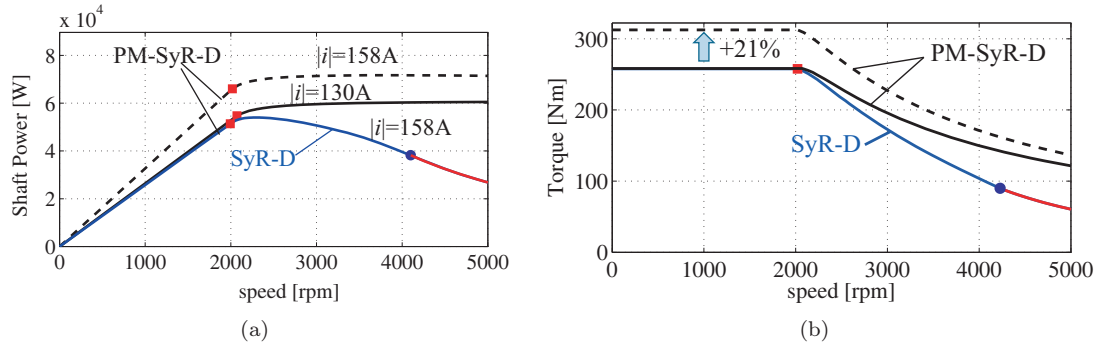
FIGURE 3.8: (a) Shaft power comparison between SyR-D and PM-SyR-D ; (b) Torque comparison between SyR-D and PM-SyR-D
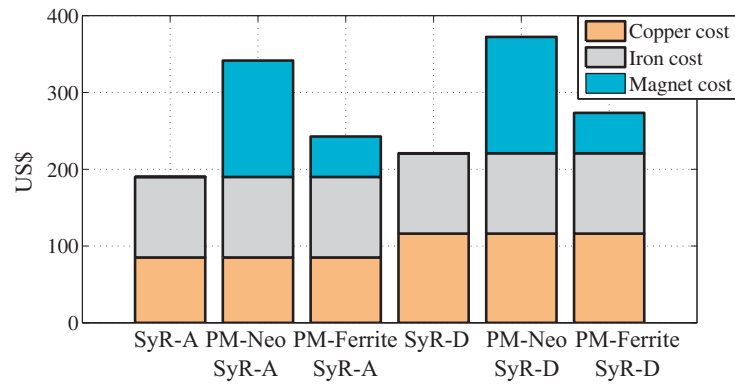
FIGURE 3.9: Cost comparison between the different machine SyR and PM-SyR solution

3.3.1   PM-SyR stack length variation (H160)

In this section it will be shown that, in the case of PM-SyR machine is possible to reduce the stack length in order to obtain the same losses per outer surface of the SyR machine. As said in the previous paragraph, working at equal K_j means at first, maintain copper temperature constant. The stack length reduction, reduce the active material in the machine with benefit on costs. Considering a design at constant output torque the efficiency is reduced. In the following it will be developed a design for H160, showing that the efficiency is still higher than the IE5 class. The reduction of the stack length for PM-SyR-D for reach the same specific losses of SyR-A is shown Fig.3.10. Length move from 270mm to 220mm (81.4%), the efficiency move from 96.93% to 96.34% still higher than the IE5 limit. In terms of costs, see Fig.3.11. Solution PM-Fe-SyR-A-L235 presents the same cost of SyR-D. Respect to Fe-SyR-A-L270 the total active cost change from 247US$ to 216US$ (87%). Respect to the SyR price the increment in price is around 8%, the benefits are the CPSR not present in the SyR machine and the feasibility of IE5 efficiency class. The stack increment not necessarily leads to an increment in efficiency. This is related to the fact that increasing the stack length, iron losses increase too. Joule losses instead are reduced with the increment of the stack length (output torque constant). Consequently efficiency trend is related to the different weight of copper and iron losses on the total ones, see Figs.3.10b,c.
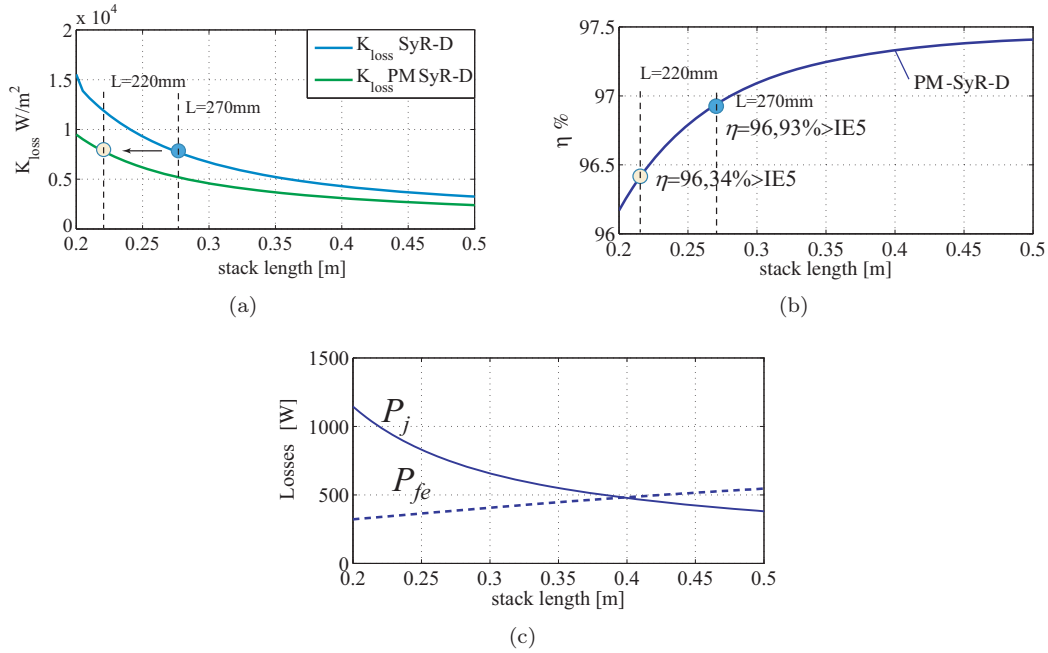
FIGURE 3.10: a) K_j @ T=const=260Nm ; b) η @ T=const=260Nm; c) Losses contributions varying the stack length
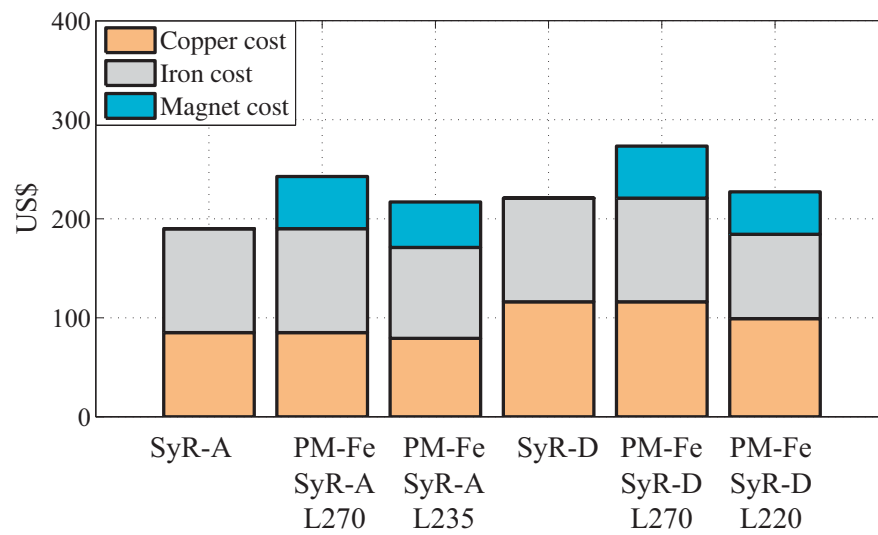
FIGURE 3.11: Costs comparison between SyR and PM-SyR solution at different stack length

Chapter 4

IE4+ Efficient Machines for Constant Speed Applications

4.1 The Rediscovery of Line Start Synchronous Reluctance Machines

Line-start synchronous motors are adopted in alternative to line-supplied Induction Motors (IM) due to their better efficiency [13]-[14]. All the cited examples refer to permanent magnet (PM) line start motors, and this has been true since the introduction of rare-earth PMs back in the 1970s. The volatility of rare earth materials price over the last ten years has led to reconsider the Synchronous Reluctance (SyR) machine as a viable alternative to induction motors for constant speed applications. Line-Start SyR (LSSyR) machines were studied and adopted in the '60s and the '70s [15]-[16].
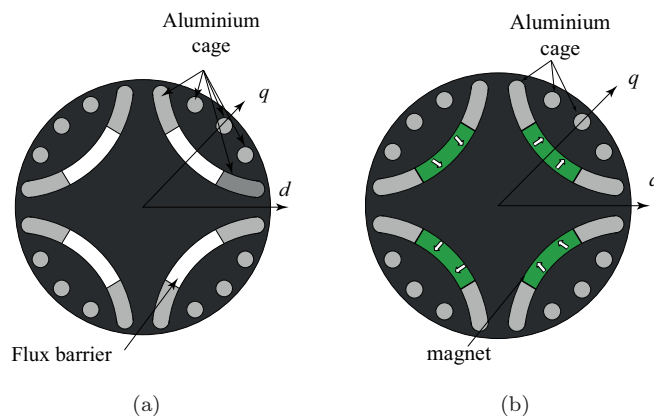
FIGURE 4.1: LSSyR rotor with circular cage bars

LSSyR machines are specifically advocated for their synchronous performance in application were is necessary to reach constant known speed, that is not possible for the induction motor due to the slip that change with load, [17]. Lately, the diffusion of vector controlled IM drives with a precise speed control and PM based line start machines with a higher torque density, led to leave LSSyR technology. In retrospect, being the literature about LSSyR rather aged, all the improvements of SyR motor design emerged between now and the '70s have never been tested in line-start applications. The research upon SyR motors for vector-controlled drives has produced up to date multi-barrier rotors [4], having better saliences than the ones adopted for LSSyR in the literature, and disclosing a potential for a higher torque and a better power factor at synchronous speed. A typical LS-SyR rotor configuration is shown in Fig 4.1, usually this machines were derived from an induction motors for the cage configuration, and cuts are add on the rotor structure in order to insert magnet for obtaining reluctance properties.

In [18] is proposed the design of a LSSyR motor for pumps application, based on a SyR rotor with four flux barriers filled with aluminum completely and short-circuited at both ends of the stack to made the rotor cage, see Fig4.2. The design of the rotor laminations is based on the state of the art of SyR machines. The design guidelines for obtaining the best compromise between the pull-in and pull-out torque values are given. The pull-in torque represents the synchronization capability intended
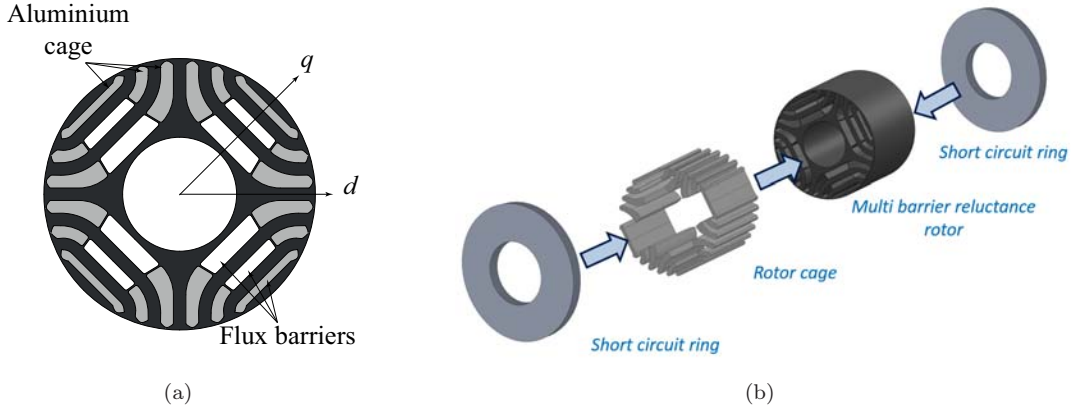
FIGURE 4.2: a) LSSyR rotor with cage like in IM b) PM Line Start motor 3D view
of the various rotor components

as the maximum load that can be put into step. The pull-out torque represents the performance
at synchronous speed, meaning the maximum load applicable at synchronism. A lumped parameters
model of the motor is presented, and simulated in the time domain to investigate the pull-in transients.
From the same model the steady state torque is expressed analytically, as a function of the slip speed
between the voltage vector, defining the synchronous speed, and the rotor. The lumped parameters
approach gives precious hints but it is not very accurate in terms of evaluating the pull-in torque
and the inertia that can be actually put into step. Works [19],[20], show the estimation of the cage
parameters in the direction of quantitatively refine the lumped parameters model. Finite Element
Analysis (FEA) simulations of the transient with motion type are used in order to accurately evaluate
the transient behavior. Also using transient with motion FE simulations some discrepancy remain
respect to the experimental results, this is related to the behavior of the rotor short circuit rings, see
Fig.4.2b. In the following an introduction in the model of LSSYR motors will be show, illustrating
some of the key points in the design that could be obtained with the model. Than two machines are
FEA validated and prototyped. A test campaign is conducted in order to experimentally measure the
synchronizing capability of this machines.

4.2   Modelling of LSSyR motor

The dynamic model of the LSSyR machine accounts for the concurrent presence of rotor saliency, as
in a SyR machine, and a short circuited rotor cage, as in an Induction Motor [13]. The dq reference
frame, synchronous to the rotor, is defined in Fig. 4.3. The rotor speed, in electrical radians, is ω_r.
The voltage vector, also in Fig. 4.4, is imposed by the AC mains that define the angular frequency ω,
p is the number of pole pairs. In the rotor frame, the voltage slips at $\omega - \omega_r$ and the slip s is defined
according to:

$$s = \frac{\omega - \omega_r}{\omega} \tag{4.1}$$

4.2.1   Dinamic Model

$$v_s = R_s\, i_s + \frac{d\lambda_s}{dt} + j\omega\lambda_s \tag{4.2}$$

$$0 = \begin{bmatrix} R_{rd} & 0 \\ 0 & R_{rq} \end{bmatrix} i_s + \frac{d\lambda_r}{dt} \tag{4.3}$$

The subscript s stands for "stator" variables, whilst the subscript r stands for "rotor". The non
isotropic shape of the cage bars is reflected into the rotor parameters of the model, and then the rotor
resistances are different for the d and q axes in (4.3). The magnetic model is:

$$\bar{\lambda}_s = L_{\sigma s}\, \bar{i}_s + \begin{bmatrix} L_{md} & 0 \\ 0 & L_{mq} \end{bmatrix} \bar{i}_m \tag{4.4}$$

FIGURE 4.3: Definition of the stator and rotor synchronous reference frames. Definition of the synchronous speed

(a)

(b)
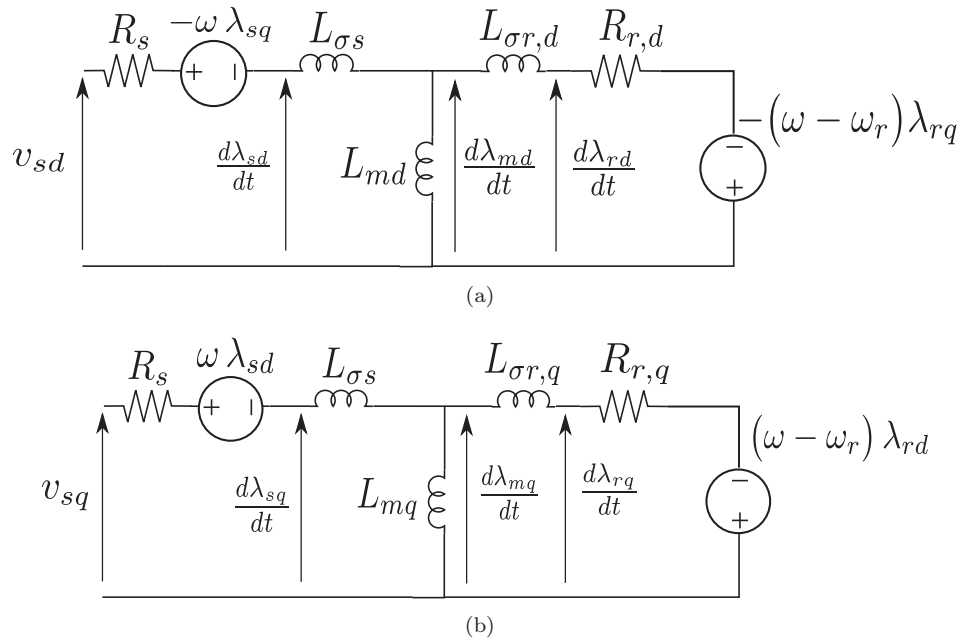
FIGURE 4.4: Dynamic equivalent circuit of LSSyR machine, in dq components

$$\bar{\lambda}_r = \begin{bmatrix} L_{\sigma r,d} & 0 \\ 0 & L_{\sigma r,q} \end{bmatrix} \bar{i}_r + \begin{bmatrix} L_{md} & 0 \\ 0 & L_{mq} \end{bmatrix} \bar{i}_m \tag{4.5}$$
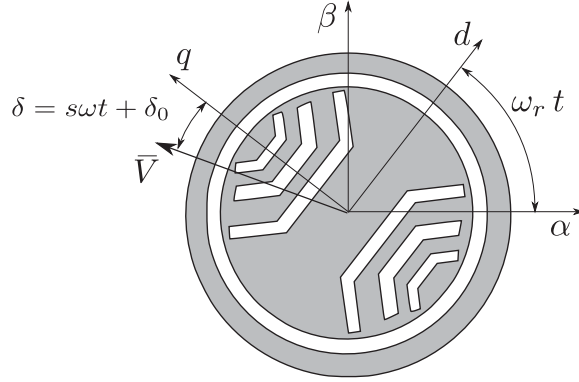
$$\bar{i}_m = \bar{i}_s + \bar{i}_r \tag{4.6}$$

Where L_{md} and L_{mq} are the magnetizing inductances. $L_{\sigma s}$ and $L_{\sigma r,d}$ are the stator and rotor leakage inductances, respectively. As for the rotor resistances, also the rotor leakage inductances are not equal in d and q in (4.5). Basically, all the parameters of the circuit related to the rotor reflect the rotor anisotropy. The electromagnetic torque and the mechanical equations are:

$$T_{em} = \frac{3}{2} p \left(\bar{\lambda}_s \wedge \bar{i}_s \right) \tag{4.7}$$

$$J_{tot} \frac{d\omega_r}{dt} = T_{em} - T_{load} \tag{4.8}$$

Where J_{tot} accounts for the motor and load inertia and T_{load} is the load torque.

(a)   (b)
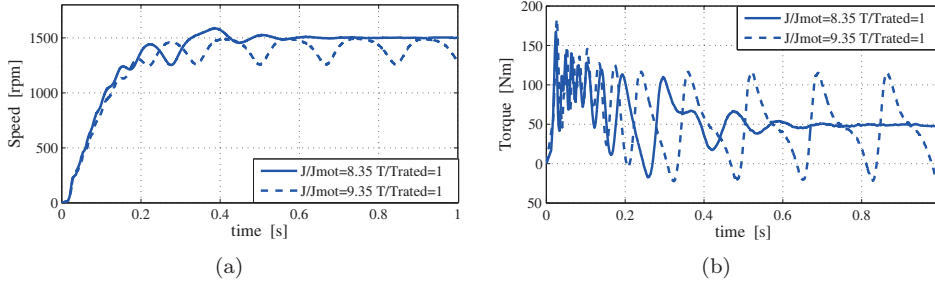
FIGURE 4.5: Torque and speed transients

4.2.2   Quasi steady state torque as function of the slip speed

The first assumption is that the electric and magnetic phenomena are faster than the mechanical transients, so the slip speed can be assumed constant time by time, while the voltage vector steadily rotates around the rotor at slip speed. The steady state electrical condition corresponds to replace the time derivatives d/dt in (4.2)-(4.3) with the operator $j(s\omega)$, valid for steady state sinusoidal variables, as they were all phasors. The angular frequency of the phasors is $s\omega$ because of the chosen rotor frame. The electrical equations (4.2)-(4.3) become (4.9) and (4.10) respectively:

$$\begin{cases} V_{sd} = R_s\,I_d + j\,s\omega\Lambda_{sd} - \omega_r\Lambda_s q \\ V_{sq} = R_s\,I_q + j\,s\omega\Lambda_{sq} - \omega_r\Lambda_s d \end{cases} \tag{4.9}$$

$$\begin{cases} 0 = R_{rd}\,I_{rd} + js\omega\Lambda_{rd} \\ 0 = R_{rq}\,I_{rq} + js\omega\Lambda_{rq} \end{cases} \tag{4.10}$$

Where capital letters indicate phasors. The torque expression (4.7) requires the stator current and flux linkage components to be expressed as $d-q$ phasors and then the vector cross-product to be calculated. To eliminate the rotor current from equations, this can be expressed as a function of the stator current by manipulation of (4.9) with (4.5) and (4.6).

$$\begin{cases} \bar{I}_{rd} = -\frac{js\omega\,L_{md}}{R_{rd}+js\omega\,L_{rd}}\,\bar{I}_{sd} \\ \bar{I}_{rd} = -\frac{js\omega\,L_{mq}}{R_{rq}+js\omega\,L_{rq}}\,\bar{I}_{sq} \end{cases} \tag{4.11}$$

$$\begin{cases} \bar{\Lambda}_{sd} = \left(L_{sd} - \frac{js\omega\,L_{md}}{R_{rd}+js\omega\,L_{rd}} \right)\bar{I}_{sd} = \bar{Z}_{pd}\,\bar{I}_{sd} \\ \bar{\Lambda}_{sd} = \left(L_{sq} - \frac{js\omega\,L_{mq}}{R_{rq}+js\omega\,L_{rq}} \right)\bar{I}_{sq} = \bar{Z}_{pq}\,\bar{I}_{sq} \end{cases} \tag{4.12}$$

$$\begin{bmatrix} \bar{V}_{sd} \\ \bar{V}_{sq} \end{bmatrix} = \begin{bmatrix} R_s + js\omega\,\bar{Z}_{pd} & -(1-s)\omega\bar{Z}_{pq} \\ (1-s)\omega\bar{Z}_{pd} & R_s + js\omega\,\bar{Z}_{pq} \end{bmatrix} \begin{bmatrix} \bar{I}_{sd} \\ \bar{I}_{sq} \end{bmatrix} \tag{4.13}$$

$$\begin{cases} V_{sd} = -\hat{V}\,sin(s\omega t + \delta_0) = j\hat{V} \\ V_{sq} = \hat{V}\,cos(s\omega t + delta_0) = \hat{V} \end{cases} \tag{4.14}$$

$$\begin{bmatrix} \bar{I}_{sd} \\ \bar{I}_{sq} \end{bmatrix} = \frac{1}{D_c} \begin{bmatrix} R_s + js\omega\,\bar{Z}_{pq} & (1-s)\omega\bar{Z}_{pq} \\ -(1-s)\omega\bar{Z}_{pd} & R_s + js\omega\,\bar{Z}_{pd} \end{bmatrix} \begin{bmatrix} j\hat{V} \\ \hat{V} \end{bmatrix} \tag{4.15}$$

$$D_c = R_s^2 + js\omega\,R_s\left(Z_{pd} + Z_{pq}\right) + (1-2s)\omega^2\,Z_{pd}\,Z_{pq} \tag{4.16}$$

$$\begin{cases} I_{sd} = a + jb \\ I_{sq} = c + jd \\ \Lambda_{sd} = e + jf \\ \Lambda_{sq} = g + jh \end{cases} \tag{4.17}$$

$$T_e = T_{cage} + T_{rel}\,cos\left(2\,s\,\omega\,t - \alpha\right) \tag{4.18}$$

$$T_{cage} = \frac{3}{4}\,p\,Real\left[\Lambda_{sd}^*I_q - \Lambda_{sq}^*I_d\right] \tag{4.19}$$

$$\begin{aligned} T_{rel} &= \tfrac{3}{2}\,p\,\sqrt{(ce+bh-df-ga)^2+(ed+cf-gb-ah)^2} \\ \alpha &= arctan\left(\tfrac{gb+ah-ed-cf}{ce+bh-df-ga}\right) \end{aligned} \tag{4.20}$$

The complete formulation is not easy to manipulate, and to understand, some simplification could be obtained avoiding the stator resistance.

$$\begin{aligned} \Lambda_{sd} &= \tfrac{V}{\omega} \\ \Lambda_{sq} &= -j\,\tfrac{V}{\omega} \end{aligned} \tag{4.21}$$

$$\begin{aligned} I_{sd} &= \tfrac{V}{\omega\,Z_{pd}} \\ I_{sq} &= -j\,\tfrac{V}{\omega\,Z_{pq}} \end{aligned} \tag{4.22}$$

Using (4.17) and cosidering the semplification of (4.21), (4.22), the cage torque (4.19) can be simplified to:

$$T_{cage} = \frac{3}{4}\,p\,(ce - bh) \tag{4.23}$$

Using (4.23) and the simplification (4.21), (4.22) the cage torque equation assume the expression:

$$T_{cage} = \frac{3}{4}\,p\left(\frac{V^2}{\omega}\right)\left(\frac{R_{rq}\,L_{mq}^2}{L_{sq}^2\,R_{rq}^2 + s^2\omega^2\left(L_{sq}L_{rq} - L_{mq}^2\right)^2} + \frac{R_{rd}\,L_{md}^2}{L_{sd}^2\,R_{rd}^2 + s^2\omega^2\left(L_{sd}L_{rd} - L_{md}^2\right)^2}\right) \tag{4.24}$$

Considering the situation near synchronism, with s that tend to zero it is possible to obtain the following equation:

$$T_{cage} = \frac{3}{4}\,p\left(\frac{V^2}{\omega}\right)\left(\frac{L_{mq}^2}{L_{sq}^2 R_{rq}} + \frac{L_{md}^2}{L_{sd}^2 R_{rd}}\right) \tag{4.25}$$

The impact of the cage resistances, $R_{rd,q}$, is weighted by the ratio L_{md}/L_{sd} and L_{mq}/L_{sq}, the red term is bigger than the q term, consequently is more important to reduce the d axis resistance. In order to understand the result shown in (4.25) some examples are studied. The motors under test are shown in Fig 4.6 the geometry is derived from an induction motor with 14 slots per pole pairs. The flux barriers are constructed starting from the rotor slots at the airgap. Solution named FUF n_r 14 presents the barrier completely filled with aluminum, PAF n_r 14 shows the inner flux barrier partially filled and in PAF n_r 14b is removed the slots along the q-axis. All the motors present the same reluctance behavior, iron ribs and flux barriers geometries are the same; this permits to understand

the behavior of the cage torque function of the different cage configuration. In Tab 4.1 are shown the rotor cage parameters evaluated for the three machines of Fig 4.6. Comparing FUF n_r 14 and PAF n_r 14 the increment of the cage resistances leads to increase the torque at zero speed and reduce the slope near the synchronism, see Fig 4.7. Removing the barrier along the q axis near the airgap, is possible to see that as mathematical formulated in (4.25) the equivalent resistance along the two axis presents different behavior and importance, R_{rd} presents an increment of 50% respect to PAF n_r 14, this leads to a downward shift, Fig 4.7, with loss of stand still torque and slope near the synchronism. A simple action like removing a cage bar leads to strong variation in the cage torque results. This mean that in order to maintain higher slope of the cage torque is necessary to maximize the aluminum quantity near the airgap, this leads also to increase the synchronizing capability that will be detailed in the next.
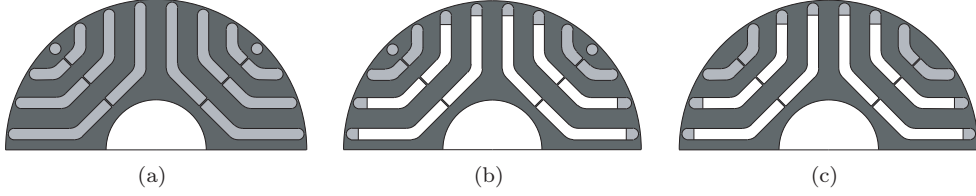
FIGURE 4.6: (a) FUF n_r 14 b) PAF n_r 14 c) PAF n_r 14b

	R_{rd}	R_{rq}
FUF n_r 14	0,25	0,5
PAF n_r 14	0,78	0,63
PAF n_r 14b	1,16	0,42

TABLE 4.1:   Rotor cage resistance value for cases in Fig.4.6
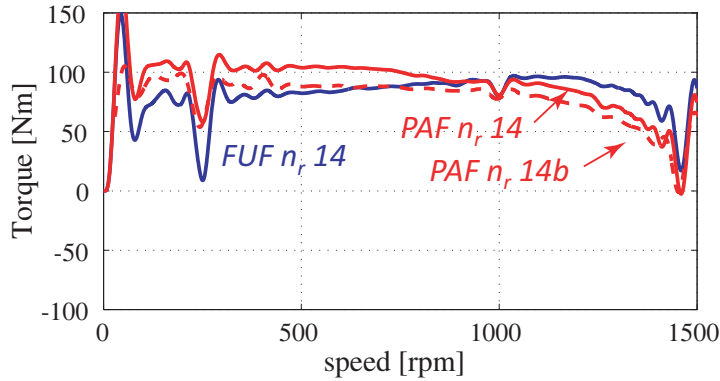
FIGURE 4.7: T_{cage} varying the R_{rd} value

4.2.3   Asynchronous Reluctance torque (No cage)

Reluctance machine presents non zero asynchronous torque, also without cage. It is possible to see that the presents of this torque is related to the non zero stator resistance that introduce a dis-symmetry in the voltage supplied configuration on the torque produced as motor and as generator. The rotor cage is avoided and consequently the rotor cage parameters (resistances and inductances) are eliminated in (4.12), the flux expression assume the simplified expression (4.26). Substituting (4.26) in (4.15), the current expression assume the formulation (4.27). Finally substituting (4.26) and (4.27) in (4.17), the final expression for the asynchronous reluctance torque, with no cage is obtained in (4.28).

$$\begin{cases} \bar{\Lambda}_{sd} = L_{sd}\,\bar{I}_{sd} \\ \bar{\Lambda}_{sd} = L_{sq}\,\bar{I}_{sq} \end{cases} \tag{4.26}$$

$$\begin{cases} \bar{I}_{sd} = \dfrac{(R_s + js\omega L_{sd})\,jV + (1-s)\omega L_{sd}\,V}{R_s^2 + js\omega R_s(L_{sd}+L_{sq}) + (1-2s)\omega^2 L_{sd}L_{sq}} \\ \bar{I}_{sd} = \dfrac{(R_s + js\omega L_{sq})\,jV + (1-s)\omega L_{sq}\,V}{R_s^2 + js\omega R_s(L_{sd}+L_{sq}) + (1-2s)\omega^2 L_{sd}L_{sq}} \end{cases} \tag{4.27}$$

$$T_{avg,rel} = \frac{3}{4}\,p\,V^2\,R_s\,\frac{(1-2s)\omega\,(L_{sd}-L_{sq})\,(L_{sq}-L_{sd})}{\left(R_s^2 + (1-2s)\omega^2\,L_{sd}L_{sq}\right)^2 + \left(s\omega R_s(L_{sd}+L_{sq})\right)^2} \tag{4.28}$$

The formulation (4.28) is not so simple. In order to understand possible trend under parametric investigation, a particular case is considered. S=1 (Stall Torque)

$$T_{avg,rel} = \frac{3}{4}\,p\,V^2\,R_s\,\frac{(1-\xi)^2}{\omega^3\,L_{sd}^2} \tag{4.29}$$

This formulation puts in evidence that the asynchronous reluctance torque (no cage) increases with the machine anisotropy. Figures 4.8 shows the asynchronous torque behavior, changing anisotropy. The anisotropy variation ca be obtained for example varying the number of flux barriers on the rotor. The effect of the asynchronous reluctance torque shown in Fig.4.8 is to modify the slope and the maximum value of the cage torque. Fig.4.8b shows the effect of the asynchronous reluctance torque with the overposition effect, it is necessary to underline that the use of the overposition principle is not applicable in this phenomena, because the effect of the cage change the electromagnetic behavior of the machine. On the other side in a qualitative way, the overposition principle permits to understand the asynchronous behavior and the reasons of the different asynchronous torque in a LS-SyR motors respect to the IMs.
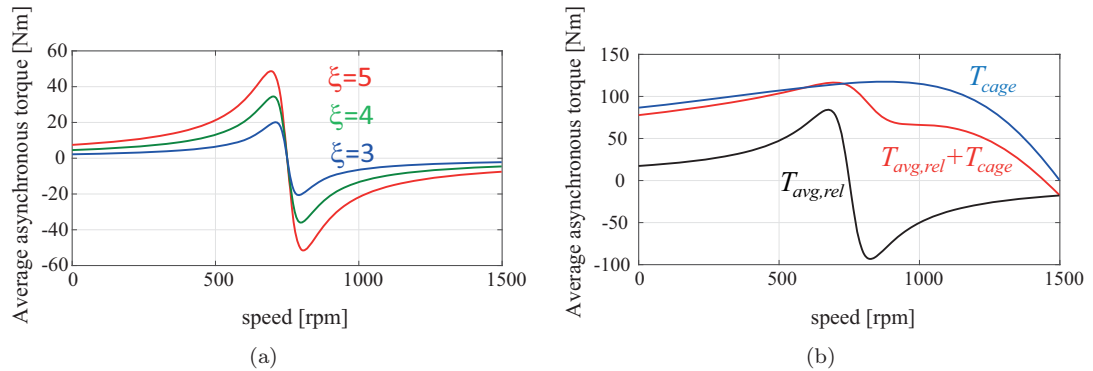
FIGURE 4.8: (a) Average asynchronous reluctance torque parametric investigation, (b) Overposition effect between cage torque and reluctance torque

	Param. Fig.4.9a	Param. Fig.4.9b
L_{md}	0,035	0,035
L_{mq}	0,0045	0,0054
L_{mq}	0,065	0,01
$R_{r,dq}$	0,8	[0,7 0,9]
$R_{r,dq}$	0,8	[0,9 1,1]

TABLE 4.2: Data used for the plot

4.3 Synchronization Process

The synchronization process represents the most important aspect in the design of this machines. The transient start-up of LSSyR motor can be synthesized in few steps, the cage torque pull-up the motor, from the standstill position towards synchronism. The reluctance torque is an alternating component, pulsating at twice the slip frequency during the starting phase of the motor. The steady-state envelope of $T_{cage} - T_{rel}$ to $T_{cage} + T_{rel}$ is represented in Fig 4.10a,b. Also the peak value T_{rel} is a function of
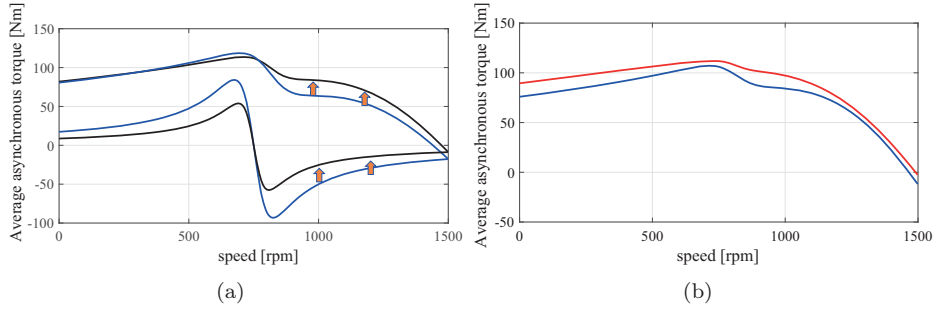
FIGURE 4.9: Impact of the reluctance asynchronous torque to the total asynchronous torque, according to data of Tab.4.2

the slip speed, as the height of the band around T_{cage} is not the same at all speeds. In particular, $T_{cage} + T_{rel}$ at synchronous speed coincides with the pull-out torque of the machine, see Fig 4.10: as usual for synchronous machines this is the maximum load torque that is applicable without loss of synchronism. The pull-out torque is normally much higher than the rated torque of the motor. However, having a high pull-out torque over rated torque ratio is an important figure of merit because it indicates that the motor has a high torque density and power factor at synchronous speed.
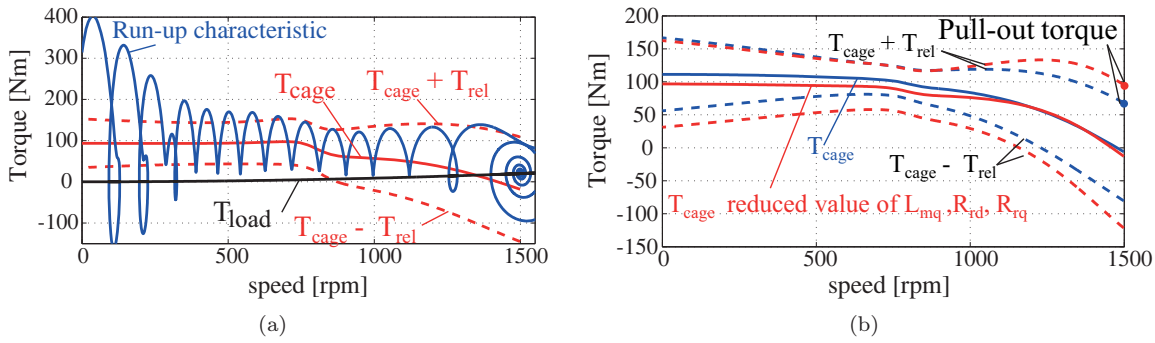
FIGURE 4.10: (a) Line start transient all torque component, (b) Cage torque and reluctance component

4.3.1 Pull-in Capability

The Pull-in Capability is the maximum load torque that the motor is able to put into synchronism at a given inertia. It represents a boundary region in the T_{load} vs $Inertia$ plane, a qualitative example for clarifying the explanation is shown in Fig 4.11a, all the combination $T_{load}, Inertia$ under the curve can be synchronized, instead the region over the curve represents the combination of $T_{load}\,vs\,Inertia$ that can not be synchronized. In the design process is really important to know the synchronizing capability, because it is necessary that all Load inertia in the lifetime of the machine are in the Synchronization Region. The behavior of the machine, if fails the synchronization is shown in Fig 4.11b, speed oscillates, torque presents an oscillation of two times the Pull-out torque, this induce current oscillation over the nominal value, and consequently high Joule losses. The torque oscillation induce shaft stress and noise.

4.3.2 Improvement of the Pull-in capability

In the previous paragraph are evidenced two main actors in the run-up process, the cage torque and the reluctance torque. In a very simple way is possible to think that for obtaining the best synchronization capability is necessary to run the rotor as much as possible near the synchronous speed (cage torque contribution) and than push it over the synchronism with the reluctance torque oscillation. From this consideration the design action to improve the synchronizing capability are:

(a)   (b)
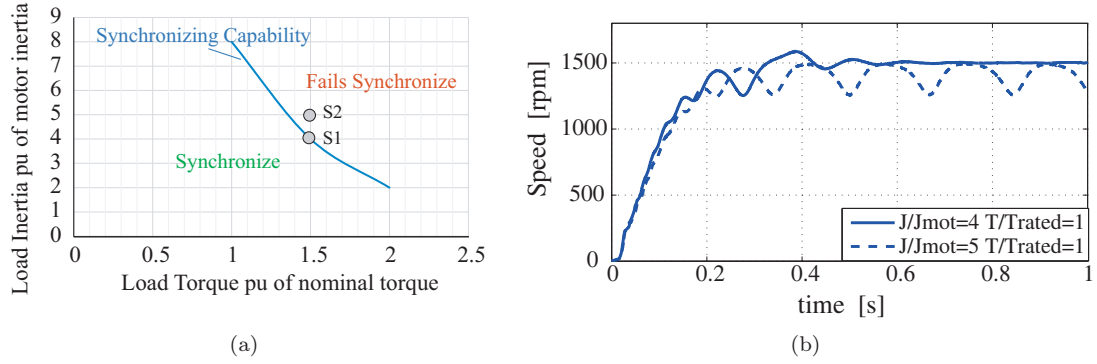
FIGURE 4.11: (a) Synchronizing Capability example (b) speed vs time of points S1
and S2

- design the rotor cage in order to improve the slope of the torque speed characteristic near synchronism;

- increase the anisotropic performance of the machine (pull out torque).

The pull-in capability of FUF n_r 14, PAF n_r 14 and PAF n_r 14b, whose cage torque are shown in Fig 4.7 is related to the slope of the cage torque. The effect of the R_{rd} variation, illustrated in Fig. 4.12, is shown by the curve PAF n_r 14 and PAF n_r 14b, full filling the barriers with aluminum the equivalent section of the rotor bars increase and consequently, due to the reduction of the rotor resistances, the slope increase and also the pull-in capability increase. A full analysis of this effect on a more realistic geometry was described in [18]. Results shown in Fig 4.12 are carried out with transient with motion FEA. Models are voltage supplied with $V = 300Vrms$ and a T_{load} proportional to the square of the speed (typical for funs or pumps) is applied to the shaft.
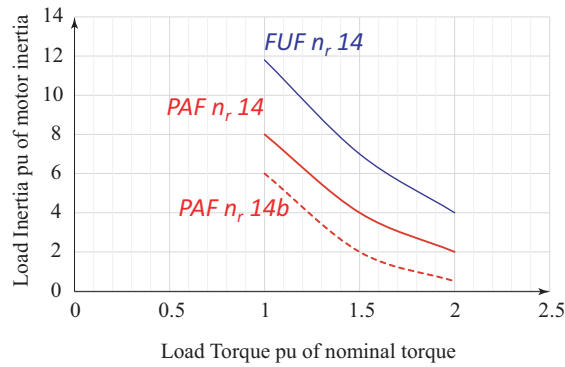
FIGURE 4.12: Synchronizing Capability of motors shown in Fig.4.6

The effect of removing a single bar on the q axis, leads to a great variation in the asynchronous performance of the machine, see Fig 4.7. This variation is reflected to the synchronizing capability. It is important to underline that all this considerations are carried out not changing the reluctance properties of the machines under test, see Fig 4.6. Higher investigation on a real SyR geometry leads to equivalent results, showing a region with different level of impact on the pull-in capability [18]. The region evidenced in Fig. 4.13 permits the reduction of the R_{rd} component with significant improvement of the slope of the cage torque near synchronism with benefits on the increment of the pull-in performance. This results is illustrated in Fig.4.14.

The action on the reluctance torque component is more complicated to describe, because it is composed by to separate effect: T_{rel} and $T_{avg,rel}$. This two torque components have two opposite effect on the pull-in capability. The T_{rel} increase the machine oscillations, giving more kinetic energy to the system to jump over the synchronous speed. The $T_{avg,rel}$ as shown in Section 1.2.3 acts towards the cage torque, reducing the slope near the synchronism and consequently it is necessary more energy to jump over the synchronous speed. The FEA results shown in Fig 4.15 give reason
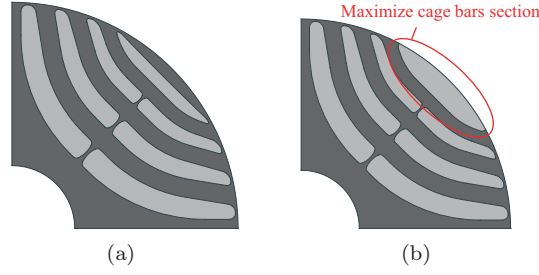
FIGURE 4.13: (a) LS2 four flux barrier rotor full filled with aluminum b) LS3 strong reduction of R_{rd}
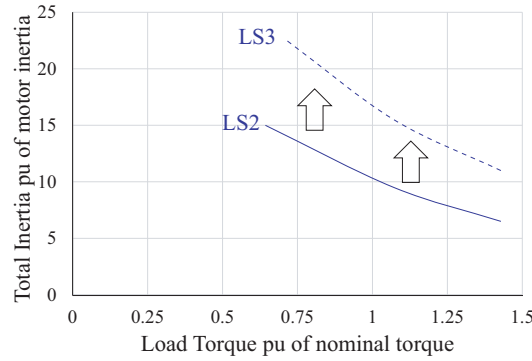
FIGURE 4.14: LS2 and LS3 synchronizing capability

to this consideration. The improvement of the anisotropy of the machine works in the direction of the increment of the pull-in capability. This happen if the reduction of the slope of the asynchronous torque is not too big to compensate and overcame the increment of the T_{rel} contribution. This effect is shown in Fig 4.15, improving the anisotropy is possible to see that finally the pull-in capability is reduced. It is important to underline that the results shown in Fig 4.15, are an investigation on the effect of the improvement of the anisotropy, in this first analysis is not considered the feasibility of the construction of the machine. Readers can understand that solution "PAF no ribs" can not work, but is shown for having a limit in the improvement of the anisotropy.
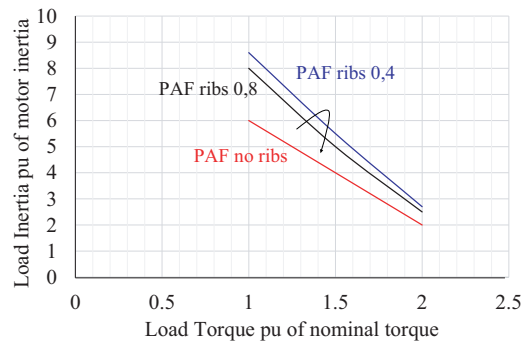
FIGURE 4.15: Synchronizing capability varying the reluctance properties

4.4　LSSyR Design Guideline

In the previous section is investigated the transient run-up of the machine, putting in evidence how to improve the synchronizing capability of the LS motor. It is shown that the improvement of the aluminum section near the airgap produce high benefit on the increment of the pull-in of the motor.

The increment of the reluctance component presents a range where the increment of the pull out torque, and consequently the oscillating component is higher than the reduction of the slope due to the increment of the asynchronous reluctance component, with positive effect on the pull-in. The fact that the reluctance property should be designed properly for the synchronizing capability is not acceptable; because the reluctance performance are responsible of the steady state performance, torque density, efficiency that higher it is, lower are the operating cost of the machine. By this way like in Fig 4.16 the flow chart shows that is necessary to maximize the reluctance property in order to maximize the steady state performance, this can be obtained designing a multi-barrier rotor. Following the flow chart, once is found the optimal SyR motor with the desired efficiency; it is necessary to design the rotor cage. The first step can be obtained full-filling the flux barriers with aluminum, than the aluminum quantity can be reduced if necessary, starting from the inner flux barriers and leaving the barrier near the airgap with much aluminum as possible.
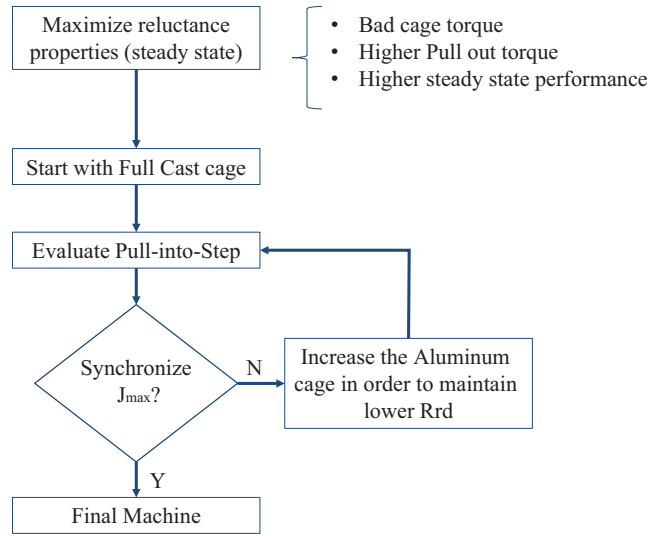
FIGURE 4.16: LSSyR design guideline flowchart

4.5 Design and experimental results of two prototype

Two prototypes were build in order to experimentally investigate the synchronizing capability and performance of LSSyR motor. The two prototype are shown in Fig.4.17 the two solution are called FUF (Full Filling) and PAF (Partial Filling). The PAF solution presents an equivalent amount of aluminum for the rotor cage to the competitor induction motor.
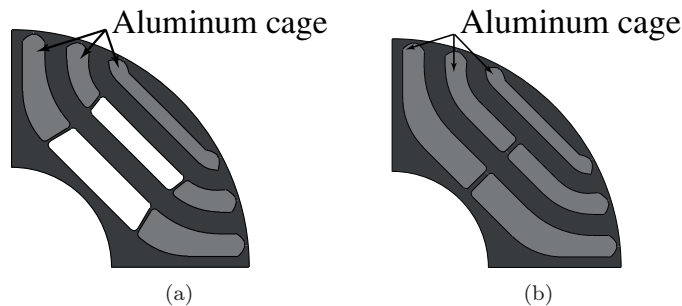
FIGURE 4.17: Rotor cross section near to the real prototype of (a) PAF solution (b) FUF solution

4.5.1 Experimental Setup

Figs.4.18 shows the experimental setup. A three phase Variac, supplies the motor under test, so to include in the experimental analysis reduced line voltage conditions. A regenerative PM synchronous motor drive is used as load, torque control. The load machine is equipped with an incremental encoder and a shaft accelerometer (BaumerHübneracc74) for emulation of additional inertia. The experimental equipment includes a HBM T40B torque transducer and an HBM Gen3i data recorder [21], for acquisition of all electrical and mechanical variables (voltages, currents, speed, and torque). The machines under test are 7,5kW, and rated speed is 1500 rpm at 50 Hz, designed for pump applications, [22].
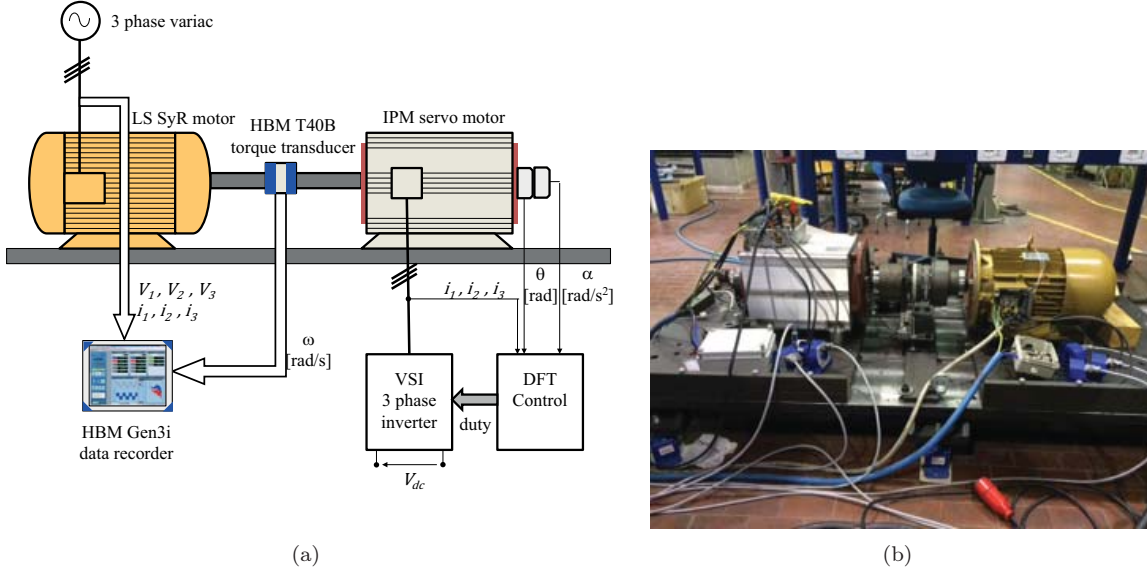
FIGURE 4.18: (a) Test bed connection (b) photo of the test bed in laboratory

4.5.2 Synchronizing Capability, experimental identification

The synchronization capability of the two LS-SyRM prototypes is summarized in Fig.4.19. The maximum value of the synchronized inertia $(J_{tot,0} + \delta J)_{max}$ is reported for each value of the steady-state torque. Maximum inertia is expressed in per unit of the motor inertia. Load torque is normalized to rated torque. All tests refer to rated line voltage conditions. The area of the plane above the pull-in characteristic represents the plan couples (Load Torque vs Inertia) unsyncable. Cold conditions (room temperature, windings at 34 °C) and hot conditions (windings at 65°C, from temperature probes mounted on windings end connections) are compared in Fig.4.19, revealing the significant sensitivity of the FuF prototype characteristic to operating temperature. Hot conditions refer to pull-in tests run just after two hours of preliminary warm up at rated speed and load. Hot conditions are relatively mild, due to the IE4-class efficiency of the two prototypes. After two and a half hours, the temperature reaches a steady level of 67 °C. As said, temperature increase leads to degradation of the pull-in performance Fig.4.19.

4.5.3 Asynchronous characteristics

The asynchronous torque was evaluated with the MUT machine line supplied, the DM is speed controlled to impose a slow speed ramp, torque is measured with HBM Gen3i datalogger. With reference to Fig 4.20, the blue cloud of torque values represents the superposition of cage torque (asynchronous motor torque, mean value highlighted in red) and reluctance torque, which is alternated when out of synchronous speed (ac component of the blue trace). In the final part of the test, around 1500 rpm, the load torque is released and the MUT naturally evolves towards idle synchronous conditions. The test of Fig.4.20 is repeated for the two motors under test at different voltage levels. The resulting asynchronous torque curves are reported in Fig. 4.22b. Despite the reduced rotor cage and the lower synchronization capability, the PaF motor presents a significantly higher asynchronous torque.
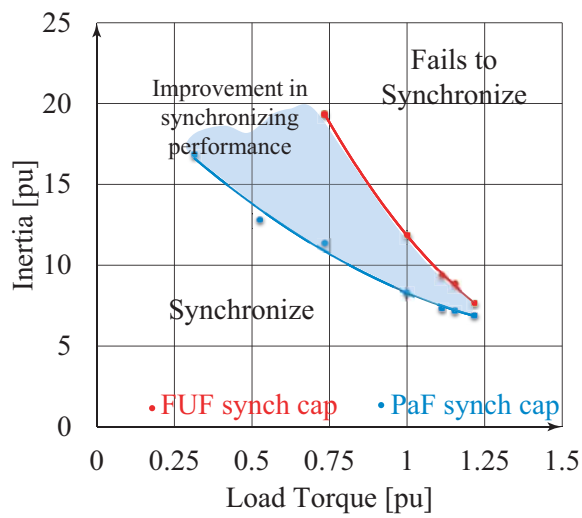
(a)
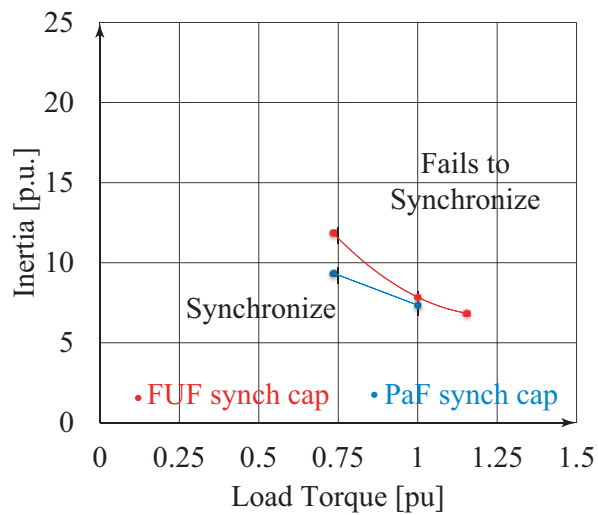
(b)

FIGURE 4.19: (a) Synchronizing capability at copper temperature of 34°C (b) Synchronizing capability at copper temperature of 65°C
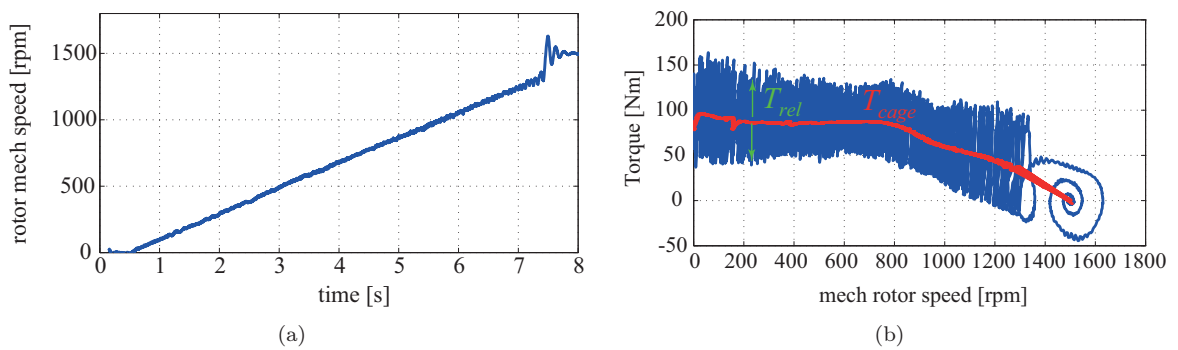
(a)
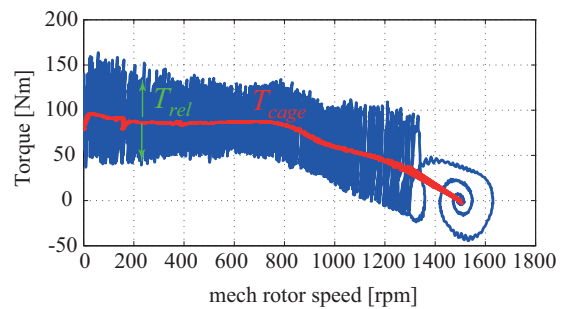
(b)

FIGURE 4.20: (a) rotor speed ramp for experimental cage torque evaluation (b) Transient cage torque experimental measurement

The aluminum cage of the PaF machine is well designed, in terms of starting torque capability. Moreover, the combination of Figs.4.19 and (4.21) also says that the starting torque (asynchronous torque) is not the key factor of synchronization, as the machine with lower cage torque (FuF) finally has the better line start capability. In conclusion: synchronization comes mainly from the reluctance torque, and the FuF is slightly superior in this sense. In Fig.4.21b, is shown the comparison between the experimental curve of FuF motor and the corresponding FEA results. It is possible to see that is necessary to increase the temperature of the cage in order to reach better correspondence between the experimental results and FEA. This is related to the not modeled end ring resistance and inductance in the FEA model. This component can be identified only with 3D FEA with higher computational time. On the other hand is possible to see that increasing the cage temperature is possible to match the experiment in cold condition.
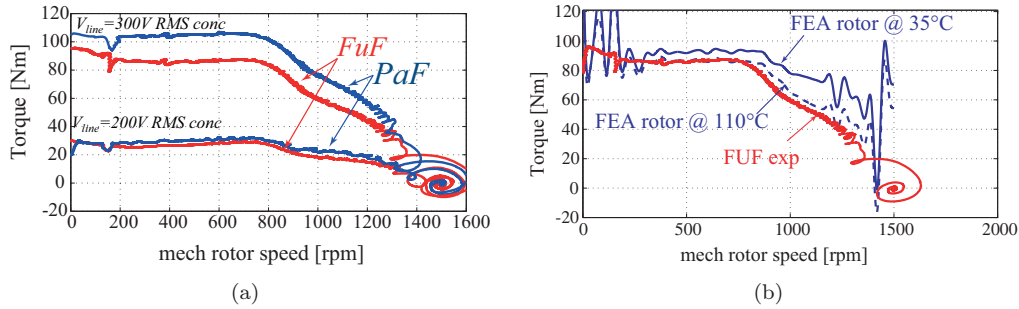
FIGURE 4.21: (a) Average asynchronous cage characteristics for PaF and FuF (b) FEA and experimental comparison of FuF motor

The behavior of the asynchronous torque illustrated in Fig 4.21a, is due to two main effect. First, the variation of the cage parameters related to the reduction of the amount of aluminum passing from the FuF solution to PaF. This reduction is done according to the reported analysis in previous section, where is shown that maintaining the smaller flux barrier near the airgap full filled with aluminum is a good way to obtain a high slope of the cage torque near the synchronous speed. The mechanical resistance during the die cast process impose to double the radial ribs of the PaF solution, this penalize the reluctance performance. Second, the FuF motor presents higher average asynchronous reluctance torque,see Fig.4.6, that tend to reduce the slope of the total asynchronous characteristic near the synchronism. The machine on the other hand maintain higher synchronizing performance, related to the higher reluctance component. That increase the oscillating behavior, giving more energy to the system to jump over the synchronous speed. It is possible to see in Fig4.21a, that in the final part near the synchronism the circle described by FuF are higher than PaF.
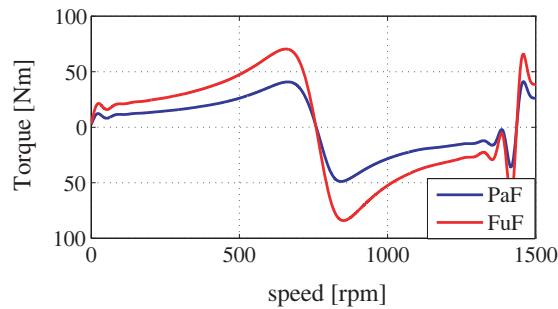
FIGURE 4.22: Asynchronous reluctance cage torque (no cage) FEA evaluated

4.5.4 Bottom Line on Synchronizing Capability

The synchronizing capability of the two prototypes are FEA investigated and compared with the experimental results. Fig.4.23 shows a good match between FEA and experiments using a cage temperature of 110°C, that is the temperature that permits to find also a good match between the asynchronous characteristics, see Fig.4.21. FEA are computed at the same voltage of the experiments

$V = 365Vrms$ and under same load conditions. This temperature is higher than the estimated rotor temperature according to the procedure in [23], this is related as previously described to the not simulated end ring resistance that require long 3D FEA, and can not be evaluated with simplified formulation. In Fig.4.24a,b are compared the experimental pull in capability of FUF and PAF with FEA; using the results obtained in Fig 4.23 at higher temperature. The pull-in capability at high load become practically the same, this effect can be explained using the asynchronous torque in Fig4.24a. It is evident that at lower load the two asynchronous curve are pretty close, and the higher reluctance property of the FuF solution leads to higher synchronizing capability. Increasing the load, increase also the distance between the FuF and PaF curves. In other words, the FuF presents lower equivalent slope respect to PaF. In this condition the higher reluctance property are cancel by the lower slope of the asynchronous curve and consequently the pull-in capability of FuF is reduced (at higher load) becoming equivalent to the PaF capability.
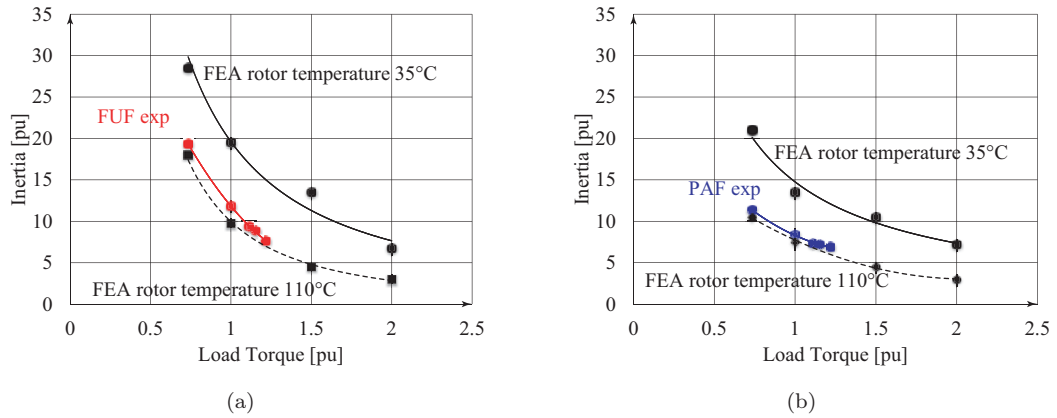
FIGURE 4.23: (a) Synchronizing Capability, comparison between FEA and experiments FuF motor (b) (a) Synchronizing Capability, comparison between FEA and experiments PaF motor
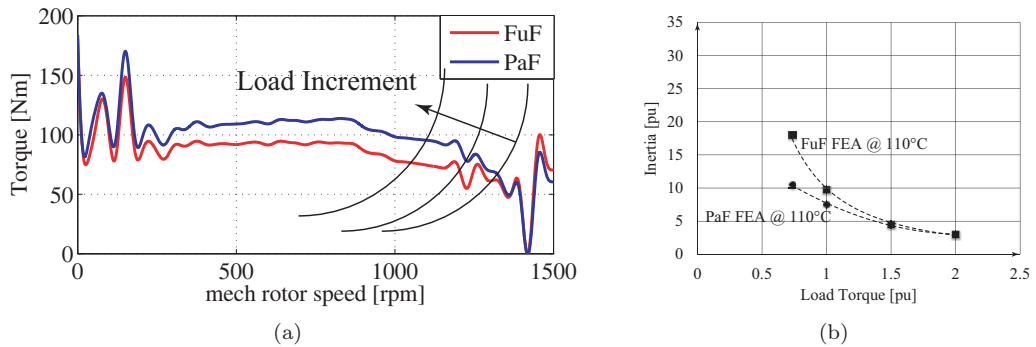
FIGURE 4.24: (a) FuF and PaF asynchronous torque @V=365Vrms FEA (b) Synchronizing capability FEA of FuF and PaF

4.6   Steady State Performance

The magnetic model of the two machines has been identified under vector current control. The constant speed identification technique adopted here is the one described in [24]. The same rig used for previous test has been utilized also for this purpose, thanks to the availability of a second inverter, back-to-back connected with the inverter that is driving the load machine. The flux linkage curves of the two prototypes are reported in Fig.4.25, in $d - q$ synchronous coordinates. The curves are quite similar for the two machines, because the two machines are equal on the stator and rotor flux barrier design, for the die-cast process the PAF solution presents higher iron ribs. However, the higher q flux

linkage of the PaF machine (blue curves) is responsible for its inferior line-start performance. The larger flux linkage in the maximum reluctance direction of the machine is produced by the bigger inter-layer ribs of this prototype. In terms of reluctance torque, the advantage of the FuF prototype is summarized by comparison of pull-out torque profiles 4.25, obtained by manipulation of the flux linkage curves. The Pull-out torque is the maximum torque at given voltage. In conclusion: better is the reluctance motor, better is the line-start capability, even with a worse starting torque coming from the cage. In the used range of voltage the FuF motor present an increment of 15% in Pull out torque respect to the PaF.
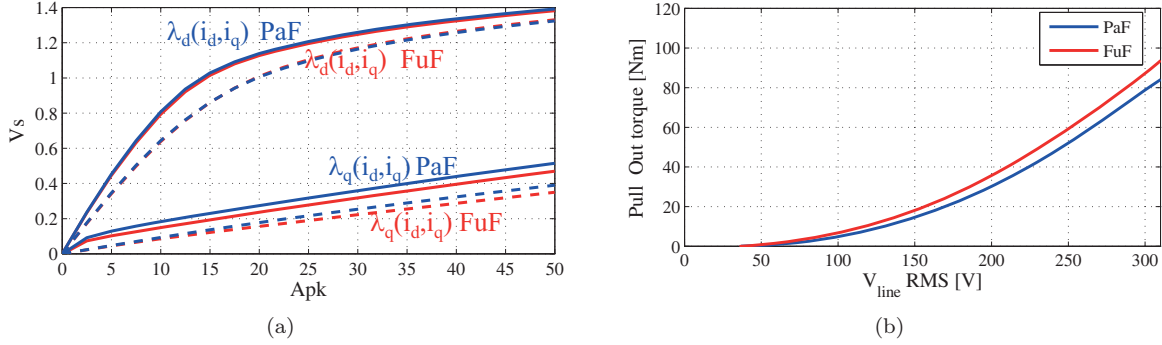
FIGURE 4.25: (a) Flux linkage curves of the two prototypes (b) Pull Out torque versus supply voltage

The steady state performances are described in Tab.4.3, at 360 V line supply and rated load torque conditions. The LS-prototypes are line supplied and loaded via the Drive Machine (DM), which is torque controlled in this case. The PaF prototype needs 1 A more, for the same torque. Power loss, measured as difference between instantaneous electrical power input and mechanical power output is again in favor of the FuF prototype, and so it is for the efficiency. The better efficiency of the FuF machine is justified by its better reluctance characteristics.

	PaF	FuF
Line Voltage	100%	100%
Voltage THD	1,64%	2,13%
Current [Arms]	105,7%	100%
Current THD	6,35%	7,44%
Power Factor	0,721%	0,727%
Efficiency	0,925	0,95

TABLE 4.3: Steady State Operation of the two Prototypes

4.7 Publications

- M. Gamba;G. Pellegrino;A. Vagati;F. Villata ; Design of a line-start synchronous reluctance motor. In: 2013 International Electric Machines & Drives Conference, Chicago, USA, Maggio 2013. pp. 648-655

- M. Gamba; E. Armando; G. Pellegrino; A. Vagati; B. Janjic; J. Schaab ; Line-start synchronous reluctance motors: Design guidelines and testing via active inertia emulation. In: 7th Annual IEEE Energy Conversion Congress and Exposition, ECCE 2015, Palais des Congres de Montreal (Montreal Convention Centre), can, 2015. pp. 4820-4827

Chapter 5

PM-SyR Machines for Traction Application

5.1 Background consideration

Hybrid and full electric vehicles are available on the market. In Tab.5.1, are summarized some of the most used motors in traction application, the higher torque density requested in electric vehicle combined with the advocated highest level of compactness and efficiency leads to the use of Permanent Magnet Synchronous Machines (PMSM), [25]. A recognized benchmark for traction PMSMs is the Toyota Prius 2010 traction motor, an Interior PM (IPM) machine whose characteristics are available to the public [26]. Its cross-section is reported in Fig.5.1, showing two bulky pieces of neodymium-iron-boron (NdFeB or "Neo") magnets per each of the eight rotor poles. After 2010, however, the cost and supply chain uncertainty associated to rare earth PM materials has compelled motor manufacturers to find alternatives to such motors topologies [27], [28].

TABLE 5.1: Comparison between different machine topologies

	SPM	IPM	SyR	IM
Torque phase current [Nm/A]				
Efficiency over complete operating range				
Power overload capability				

This chapter explores the potential of the PM-assisted Synchronous Reluctance (PM-SyR) in traction application, in terms of performance and cost of magnets. In principle, PM-SyR machines have a maximized reluctance torque contribution replacing a substantial part of the PM generated torque, so to cut the cost of PMs significantly. PM-SyRMs can be realized with rare-earth magnets or with ferrite magnets, [29]. Ferrite-SyR machines were proposed for traction application in [27],[28], compared to the IPM motor of a Prius 2003, having a power density of 10kW/liter. It was shown that a ferrite-SyR design can reach 85per cent of the torque of the benchmark, using the same stator [27] and same power in the same stack volume if also the stator is redesigned [28]. However, the IPM machine of the Prius 2010 rose the bar to a peak power density of about 15.6 kW/liter and a peak shear stress of 43kPa, and this is harder to beat with ferrite magnet. The GM Company recently launched its new Chevy Volt 2016 powertrain concept [30], where one of the two electric motors is a ferrite-SyRM, with four layers per pole, filled with ferrite PMs. Although its torque and power density are admittedly lower than the ones of Neo equipped counterparts, such technology was chosen for its convenient efficiency profile, which is steadily high in a large speed versus torque area. The first objective of this work is to establish the advantages and limitations of PM-SyR machines for traction quantitatively, in comparison to the Prius 2010 IPM machine. It will be shown that ferrite-SyR machines cannot beat the Prius IPM machine, whatever the rotor design. The ferrite-SyR machine can match the power at high speed, but then falls short with torque at low speed, and vice versa. This physical limit is demonstrated analytically using the mathematical expression of the characteristic current loading A_{ch} [A/m] of ferrite-SyR machines as a function of their geometry and magnet strength. The equation

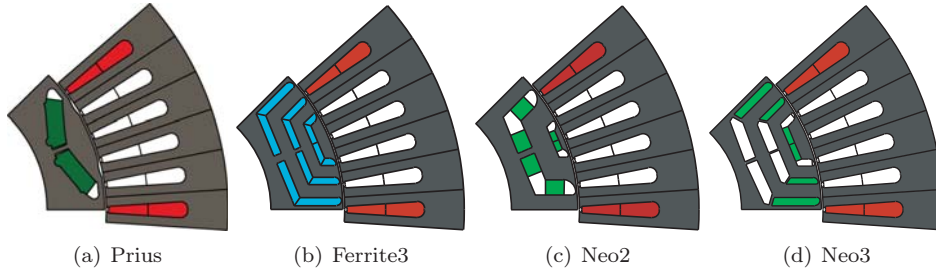(a) Prius   (b) Ferrite3   (c) Neo2   (d) Neo3

FIGURE 5.1: Cross-section of the machines under study

says that the relatively weak ferrite magnet cannot produce a characteristic current loading as high as the one of the Prius IPM machine. This comes after the demanding loading conditions imposed by the application. In the second part of the paper the same modelling approach will be used to quantify the potential of PM-SyR machines with NdFeB magnet against the benchmark. This second part confirms that Neo magnet is mandatory for the PM-SyR technology in this circumstance, unless the constraints on stack dimensions are relaxed. As expected, with Neo magnet the PM-SyR machine can match the performance of the IPM benchmark, and use a lower magnet quantity. The analysis takes profit of a piecewise linear magnetic model of the PM-SyR machine developed for direct-drive ferrite-assisted machines [31]. All designs in this paper use the same stator of the benchmark, so to have the same copper temperature for the same current loading for all machines and then a fair thermal comparison. The results are validated by finite element analysis (FEA), where needed. FEA is also used to build loss and efficiency maps of the considered designs. Stress limits at maximum speed are taken into account in the design and verified with structural FEA.

5.1.1   Design Specifications

Fig.5.1 reports the cross-sections of the Prius 2010 benchmark motor and of four PM-SyRM designs. The Ferrite-3 design of Fig.5.1b has the flux barriers completely filled with ferrite magnet. The three Neo-SyR motors (Neo-2, Neo-3 and Neo-3+) are called *Neo* after NdFeB magnet. Different number of barriers per pole are tested (2 or 3), so to cover a significant number of possible solutions. All designs have in common:

1. the same stator (laminations, stack length and winding) of the Prius 2010 IPM motor;

2. the same power converter;

3. the same thermal constraints (i.e. the same cooling setup);

Reference data is reported in Tab.5.2. The key operating condition used to summarize the aggregate of the Prius IPM machine specifications into a single magnetic design condition is the characteristic current loading. The Prius IPM machine has a pretty high value of current loading in characteristic current conditions, 76kA/m @ 150°C. All PM-SyR competitors need to match or beat this figure. When the characteristic current loading target is met, then performance is comparable in all respects, including efficiency maps.

5.1.2   Characteristic current condition

Besides the primary goal of matching the output torque of the Prius IPM machine using less magnet, the second design goal is that the constant power speed range of the Prius specs, given the power converter rating, is also guaranteed. In turn, the output power specification at high speed reported in Tab.5.2 (40 kW @ 13.500 rpm) should be respected, in flux weakening conditions. The vector diagrams in Fig.5.2 and the torque and power versus speed curves in Fig.5.3 anticipate the results of the chapter. The vector diagram of the Prius IPM machine is in Fig.5.2a, at its characteristic current of 75 Apk at 150°C. The square marker refers to the maximum torque per ampere (MTPA) condition, which is exploited from standstill to base speed. At the base speed the machine voltage reaches the upper limit V_{max}, set by the converter. The voltage constraint imposes that the flux linkage amplitude is progressively diminished at any higher speed level. Therefore, the current vector

is rotated towards the negative d-axis (dashed circle) so to shrink the flux linkage amplitude (dashed elliptical trajectory). By definition of characteristic current (5.1), the flux weakening trajectory will end at zero flux amplitude (circular marker in Fig. 5.2a).

$$I_{ch} = \frac{\lambda_m}{L_d} \quad \Longrightarrow \quad L_d \, i_{ch} = \lambda_m \tag{5.1}$$

Given the maximum voltage amplitude V_{max}, zero flux would mean infinite speed. Correspondingly, the output power tends to the characteristic power (5.2) at infinite speed:

$$P_{ch} = \frac{3}{2} V_{rated} \, I_{ch} \tag{5.2}$$

Where machine losses are neglected and the power factor of the machines tends asymptotically to one [32]. The power versus speed curve of the Prius IPM machine at 75 A pk and $V_{rated} = 337V$ is reported in Fig. 5.3b. Fig.5.2b represents the Neo-2 PM-SyRM design. Purposely, the characteristic current (75 A) and the flux linkage in MTPA conditions (square point) are the same of the Prius IPM machine. Therefore, the flux weakening behavior will be similar, with the flux amplitude ending to be zero. What is different respect to Fig.5.2a is that the magnet flux vector (red vector) is shorter than the one in Fig.5.2a, thanks to the increased reluctance torque. Torque and power curves of Neo-2 at 75 A overlap the ones of Prius, in Fig.5.2a. Finally, Fig.5.2c reports the ferrite-SyR machine case. This one has a L_d, L_q similar to the ones of Neo-2, but with a visibly smaller flux linkage vector. As for the Neo-2 machine, a good SyRM was designed, and therefore its barriers were filled with NMF-12F ferrite. However, the magnet contribution is not enough to meet the target characteristic current condition. In turn, the magnet flux linkage is smaller than the one of Neo-2, and so are the characteristic current (42 A) and characteristic power of Ferrite-3, according to (5.1) and (5.2), respectively. Fig 5.3 reports the torque and power curves of the Ferrite-3 design at its $I_{ch} = 42$ A and at 75 A, showing its lower performance. Torque at 75A is slightly lower that the one of the benchmark, and this gap is retained in the entire speed range (Fig 5.3a). In terms of power, below base speed the power gap is in the same percentage of the torque gap, and then it gets larger in the flux weakening speed range (Fig.5.3b).

TABLE 5.2: Main Parameters of the motor

			PM-SyR		
	Prius	Ferrite-3	Neo-2	Neo-3	Neo-3
Stator outer diameter [mm]			260,0		
Rotor diameter [mm]			160,46		
Pole pairs number p			4		
Airgap length [mm]			0,73		
Stack length [mm]			50,16		
Number of series turns per phase N_s			88		
Target peak power [kW]			60		
Type of magnet	[2]	NMF-12F	Same characteristic as in [2]		
PM Volume [liters]	0,100	0,195	0,0936	0,0913	0,0857
PM cost [USD] and (%) [17]	72,8 (100%)	7,3 (10%)	68,1 (94%)	66,5 (91%)	62,4 (86%)
Maximum Speed [rpm]			13500		
Power at max. speed [kW]			40		
Characteristic current Ich [A] @ 150°C	75	42	75	75	75
Torque at Ich [Nm]	77	32	83	83	83
Maximum Speed [rpm]	13500	13500	13500	13500	13500
Characteristic current loading A_{ch} [A/mm]	76	42,6	76	76	76
Shear stress @ A_{ch} [kN/m2]	38	16	41	41	41
Tooth length/airgap length			42,6		
Pole pitch/airgap length			86		

5.1.3 Effect of the Number of Turns

So far, $N_s = 88$ turns in series per phase, single way, has been considered for all machines. The characteristic current of the ferrite machine can be adapted changing the number of turns to $N_s = 8842A/75A = 50$ turns . In this case, the power at high speed grows, as shown in Fig. 5.4 b. However, torque at low speed is reduced (Fig.5.4a). Vice-versa, using a higher number of turns, $N_s =$
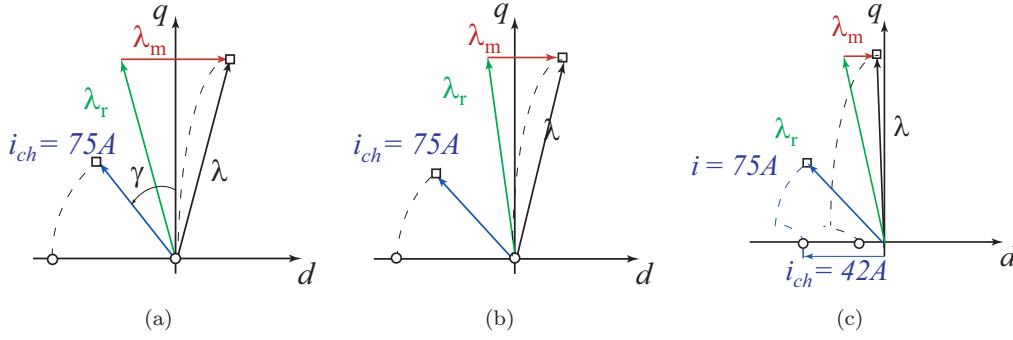
FIGURE 5.2: Vector diagrams at Prius characteristic current conditions. a) Prius
IPM; b) Neo-2; c) Ferrite-3.
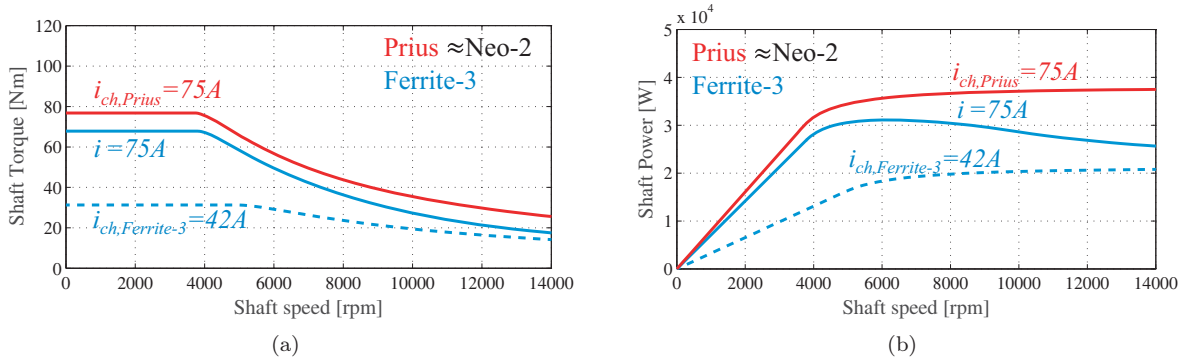
FIGURE 5.3: a) Torque and b) power curves at dc link voltage 650V and 75 A pk
(Prius's I_{ch}), for the three designs of Fig.5.1.

$88(80Nm)/(68Nm) = 104\,turns$, torque grows and power at high speed is penalized (also in Fig. 5.4a).
Whatever the number of turns, the Ferrite-3 design does not match the Prius 2010 performance. In
the following, the current loading (5.3) will be used in place of currents, so to keep into account total
ampere-turns and avoid the ambiguity related to the choice of the number of turns. The current
loading in [A/m], peak, is defined:

$$A = \frac{3}{\pi\,r} k_w\,N_s\,I \tag{5.3}$$

Where r is the air-gap radius, k_w is the winding factor, N_s the number of series turns per phase,
I the stator phase current peak value. The characteristic current loading A_{ch} is the value of current
loading corresponding to characteristic current conditions, when the magnet and armature flux linkages
compensate for each other. The next section gives insight and quantification of the performance gap
between ferrite-SyR machines ant the Prius IPM, using A_{ch} as the metrics of such gap.

5.2   Linearized Machine Modelling

The model developed in [31] for direct drive ferrite-SyRMs is used here to define the characteristic
current loading as a function of geometric parameters and magnet strength and quantity. The fictitious
remanence B_r' [T] is used to calibrate the magnet contribution using a single parameter, as reviewed
later. The lumped parameter model neglects saturation in stator and rotor iron. The rotor ribs are
fully saturated and thus considered linear, magnetic wise. Fig.5.5 shows a sketch of one machine pole.
Flux barriers are circular, have constant thickness, and are full of fictitious magnet having remanence
equal to B_r'. Such parameter can be varied with continuity to produce the needed PM assistance.
Following the model in [31], the barriers ends at the airgap are called rotor slots and are equally
spaced tangentially, meaning that the rotor pitch is equal to $\Delta\xi = 2\pi/n_r$ [rad] (electrical); n_r is the
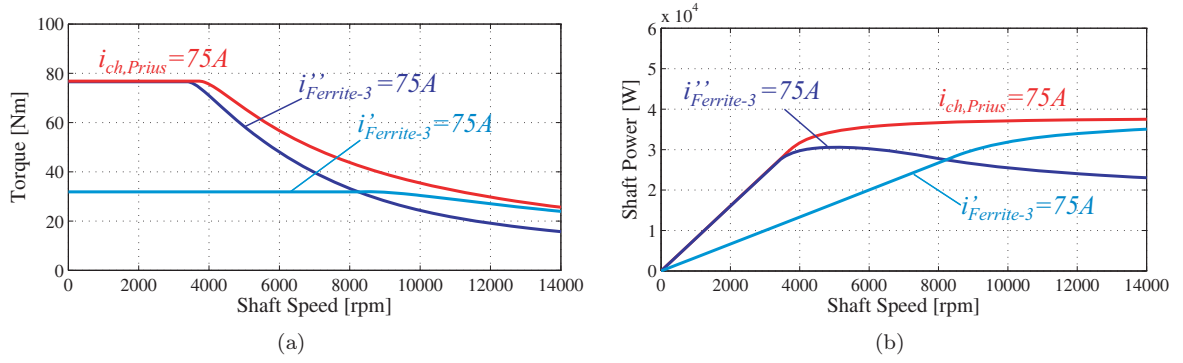
FIGURE 5.4: Torque and power versus speed profiles of Ferrite-3 with $N_s = 88$ and $N_s' = 50$, $N_s'' = 104$.

number of slots per pole pair. The rotor pole pitch is called a [m], after [31]. Finally, results are FE verified.
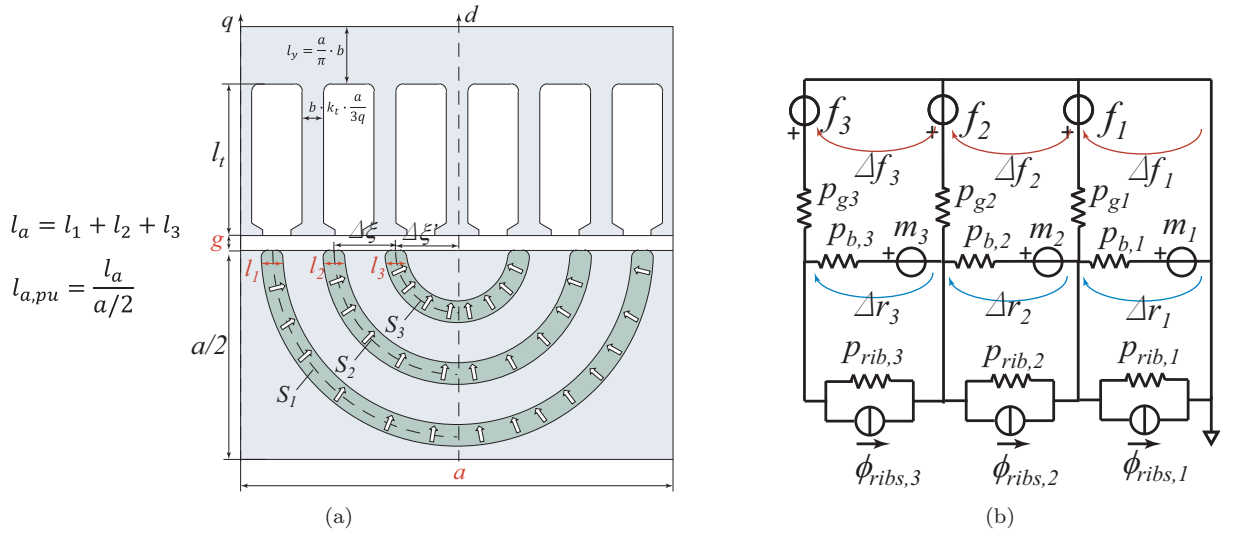
FIGURE 5.5: Schematic section of one machine pole. The magnetic circuital model used for the design is superimposed.

5.2.1 Characteristic Current Loading Equation

The total air length, in p.u. of the half the rotor pitch is:

$$l_{a,pu} = \frac{\sum_{k=1}^{n_{lay}} l_k}{a/2} \tag{5.4}$$

where n_{lay} is the number of layers. This key parameter accounts for total barrier thickness, before barriers are filled with magnet, and appears in all equations in the following. Following the procedure presented in [31], the characteristic current loading turns out to be the ratio between the peak airgap flux density produced by magnet $B_{g,m}$, and the per-unit d-axis inductance [1].

$$A_{ch} = \frac{3\pi}{2\,\mu_0} \cdot \frac{B_{g,m}}{L_{d,pu}} \tag{5.5}$$

---

[1] $L_{base} = \mu_0 L \left(\frac{2}{\pi} k_w \frac{N_s}{p} \right)^2$

The peak air-gap flux density at the numerator of (5.5) is mainly a function of the PM remanence B'_r, the airgap to pole pitch ratio g/a, and the air length $l_{a,pu}$, total air divided by $a/2$.

$$B_{g,m} = B'_r \left(\frac{2}{l_{a,pu}} \frac{g}{a} + \frac{1}{n_{lay} \, \pi \, \sin\left(\frac{\pi}{n_r}\right)} \right)^{-1} \tag{5.6}$$

Other factors in (7.18) such as n_{lay} and n_r are less important than the former three. The d-axis per unit inductance at denominator in (5.5) is the sum of three components: magnetizing (7.21), slot-leakage (5.8) and zig-zag (5.9) inductances.

$$L_{md,pu} \approx \frac{3\pi^2}{4} \frac{1}{l_{a,pu}} \left(1 - \frac{2}{n_r} \right) \qquad \propto \qquad \frac{1}{l_{a,pu}} \tag{5.7}$$

$$L_{\sigma,slot,pu} = \frac{\pi^2}{2\,k_w} \frac{1}{(1 - b\,k_t)} \frac{l_t}{g} \frac{g}{a} k_{tip} \qquad \propto \qquad \frac{l_t}{g} \left(\frac{a}{g} \right)^{-1} \tag{5.8}$$

$$L_{zzd,pu} = \frac{1}{8} \left[\left(\frac{\pi}{3q} \right)^2 + \left(\frac{2\pi}{n_r} \right)^2 \right] \frac{a}{g} \qquad \propto \qquad \frac{a}{g} \tag{5.9}$$

In (5.8), b is the ratio between airgap flux density and back iron flux density (stator yoke), k_t is the ratio between yoke and tooth flux density and $k_t ip$ (tooth tip factor) takes into account the increment of slot leakage inductance due to the tooth tip. In (5.9) q is the number of slots per pole per phase. As for (7.18), the key design quantities in (7.21)-(5.9) are again a/g, $l_{a,pu}$ and B'_r. Another significant factor is the tooth length l_t that is equal for all the designs, because the stator is the same for all. The same is true for the p.u. airgap, because all the designs have the same airgap and pole pitch lengths. The Prius stator and airgap figures give $g/a = 1/86$. Bottom line is that with the stator design constrained as it is here (a/g and l_t are constants), the characteristic current loading is a function of the magnet grade B'_r and the air thickness $l_{a,pu}$.

5.2.2   Results with Ferrite Magnet

Fig.5.6a reports the characteristic current loading as a function of a/g, calculated with (5.5)-(5.9). The insulation factor $l_{a,pu}$ is used as parameter and B'_r is equal to 0,35 T, to account for the NMF-12F ferrite grade at 150°C. Other data used to build Fig.5.6 are in Tab.5.2. The circular marker spots the Prius IPM conditions, having $a/g = 86$ as said, and a characteristic current loading of 76A/m, at 150°C. The curves in Fig.5.6 show that:

1. The characteristic current loading of the ferrite-SyR solution is below the target, if a/g is the same of Prius;

2. A different a/g combination could increase the A_{ch} of the ferrite-SyR. For example, a higher value of a/g (smaller airgap or larger rotor radius) would produce advantages in this sense;

3. Increasing $l_{a,pu}$ increases the volume of air and therefore the room for ferrite and it is beneficial to the A_{ch}, but this has to be traded-off with the quantity of steel dictated by the constrained stator. Using the Prius IPM stator, the maximum reasonable insulation is $l_{a,pu} = 0.3$;

4. Increasing the remanence to 0.4 T would increase the current loading, but 0.35 T is a more realistic value at 150°C, same temperature considered for the Prius IPM machine.

5. Other changes, such as redesigning the stator with a different slot/tooth width ratio, do not change the conclusion of Fig.5.6a substantially.

Altogether, ferrite magnets cannot meet the target set by the Prius 2010 IPM motor, unless the dimensions of the stack are increased. Under the design constraints used in this study, the characteristic current loading of a Ferrite-SyR machine is 56% of target one (red curve at $a/g = 86$), according to the simplified magnetic model. This confirms the power curves of Fig.5.3b, where the characteristic power of the Ferrite-3 design is 56% of that of the Prius motor, both FEA calculated.
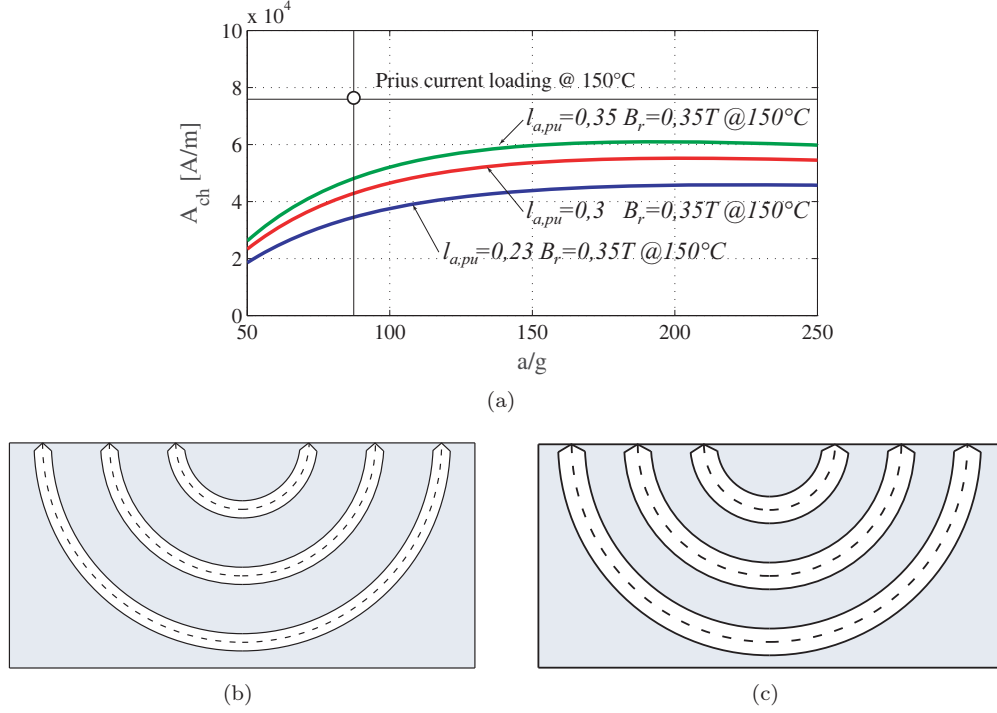
(a)

(b)   (c)

FIGURE 5.6: a) Characteristic current loading of Ferrite-SyRM having the Prius IPM Stator. b) cross section of rotor with $l_{a,pu} = 0.23$ and c) with $l_{a,pu} = 0.35$

5.2.3 Results with Stronger Magnet

To beat or match the Prius IPM machine, a stronger magnet would be needed. If B'_r could be set to $0.5 - 0.6$ T, then the A_{ch} curves of Fig.5.6 would shift upwards to meet the target, as shown in Fig.5.7. The Prius A_{ch} target is met with B'_r values spanning from 0.50 T to 0.62 T, depending also on other parameters. The three curves in Fig.5.7 are representative of the three Neo-SyRM designs Neo-2, Neo-3 and Neo-3+ of Fig.5.1, as explained later. All designs were tailored to give the same A_{ch} of the Prius IPM, with different numbers of layers and different total insulation. The volume of fictitious magnet, equal to the barriers volume Va, is reported in Fig.5.7b. This was evaluated under the simplifying assumption of circular barriers (Fig.5.5a):

$$V'_m = V_a = 2p \, L \, 2 \sum_{k=1}^{n_{lay}} S_k \, l_k \approx \frac{\pi^2}{2} \, p \, a^2 \, L \, l_{a,pu} \, \frac{n_{lay}}{n_r} \tag{5.10}$$

Where V'_m is the volume of the weak magnet, equal to the total volume of the barriers V_a.

The circa in (5.10) refers to the assumption of regular rotor pitch ($\Delta\xi = \Delta\xi'$ in Fig.5.5). V'_m is mainly a function of $l_{a,pu}$ and the number of layers; n_r is strictly related to n_{lay}, in Fig.5.7b is shown the linear relation between the fictitious magnet volume V'_m, and $l_{a,pu}$ at the same pole pitch of Prius motor (in the first part of the paper is underlined no variation on stator and rotor dimensions, respect to Prius data), the three designed Neo-SyR motors are put in evidence(circular marker). The choice of lower $l_{a,pu}$ reduce also the magnet volume, the sensitivity of the variation of V'_m to $l_{a,pu}$ is higher than the variation to the number of layers. The fictitious magnet volume turns into an equivalent quantity of Neo magnet as addressed in the next subsection.

5.2.4 Equivalence between Fictitious and Final Magnet

The modelling approach based on the fictitious remanence B'_r is extended here to the case of Neo-SyR machines, having a much stronger magnet and the barriers space not filled completely. The two situations are schematized in Fig.5.8, where a single barrier is represented. This is at first filled with a magnet with remanence B'_r (Fig.5.8a) and then partially filled with an equivalent quantity of stronger magnet ($B_r > B'_r$, Fig.5.8c). The respective magnetic circuit networks are in Figs.5.8b and 5.8d. Saturated ribs are included. It is assumed that both magnet types have the incremental permeability
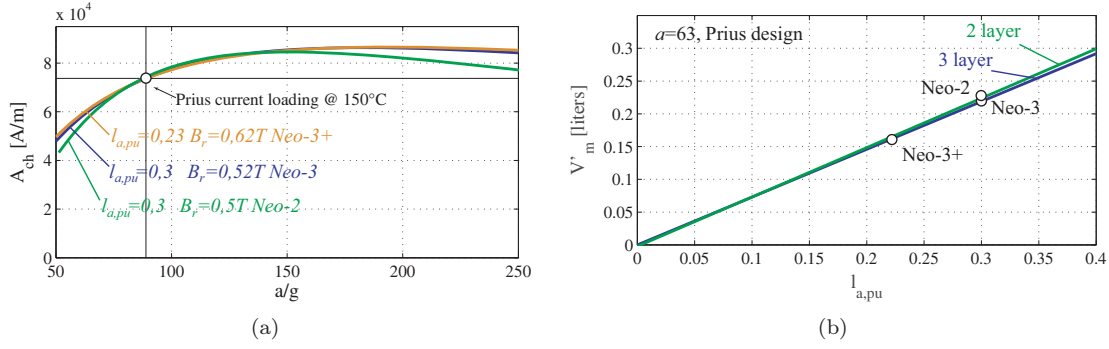
(a)   (b)

FIGURE 5.7: (a) Characteristic current loading for the case Neo-2, -3, -3+,for the
three designed machines. It is shown the B_r' value necessary to reach the Prius current
loading; (b) Fictitious magnet volume function of pu pole pitch a/g and $l_{a,pu}$.

equal to that of vacuum, μ_0, as reported in the circuits. The two magnetic circuits are equivalent if
the condition (5.11) is met:

$$m_k' = m_k \frac{S_{mk}}{S_k} \tag{5.11}$$

This comes from the Thevenin's equivalent of the circuit in Fig.5.8d. Manipulating (5.11), and
putting in evidence the stack length L, the magnet volumes ratio is found.

$$\frac{B_r}{B_r'} = \frac{S_k}{S_{mk}} \frac{l_k}{l_k} \frac{L}{L} = \frac{V_m'}{V_m} \implies V_m = \frac{B_r'}{B_r} V_m' \tag{5.12}$$

Where V_m', is the volume of the weak magnet, equal to the total volume of the barriers, and $V_m <
V_m'$ is the volume of the strong magnet. Neglecting the magnetic saturation, the simple equivalence
(5.12) applies to any flux barrier individually and therefore to the entire magnet volume. Moreover,
replacing the fictitious magnet with the stronger one produces no change of machine performance:
flux linkages, inductances, and torque remain the same.

5.2.5   Final Magnet Volume

Fig.5.7 tells that the same A_{ch} of the Prius IPM machine can be reached with different combinations
of fictitious magnet and insulation (i.e. air volume). Now, the Neo grade of the Prius is imposed to
the PM-SyRM designs ($B_r = 1{,}08$T at 150°C, from [26]) and the fictitious magnet is translated into
the final Neo grade by means of (5.12). The final magnet volume V_m, coming from (5.10) and (5.12)
is reported in Fig. 5.9, as a function of $l_{a,pu}$, with A_{ch} imposed to 76A/mm. The number of layers is
a parameter. Fig. 5.9a shows that:

1. $l_{a,pu}$ strongly influences the final magnet volume;

2. To a minor extent, also the number of layers has effect on the volume: using three layers is
   convenient respect to using two layers.

The positions of the three designs Neo-2, Neo-3 and Neo-3+ are indicated in the figure. FEA validation
is also reported in Fig.5.9b. Fictitious and final magnet volumes of the three designs are reported,
and model and FEA results are compared. Both model and FEA confirm that:

1. the Neo-3+ design is the one with the minimum magnet quantity, because of its thinner barriers
   (smaller $l_{a,pu}$);

2. the number of layers does not produce substantial differences.

The main discrepancy between model and FE comes from volume overestimate by the model,
because the final barriers of Fig.5.1 are not circular as the ones of the model of Fig.5.8a. Altogether,
the magnet volume estimate coming from the model is consistently $10 - 12\%$ greater than the FEA
calculated one. The errors on V_m' and B_r' for the 2-layer machine are bigger than the ones for the
3-layer machines, because the model works better with higher numbers of layers. However, the final
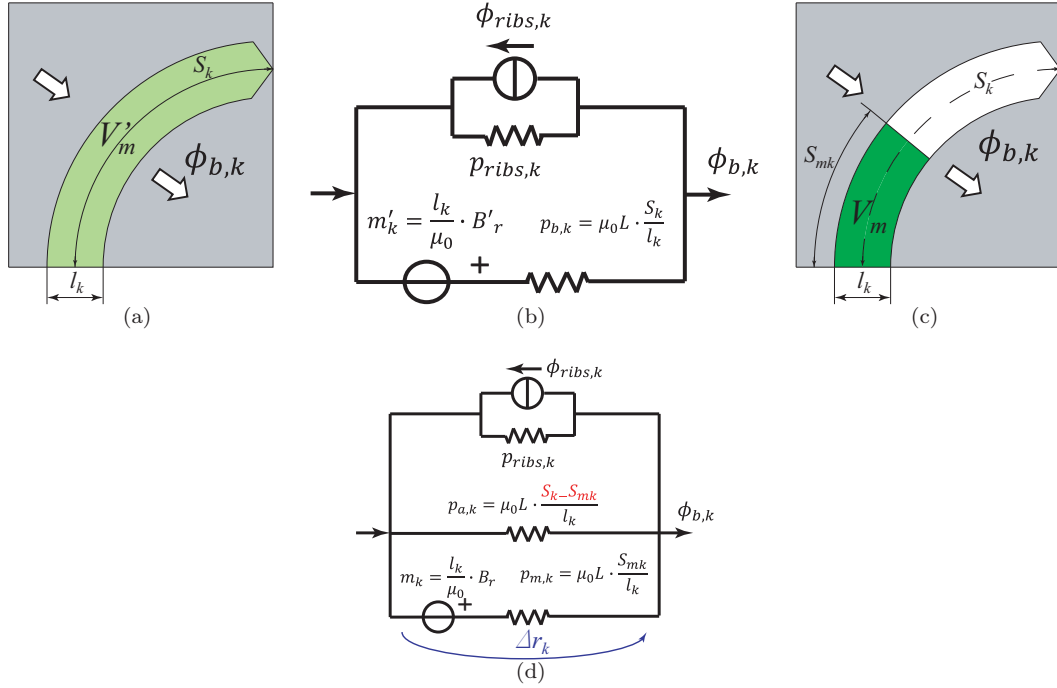
FIGURE 5.8: Illustration on of the equivalent permeance model of a barrier partially filled with magnet, a) barrier cross section in equivalent full filling condition, b) permeance network of the equivalent full-filled solution, c) cross section of partial filled solution d) permeance network of partial filled case

magnet volume is well estimated also for the Neo-2 design. To conclude, the Neo3+ design can match the Prius IPM performance using 86% of its magnet volume, as reported in Tab.5.2.

5.2.6 Risk of Demagnetization

The risk of demagnetization is one possible side effect of using thin barriers as in Neo3+. Fig.5.10 illustrates the operating conditions of the Prius IPM machine in the B-H plane of the considered Neo grade. The flux density at 150°C is evaluated at the characteristic current level of 75 A and the maximum inverter current of 250 A. Corresponding values are reported for the Neo-3+ design, that is closer to demagnetization because of its thinner magnets. The results are FEA calculated, considering the weakest point of all magnets of each machine. The other machines (Neo-2 and Neo-3) where designed to have the same margin of the Prius IPM one, against demagnetization. To give better insights of the FEA results of Fig.5.10, the magnet flux density is expressed analytically using the model in [31]. The magnetic circuit network of Fig5.5b is used to calculate the magnetic potential difference across each rotor flux barrierΔr_k. Then the magnet operating point B_m is calculated for the k-th barrier, divided by the magnet remanence B_r.

$$\frac{B_{m,k}}{B_r} = \left(1 - \frac{\Delta r_k}{m_k}\right); \qquad k = 1, 2, \dots n_{lay} \tag{5.13}$$

After manipulation, the flux density under open circuit conditions B_{m0} is found (5.14), the same for all values of k.

$$\frac{B_{m0}}{B_r} = \left[1 + \frac{S_1^*}{a} + \frac{2}{l_{a,pu}}\left(\frac{a}{g}\right)^{-1} n_r \sin\left(\frac{\pi}{n_r}\right)\right]^{-1} \qquad where \quad S_1^* = S_1\left(1 + \mu_0 \frac{S_{rib,1}}{S_1}\right) \tag{5.14}$$

The expression of magnet flux density as a function of current loading A follows:
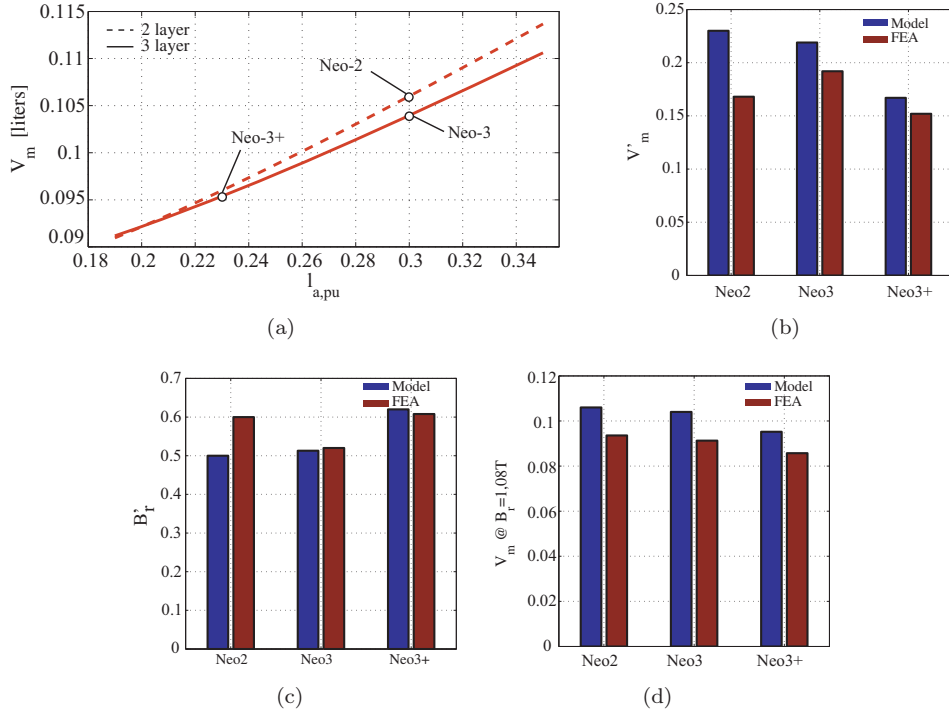
FIGURE 5.9: (a) Magnet volume function of the p.u. air length in the rotor, (b) Model and final designed FEA air volume (14), (c) fictitious magnet remanence and (d) final magnet volume with remanence Br=1.08T (13).

$$\frac{B_m}{B_r} = 1 - \left[1 - \frac{B_{m0}}{B_r}\left(1 - A\left(\frac{\pi}{2}\, l_{a,pu}\,\frac{B_r}{\mu_0}\,\frac{S_{m,1} + B_{rib}/B_r\, S_{rib,1}}{S_1^*}\right)^{-1}\right)\right]\frac{S_{m,1} + B_{rib}/B_r\, S_{rib,1}}{S_1^*} \quad (5.15)$$

B_{rib} in (5.15) is the flux density in the saturated iron ribs, $S_{rib,1}$ is the rib thickness. Details are in [31]. Equation 5.15 is quite complicated, but the important variables that affect the B_m value are the current loading A, the insulation factor $l_{a,pu}$ and the number of layers. Fig.5.10b reports the trend of B_m/B_r (5.15) as a function of $l_{a,pu}$, with the number of layers as parameter and with A imposed to 76 A/mm. Expectedly, reducing $l_{a,pu}$ as done for the Neo-3+ design also affects the magnet operating point; reducing the distance from irreversible demagnetization.

5.3   Efficiency comparison

The four PM-SyR machines of Fig.5.1 were FEA designed after the reported analysis. Ferrite3 is a 3-layer machine designed to maximize A_{ch}, given the stator. Neo3 comes from Ferrite3, using an appropriate quantity of NdFeB so to match the A_{ch} target. Neo2 shows the effect of reducing the number of barriers to two. Neo3+ minimizes the magnet quantity, in change of a reduced margin against demagnetization. All designs were developed using resources available online: SyR-e [33]. Core and PM loss have been calculated with Infolytica/Magnet. Scripts for evaluation of torque and power profiles, control trajectories and efficiency maps are also included in [33]. The torque and power curves of all designs are summarized in Fig.5.11. It shows that the torque versus current characteristic of the Ferrite3 design is quite close to the ones of the Neo machines, included the Prius IPM one. Fig.5.11 shows that the output power at limited voltage and current is the same for all the Neo designs, and insufficient with ferrite. The open circuit voltage is reported in Fig.5.11c for all designs. As expected, the ferrite machine has a much lower magnet contribution, and thus a lower open-circuit voltage. Unexpectedly however, the Neo-SyR machines have the same or even higher open circuit voltage respect to the Prius IPM motor. This is not expected from machines having less magnet and more reluctance. The conclusion is that all Neo-SyR designs are quite close to the IPM benchmark,

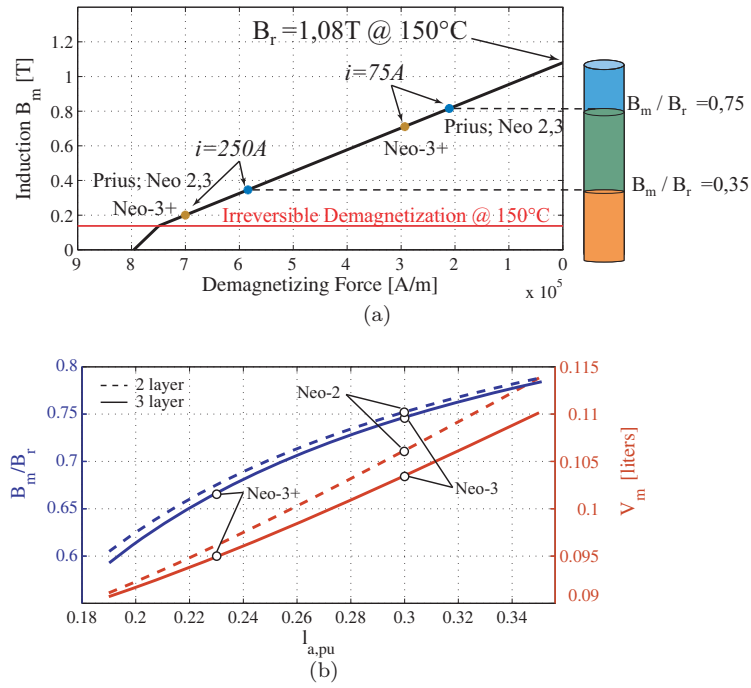FIGURE 5.10: B-H characteristic of the Prius IPM material. Worst case operating points at 75A and 250A are shown for the Prius IPM and the Neo-3+ machines. b) Magnet operating point and magnet volume versus the rotor insulation factor $l_{a,pu}$.
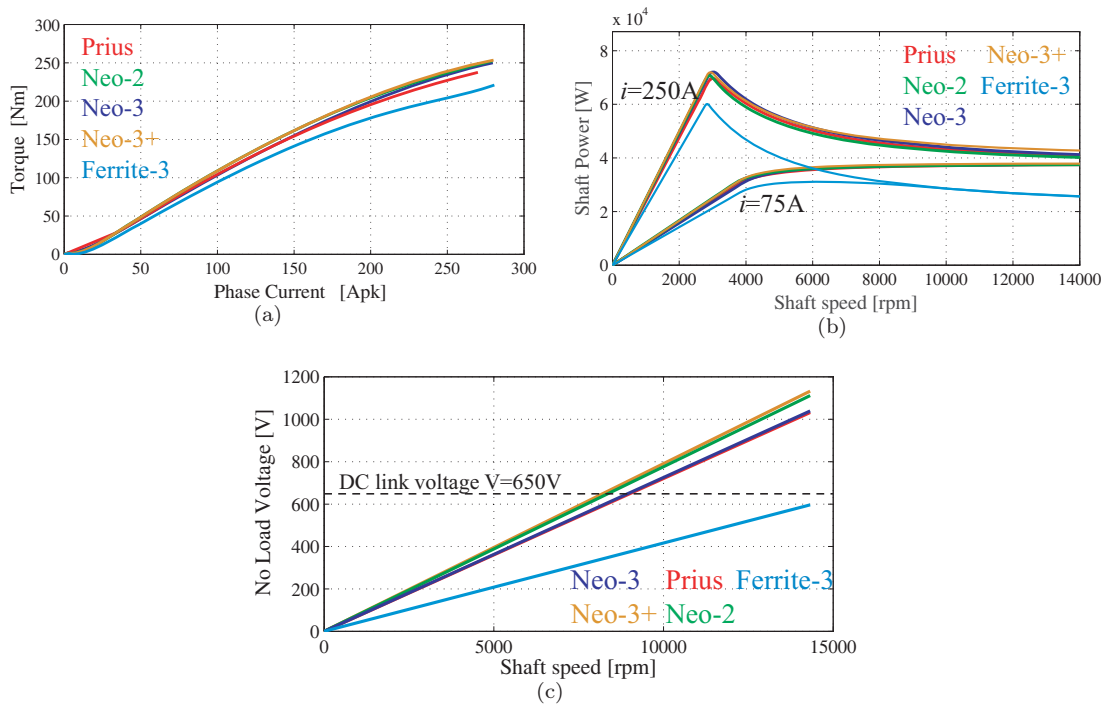
FIGURE 5.11: (a) Torque versus phase current, (b)Power versus speed profile at limited dc link voltage V_{dc}=650V (concatenate peach) (c) No load voltage versus rotor speed

and they can no longer be called PM-assisted synchronous reluctance machines, because the magnet part plays a primary role as in a standard IPM, and the magnet quantity is equivalent to the one of the Prius IPM machine. FEA calculated efficiency maps are compared in this section. The windings and PMs temperature is set to 150°C. Ferrite-3 in Fig.5.12b shows a torque envelope that is lower than all other motors, but with the highest efficiency of all at high speed. Neo-2 and Neo-3+ have a sweet spot at 97% that the others do not have. At high speed, Prius' efficiency is better than Neo-SyR competitors, probably due to harmonic loss in the stator induced by the multi-layer rotors.
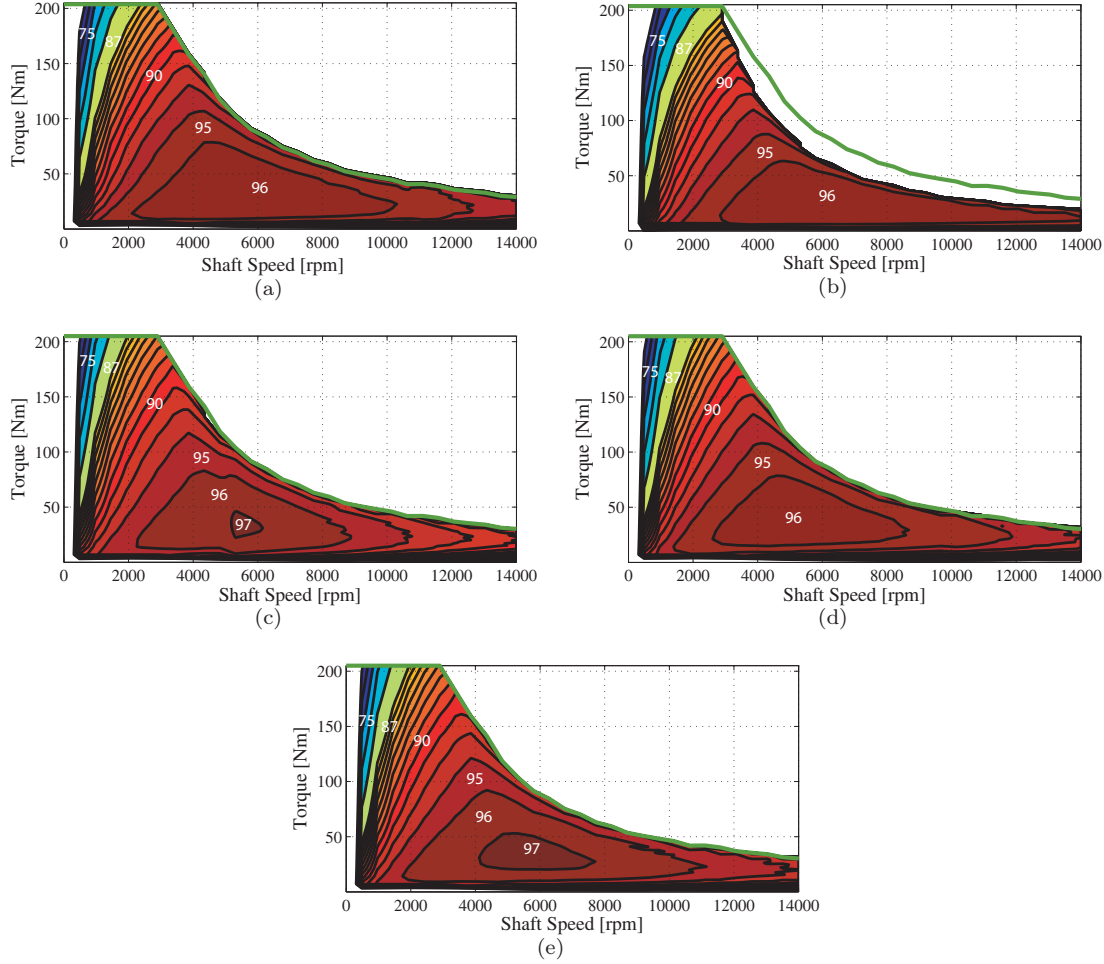
FIGURE 5.12:   Efficiency maps of all considered designs a) Prius IPM, b) Ferrite-3,
c) Neo-2, d) Neo-3, e) Neo-3+.

5.3.1   Pm-SyR motor for traction bottom line

In the previous Paragraph it was shown a comparative study to assess the potential of PM-SyR machines in substitution of IPM motors for electric and hybrid electric vehicle applications. Ferrite and NdFeBr were considered, for the PM-SyR structures. The output limit of Ferrite motors was quantified in a general way, consistent with results shown in the literature. Moreover, the analysis puts in evidence the characteristic current loading as a key figure capable of summarizing the output performance of PM machines for electric power-trains. Finally, it is shown that PM-SyR machines with Neo magnet can be competitive, but with limited advantages in such highly loaded motoring application. The mathematical approach is valid in general and not only for the reported design examples.

5.4 THOR Project: Ferrite-SyR solution for light quadricycle

The motor performance has been evaluated on the basis of US driving cycle US06, used to evaluate the fuel efficiency, exhaust emission of light duty vehicles. The US06 shown in Fig.5.13 combines the city profile with highway driving, providing a more accurate description of the real operating condition of the machines. It includes 4 stops along a 10min, 13 km route with an average speed of 78km/h and a maximum speed of 130km/h. For the analysis it is assumed that the driving cycle has to be performed on a lower size car for urban mobility. Main data of the car are reported in Tab.5.3. A gear box with a 1:8 ratio is used between each wheel and motor. The requested torque vs speed characteristic is evaluated using a simple design procedure [34]. The first step in the vehicle traction modeling is to produce an equation of the tractive effort, considering a vehicle of mass m at a velocity v, up to a slope of angle α, as in Fig.5.14. The total tractive effort is the sum of all the forces in 5.16.

$$F_{te} = F_{rr} + F_{ad} + F_{la} + F_{hc} \qquad (5.16)$$

where:

1. F_{rr} is the rolling resistance force.

2. F_{ad} is the aerodynamic drag;

3. F_{la} is the force necessary to give linear acceleration;

4. F_{hc} is the hill climbing resistance;

The rolling resistance is primarily due to the friction of the vehicle tyre on the road. This resistance is approximately constant and hardly depends on vehicle speed, typical equation is:

$$F_{rr} = C_{rr} \, M \, g \cos(\alpha) \qquad (5.17)$$

Typical value of C_{rr} is 0.015 for radial tyre, down to about 0.005 for tyres developed for electric vehicles. The aerodynamic drag is due to the friction of the vehicle body moving through the air. It is a function of the Frontal Area, see Tab.5.3, ducts and air passages, spoiler, and many other factors. The formula:

$$F_{ad} = \frac{1}{2} \, \rho \, A \, c_x \, v^2 \qquad (5.18)$$

where ρ is the density of the air, c_x is the drag coefficient, see Tab.5.3.

The hill climbing force is the force needed to drive the vehicle up to a slope, the formula is:

$$F_{hc} = mg \, sin(\alpha) \qquad (5.19)$$

If the velocity is changing then a force will need to be applied in addition to the forces shown in Fig.5.14. This force will provide a linear acceleration of the vehicle, the form is the well known Newton's second law $F_{la} = M \, a$

Using eq. (5.16) with previous consideration, it is possible to evaluate the torque required by the electric motor by (5.20). Where n_{motor} is the number of motors devoted to the traction supply, R_w is the tyre radius, η_{tras} represents the transmission efficiency set to 0,95.

$$T_{axle} = \frac{1}{n_{motor}} \, F_{te} \, R_w \, \frac{1}{\eta_{tras}} \qquad (5.20)$$

In the present application the $n_{motor} = 2$ because one motor is set for each axes as shown in Fig.5.14b. Each motor is supplied with two battery modules, with a total amount of four battery modules of global weight of 80kg. The torque vs time and torque vs speed of each motor is shown in Fig.5.13a,b. Due to the high dynamic performance along the driving cycle, the motor reach higher torque for short time, that represent transient overload conditions. The effective utilization is located to lower values. A good indicator is represented by the RMS torque (5.21) that is related to the allowable thermal limit.

$$T_{RMS} = \sqrt{\frac{1}{\Delta t_w} \int_{\Delta t_w} T_{axle}^2 \, dt} \qquad (5.21)$$

Where Δt_w is the time window, T_{axle} as previously explained is the instantaneous torque, and t is the time. The RMS torque shown with red dashed line in Fig.5.13a is about 19Nm (33% of the peak torque).
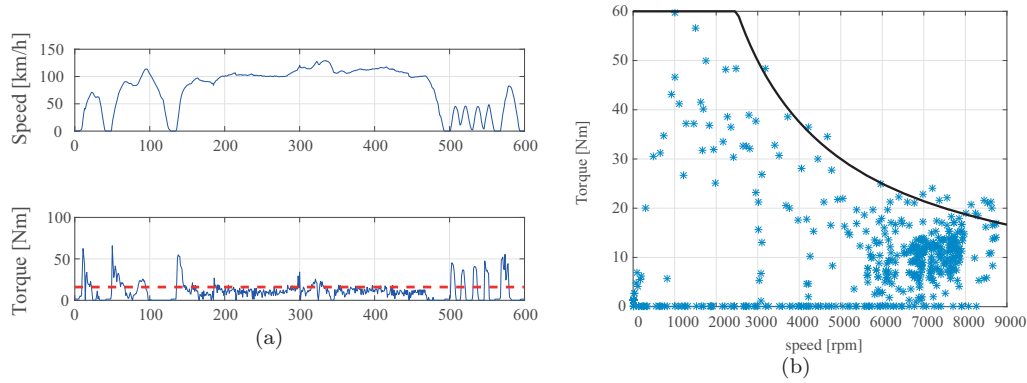
FIGURE 5.13: a) driving cycle b) torque vs speed profile

TABLE 5.3: Main car data

Gross vehicle weight	390 kg +80 kg (battery)
Vehicle load	2x80kg (driver) + 160 kg (baggage)
Frontal Area	$1,85m^2$
Drag coefficient	0,26
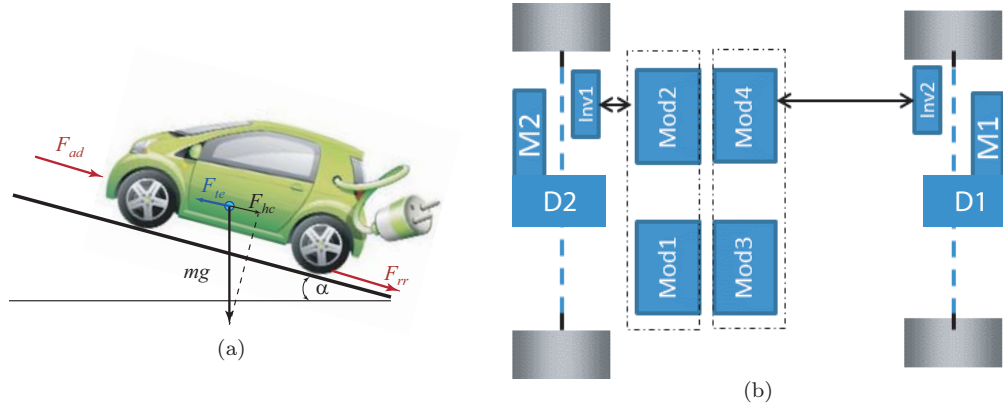
FIGURE 5.14: a) Force acting on a vehicle moving along a slope; b) Thor car power train

Finally the main targets of the traction motor are summarized in Tab.5.5, this data represent the start constraint for the motor design.

TABLE 5.4: Power and Torque characteristic summary

Continuous stall torque	22 Nm
Max stall torque	60 Nm
Continuous Power	7500 W
Peak max torque	13000 W
base speed	3500 rpm
max speed	9000 rpm

5.4.1 THOR Design Steps

The design procedure follows the flow chart shown in Fig.5.15. The first step is represented by the definition of the shear stress. This can be evaluated by the use of tables that summarize the performances of various PM machines, or, like in this case, by the rated expected torque and a prevision of the weight of the motor. The weight of the motor is hypothesized according to the disposable space on the car, see Fig.5.14b. The outer stator diameter is D=170mm the stack length L=120mm. The shear stress is evaluated on the rotor surface, a typical split factor x=0,6 is assumed. The rated torque according to Tab.5.5 is T=22Nm; with this data the shear stress is $\sigma_{rated} = 22kN/m^2$.
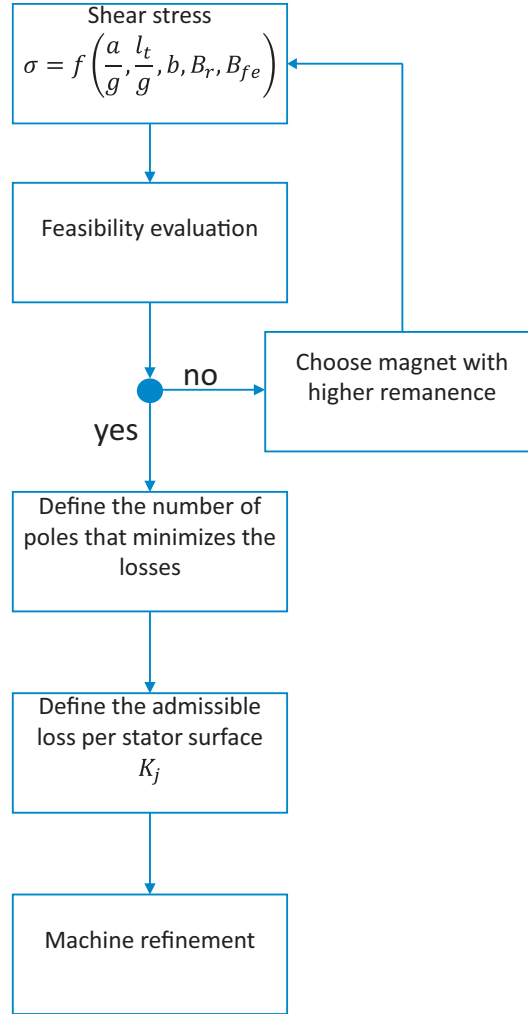
FIGURE 5.15: Ferrite-SyR motor design flow chart

Second step is the evaluation of the feasibility of the selected shear stress with ferrite magnet, see Fig.5.6. For the selected shear stress target, it is feasible the use of ferrite.

The next step is represented by the evaluation of the pole pairs that minimizes the losses. The formulation used are summarized in (5.22) and (5.23). The results show that for high speed machines like motors used in traction application the iron losses leads to solutions at lower number of poles, for the selected frame.

$$K_j = \rho \frac{K_{end}}{K_{cu}\,R} \frac{\pi r^2}{R\,A_s} \left(\frac{A_{\sigma=22kN/m}}{k_w} \right)^2 \tag{5.22}$$

$$K_{fe} = \left[k_h \left(w_{el} B_{fe} \right)^{1,2} + k_e \left(w_{el} B_{fe} \right)^{1,77} \right] \rho_{fe}\, R \left(\frac{V_{stat,Fe}}{2\,\pi\,R\,L} \right) \tag{5.23}$$

The current loading in (5.22) is the one, necessary to produce a shear stress of 22kN/m, it is necessary to underline that this is the total current loading $A = \sqrt{A_d^2 + A_q^2}$ where A_q is related to the magnetic loading (for the selected reference frame), the A_d component is the one evaluated in (5.3).
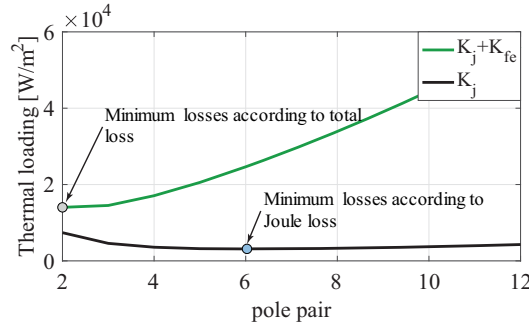
FIGURE 5.16: specific Losses vs pole pair

In step 1 and 2 is evaluated the feasibility of the machine and the optimal pole solution for minimizing the total loss in the machine. The following final step consists in the evaluation of the optimal trade off between the core/copper ratio b, and the airgap split ratio x.

Using equations, from Chapter 1 is possible to evaluate the last point of the flow chart, shown in Fig5.15. In this final part the external dimensions of the machine are defined. The optimal trade-off between the torque production, the power factor and the magnet volume is shown in Fig.5.17ab. The selected solution permits to satisfy the torque requirement, maintaining a higher power factor. The magnet volume is shown in Fig5.17b, in this designing step it is assumed that the flux barriers are full-filled with magnet with remanence $B_r = 0,35T$. The Magnet volume presents a variation with the rotor radius. Lower is the radius, lower is the air section that is feasible in the rotor and so the magnet volume. Also a sensitive variation with b is present, because reducing b at constant rotor radius, means that is possible to reduce the iron section on the rotor, so the magnet volume increase.
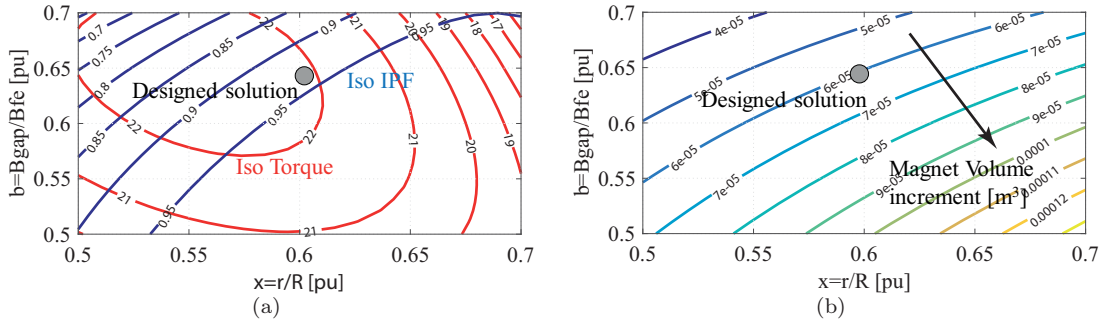
FIGURE 5.17: Torque and IPF in bx plane; b) Magnet volume in bx plane

5.4.2   Rated Performance of the designed machine

The designed motor according to the procedure previously described was built and tested. Fig.5.18b illustrates the cross section of the designed machines. The rotor presents three flux barriers filled with Ferrite magnets. The magnets are sintered ferrite sheet. Three different trapezoidal magnets are present, one for each barrier.

TABLE 5.5: Power and Torque characteristic summary
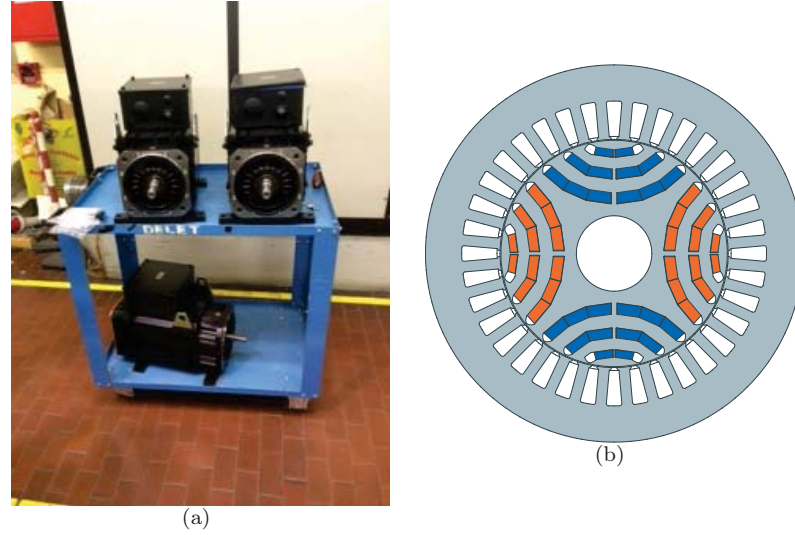
FIGURE 5.18: a) Thor motor prototypes ; b) stator and rotor cross section

Cooling media	Air
Rated voltage dc	110V
Rated Current	$98A_{pk}$
Rated torque	22 Nm
Torque at max speed	9 Nm
Rated Power	7500W
efficiency at rated power	0,92
Weight	22kg
Dim $L\,x\,D_e\,D_{rot}$ [mm]	120x170x102
Airgap [mm]	0,4
max speed	9000 rpm

5.4.3 Magnetic Model identification and Efficiency Test

The test bed is shown in Fig.5.19, the test bed setup consists of a Drive Machine (DM) represented by an IPM motor of 15kW continuous power 9000rpm, vector controlled. The Motor Under Test (MUT) vector controlled by a dSpace board 1103, that send PWM and reference command to a custom inverter with IGBT modules. Current sensors are hall effect sensor LEM with current range from 5A to 200A. Torque and speed are acquired by a torque meter T40B by HBM company. Electric signals and mechanical ones are acquired with a Data Logger Gen3i, by HBM as shown in Fig.5.20. The Drive Machine (DM) is speed controlled. The speed is maintained constant at a value usually around one third of the base value, this is a trade off between the need to rotate slower for having negligible contribution of the iron losses, and high value of v_d and v_q in order to obtain good voltage measurement. For the correctness of the measurement it is necessary that the amplitude of the signal is significantly bigger than the noise. The Machine Under Test (MUT) is current controlled; a grid of dq current references is applied in order to investigate all the working plane of the motor [24].

Once the flux linkages, over the dq plane, are identified with the Magnetic Model Identification procedure. It is possible to evaluate the steady state performance off-line with usual PC and common software like Matlab or Excel. The MTPA and MTPV control trajectory are shown in Fig5.21. they are evaluated respectively by intersection between constant current and constant flux contours with constant torque contours. The torque per Amps and flux vs torque are shown in Fig5.22. This curves can be used by machine designers for consideration on the real performance of the machine or for the implementation of optimal control strategy. Usually in vector current control of synchronous reluctance and IPM machines, MTPA and MTPV trajectories are implemented in look-up tables.

The next step in the test procedure is represented by the efficiency test. This test must be necessarily executed after the MMI, because the control strategy require the knowledge of the motor optimal control trajectories (MTPA, MTPV) and the magnetic model for flux observer in order to

(a)   (b)
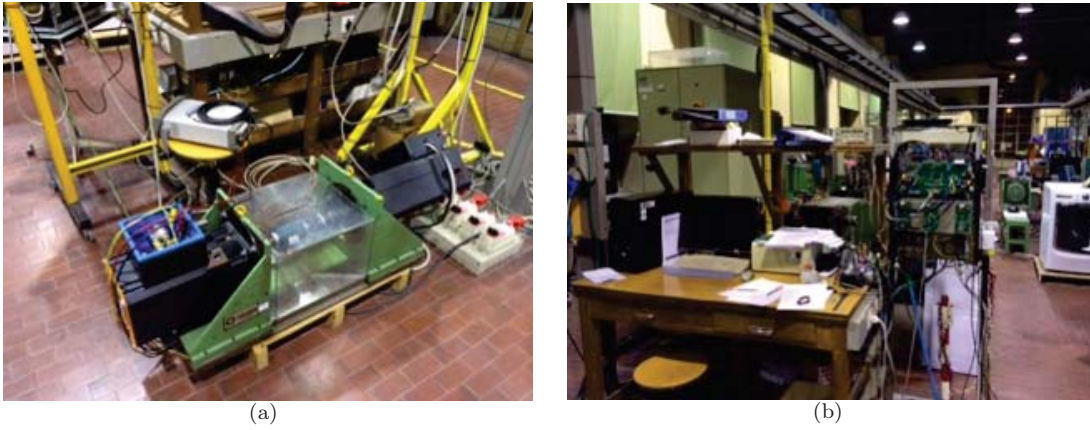
FIGURE 5.19: (a) photo of the test bed showing the machine under test and the drive
machine (b) photo of the inverter used in the test procedure
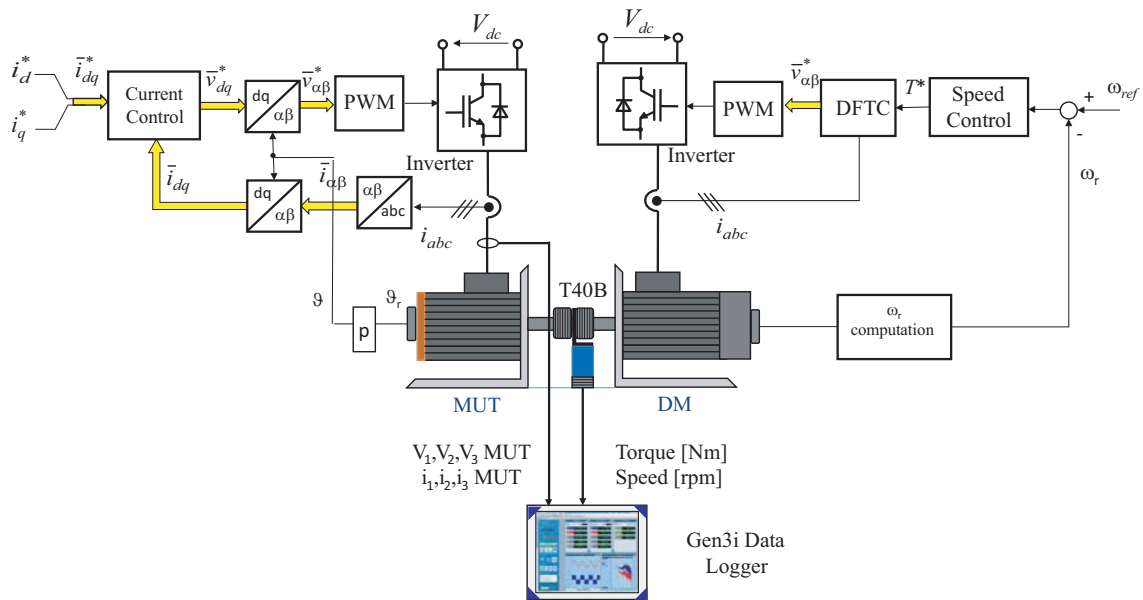
FIGURE 5.20: block diagram of the test bed control scheme for Magnetic Model
identification
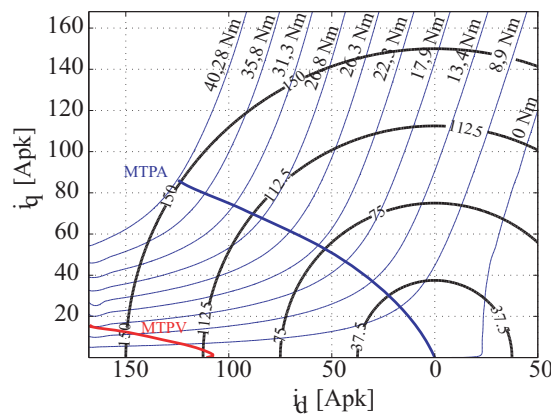
FIGURE 5.21: MTPA MTPV contour in iso current and iso torque plane
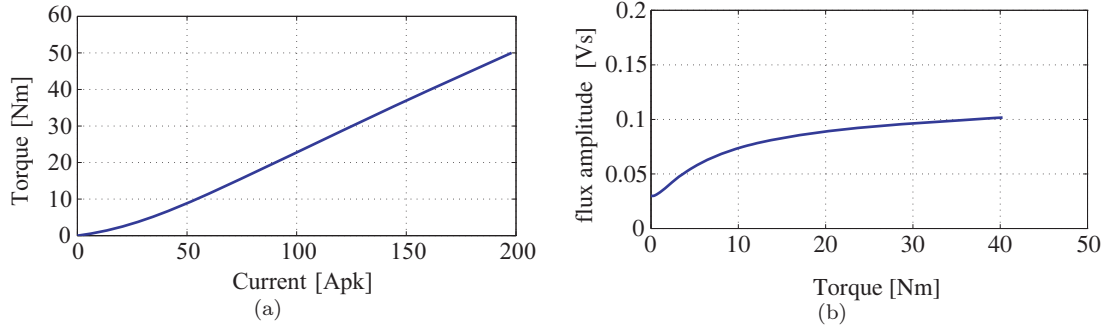
FIGURE 5.22: a) Torque vs phase peak current; b) Flux vs Torque

correctly exploit also the flux weakening region of the MUT. The speed is changed between a minimum value (ω_{min}) and a maximum value (ω_{max}). The speed range (ω_{max}-ω_{min}) is divided into equal intervals of length $\Delta\omega$ that is properly chosen to get a reasonable number of points n (10 to 20). For each speed, the torque is changed between a minimum value (T_{min}) and a maximum value (T_{max}) with steps of ΔT that is properly chosen to get a reasonable number of points m (10 to 20). As a result, the mesh in the torque-speed plane contains N = n x m points.

The DM is speed controlled and provides the speed for one operating point, while MUT is torque controlled. For each operating speed, the torque is changed with steps of ΔT between T_{min} and T_{max}, as shown in Fig.5.24.

The control strategy implemented is the Direct-Flux and Torque Control DFTC,Fig.5.23. This control solution is less model dependent than the current vector control, dealing in particular to the flux weakening behavior. Applying torque step from 0 to 40 at different speed from 100 rpm to 8000rpm is possible to experimentally evaluate the efficiency over the torque vs speed plane, as shown in Fig.5.25. It is possible to appreciate that due to the higher anisotropy higher efficiency can be obtained also at higher speed. The power profile is shown in Fig.5.26 it is possible to see the flat behavior at the rated current, and the overload capability at two times the rated current. A real vehicle was assembled and tested with Ferrite-SyR motor, a picture from the presentation is shown in Fig.5.27.
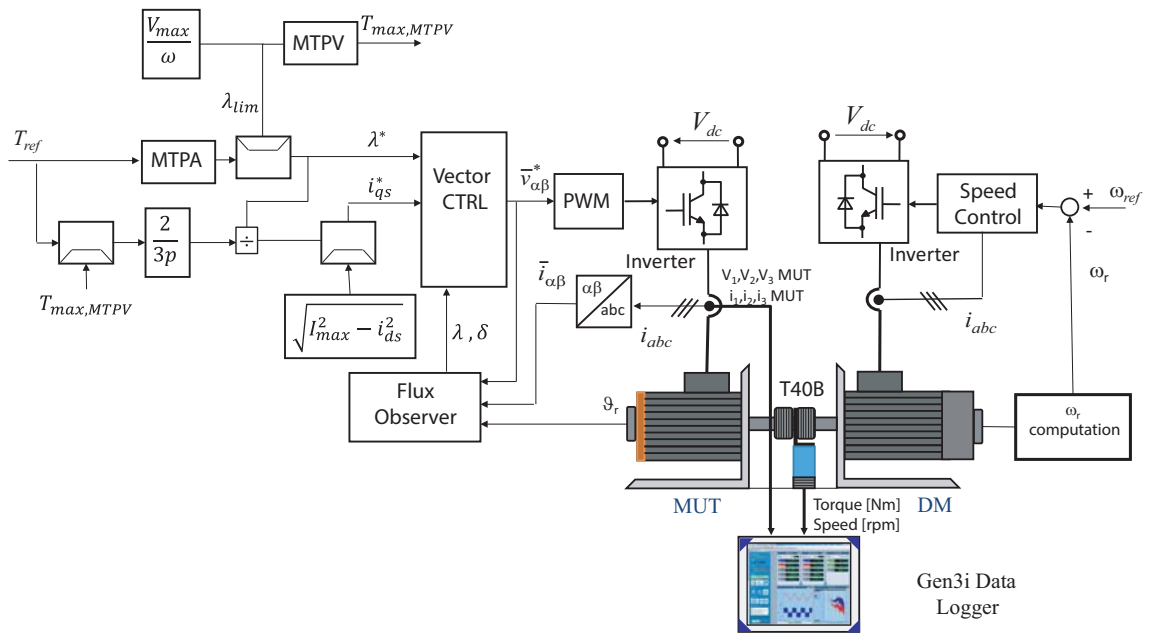
FIGURE 5.23: Direct Flux Vector Control strategy used for efficiency test

(a)   (b)

FIGURE 5.24: a)Mesh of operating points in the MUT torque-speed operating plane;
b) Generation of the DM reference speed and the MUT reference torque

FIGURE 5.25: THOR, Efficiency Map

FIGURE 5.26: THOR, Shaft Power at two current level

FIGURE 5.27: THOR vehicle presented at Torino exposition

Chapter 6

Automatic Design

6.1   Automatic design of Synchronous reluctance motors (SyRE)

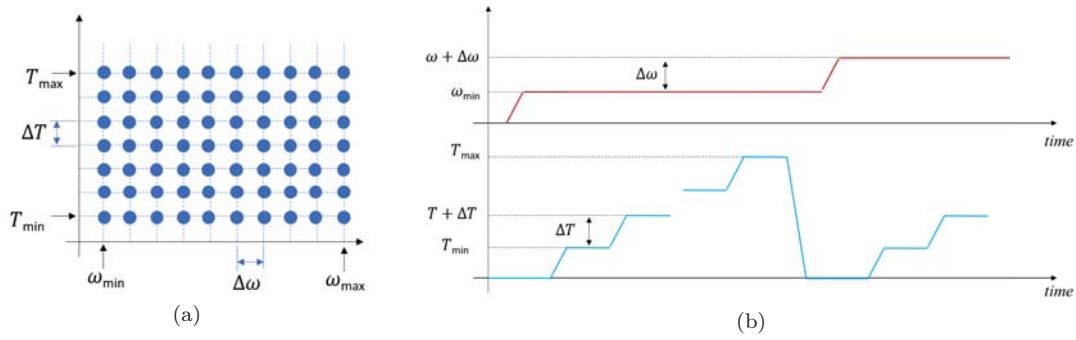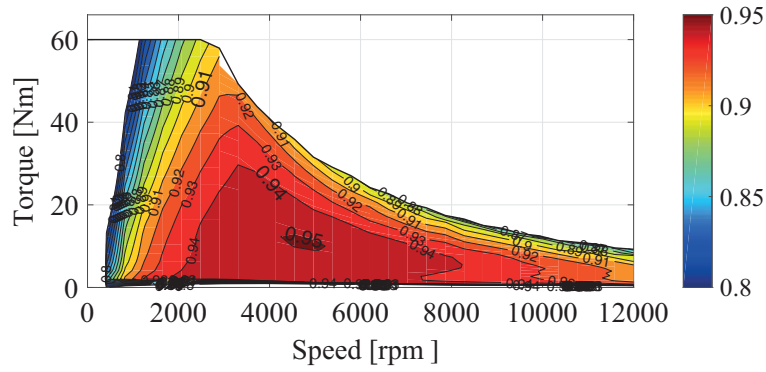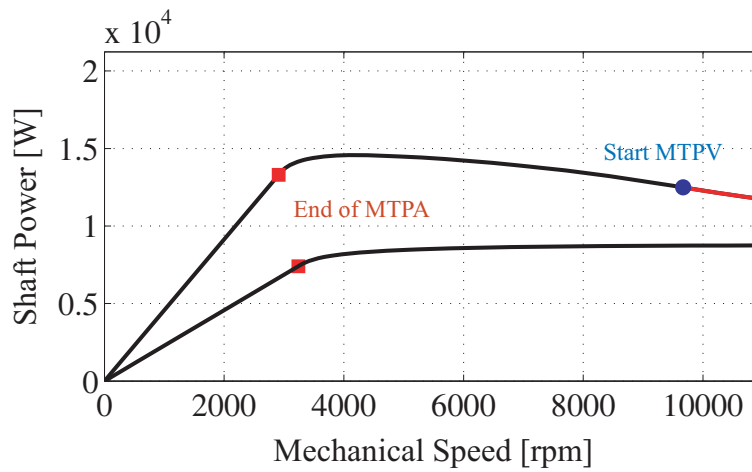In the last ten years the increment in the computation capability of Personal Computer, leads to a growing interest in the use of optimization algorithm, in the design of electromagnetic devices, [35]. This is related to the possibility of the exploration of multi-physics design trade-off and the optimization of non linear problems. The automatic design of such machines by means of optimization algorithms [36], [37] is discouraged by the mandatory use of finite element analysis (FEA) and to the peculiarity that more than one FEA simulation is needed for the evaluation of each new SyR machine. Both factors easily lead to long computational times. The use of FEA is mandatory because of the influence of magnetic saturation on machine performances [38]. Plus, torque ripple minimization is necessary [39],[40], and this requires FEA simulations in multiple rotor positions per each machine evaluation. Last, the current phase angle giving the Maximum Torque per Ampere (MTPA) is not known a priori for every new candidate machine. All considered, the number of FEA simulations required by multi-objective optimization turns out to be quite high. The former point is intended as the proper selection of the optimization goals, (torque per Joule loss and torque ripple) and of the geometric variables to be optimized. In the following it will be presented the construction rules for the simplified rotor geometry, described by few parameters per flux barrier, and the design procedure follows for the automatic design of synchronous reluctance motor.

The intent is to detail a procedure for the design of Synchronous reluctance machines that uses optimization algorithm, not to detail the optimization process topology.

6.1.1   General formulation of the motor design

The design procedure follows the flowchart shown in Fig 6.1. It is necessary at the beginning to define the outer stack surface (outer stator radius and stack length) like explained in Chapter 1. This permits to assume, disregarding the iron to copper conductivity variation that the machines analyzed, during the optimization process, present similar copper temperature. The K_j formulation is here reported (6.1). The K_j can be estimated by tabular value like ones in Tab.6.1 or defined according to the designer experience.

$$K_j = \frac{P_j}{stacks\,ylinder\,surface} = \frac{3/2\,R_s\,i_0^2}{2\pi\,R\,L} \tag{6.1}$$

$$R_s = 12\,\rho\,N_s^2\,\frac{L + L_{end}}{k_{cu}\,A_s} \tag{6.2}$$

Where R_s is the stator resistance, i_0 is the rated current estimated according to the thermal limit. In (6.2), N_s is the series turns per phase, ρ is the copper resistivity, k_{cu} slot fill factor, $L + L_{end}$ total turn length (stack+end winding). it is possible to evaluate i_0 from the geometry of the stator and the thermal limit K_j, substituting (6.2) in (6.1). In (6.2) k_{cu} is the net copper/slot area, A_s is the total slot surface, ρ is the copper resistivity function of the temperature.

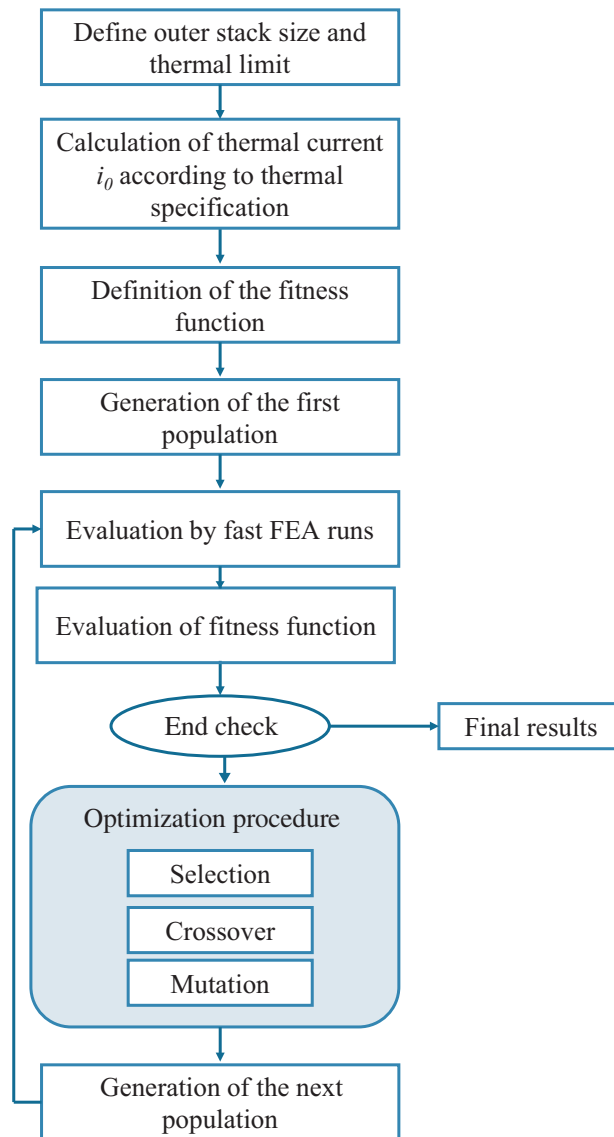$$i_0 = \frac{\pi\,R^{1,5}}{3\,N}\,\sqrt{\frac{k_{cu}\,K_j}{\rho}\,\frac{L}{L + L_{end}}}\,\sqrt{\frac{A_s}{\pi\,R^2}} \tag{6.3}$$

FIGURE 6.1: SyRE design flowchart

Parameter	value
totally enclosed	1,3-3 kW/m^2
forced ventilation	5-12 kW/m^2
liquid cooling	12-20 kW/m^2

TABLE 6.1: Typical K_j for different cooling system

The next step is represented by the definition of the fitness function, that usually is a linear combination of the objective functions. The objective functions represent the set of variables that must be maximized or minimized. For example typical variable in motor design are the maximization of torque, minimization of torque ripple, minimization of costs. In a general way it is possible to define the objective function $O(X)$ where $X = (x_1, x_2, ...x_n)$ represents the set of n design variables. In this specific case the geometric degrees of freedom in the stator and rotor design. The general formulation of the Fitness function is shown in (6.4). In this simple formulation $O_k(X)$ represents the performance to be optimized. The p_k variable represents a weight, that permits to add objectives that have different physical meaning and also to modulate the fitness function, in order to take into account objectives that have different absolute values. For example (6.5) represents a realistic fitness implementation that is used in the following. There are two typical design variables, torque and torque ripple. This two components can be really different from the numerical point of view. if ΔT is evaluated with the standard deviation it represents the distance from a mean distribution of points around the mean torque value and it can be some % of the mean torque. The $p_{\Delta T}$ variable can be used in order to increase the numeric value of ΔT and consequently "penalize" the fitness function in order to focus on the torque ripple optimization.

$$F = p_1 \, O_1(X) + p_2 \, O_2(X) = \sum_{k=1}^{m} p_k \, O_k(X) \qquad (6.4)$$

$$F = p_T \, T_{FEA} + p_{\Delta T} \, \Delta T_{FEA} \qquad (6.5)$$

The flowchart of Fig 6.1 shows a typical structure of the optimization algorithm. A population of N individuals is built. Each individual is characterized by a string composed by the number of degrees of freedom. All the individuals of the population are FE evaluated and the fitness of the population is calculated with (6.4). At this stage, the rules of the Genetic Algorithms (GAs) are applied to produce a new population. The process is repeated until are satisfied the exit rules. The GAs are the most up to date artificial intelligence techniques. Three steps are typically present:

- *Selection*: Individuals of the old population are selected and put in the new one, with preference given to the fittest. The selection can be stochastic sampling (by witch best and worst individuals are selected) or deterministic sampling (by witch only the best individuals are selected).

- *Crossover*: two randomly selected strings, among those selected in the previous step, are mated. A position along one strings is selected and swapped with those of the second string. Then the two new strings move in the new generation.

- *Mutation* a bit of string of the new population is randomly selected according to a defined probability and mutated.

6.2 Geometric rules for motors construction in SyRE

Stator and rotor constructions are parametrized according to few variables in order to simplify the optimization algorithm and the definition of the degrees of freedom. Only internal rotor motors are considered. The stator presents a typical construction related to the tooth width and length, slot opening etc. ... It will be shown more in detail in Chapter 6.2.2 that Rotor is the most critical component in SyR machine design. Different geometries are implemented. The various geometries differ for the flux barriers shape and degrees of freedom for each flux barrier. After the definition and the main strategy in the design of the various geometries, an analysis on the minimum number of degrees of freedom necessary to find a trade off between performances and computational time is carried on.

6.2.1   Stator and End Winding construction

The stator geometry is characterized by few parameters that permit to design the tooth width, the iron yoke indirectly evaluated by l_t, the slot opening etc. ... The stator can be a part of the optimization process or not. Some attention must be considered in the stator optimization, because the computational time increases and the only torque optimization leads to solutions that penalize too much the power factor. This is related to the adopted strategy in machine performance comparison, that impose a constant K_j.
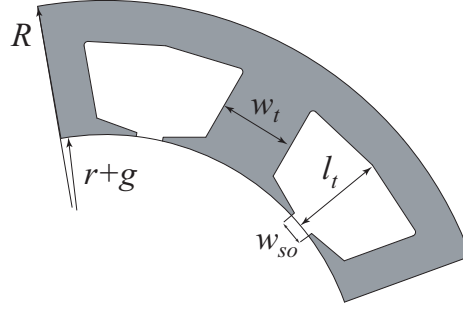
FIGURE 6.2: Stator main design variables

The end winding computation represents an important component in the stator resistance and Joule losses estimations. Two formulations are developed to take into account distributed and tooth windings configuration. In Fig 6.3 is shown the simplified hypothesis in the construction of end connection for distributed and tooth winding solutions.

(a)   (b)   (c)
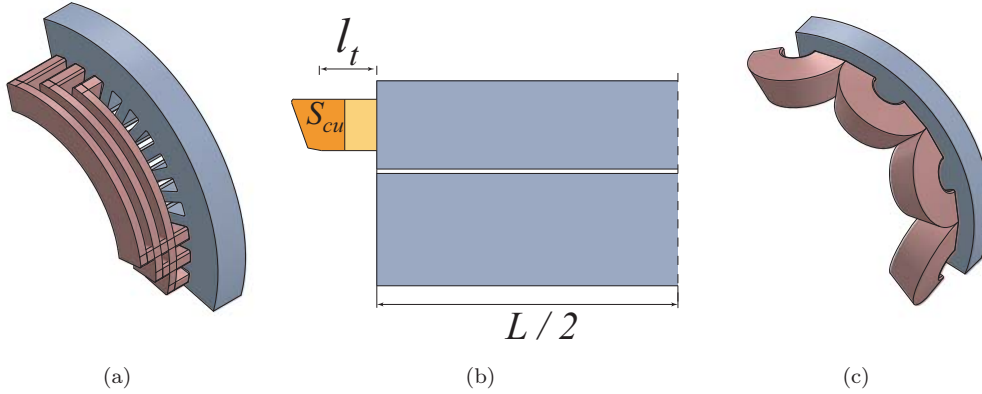
FIGURE 6.3: a) 3D view of the end winding connection according to (6.6); b) section of q=3; c) 3D view of q=1/2 end winding connection

The end winding formulation for distributed and mild overlapped solution is detailed in (6.6)

$$l_{end} = 2l_t + K_{sw} \left(r + \frac{l_t}{2} \right) \tau_p \tag{6.6}$$

Where l_t represents the tooth length, r is the airgap rotor radius, $\tau_p = \pi/p$ is the pole span and K_{sw} is the winding shortening factor.

A second formula (6.7) according to Fig 6.3c is used for concentrated winding:

$$l_{end} = \frac{1}{2} \left[w_t + \pi \left(r + \frac{l_t}{2} \right) \sin \left(\frac{\tau_{slot}}{2} \right) \right] \tag{6.7}$$

Where w_t represents the tooth width and τ_{slot} is the slot angle defined as $\tau_{slot} = \frac{\pi}{3pq}$.

6.2.2 Circular geometry

The circular geometry presents a cross section shown in Fig 6.4. The inputs in the design of this geometry are represented by the position of the flux barriers at the airgap $\Delta\alpha_k$ and the width $h_{c,k}$. This geometry is very simple to design and represents the base construction architecture for most of the others geometries developed in SyRE.
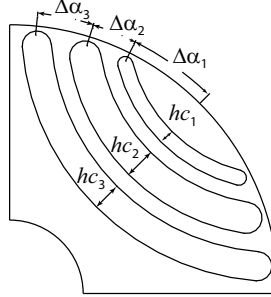
FIGURE 6.4: Circular geometry cross section

The procedure for the flux barriers construction is illustrated in Fig 6.5. Barriers are designed as circular segments, with center in $(x_0, 0)$. The x_0 point (6.8) depends on the number of poles, this permits a modulation of the curvature of the flux barriers varying the number of poles. The equations for the radius and angle of the central mean curve of the flux barrier by red dashed line in Fig 6.5a, are calculated with (6.9).

(a)   (b)
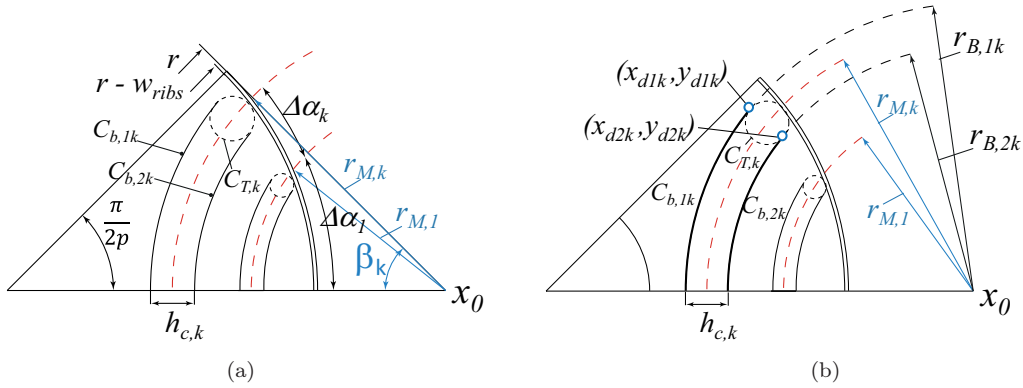
FIGURE 6.5: Circular geometry design rules

$$x_0 = \frac{r}{cos\left(\frac{\pi}{2\,p}\right)} \tag{6.8}$$

$$\beta_k = arctan\left(\frac{r\,sin(\alpha_k)}{x_0 - r\,cos(\alpha_k)}\right) \qquad r_{M,k} = \frac{x_0 - r\,cos(\alpha_k)}{cos(\beta_k)} \tag{6.9}$$

The radius of the arc of the circumferences, representative of the boundary of the flux barriers: $C_{b1,k}$, $C_{b2,k}$, are calculated with (6.10), the barrier width $h_{c,k}$ is split into two equal portion respect to the position of the barrier at the airgap.

$$r_{B1,k} = r_{M,k} + \frac{h_{c,k}}{2} \qquad r_{B2,k} = r_{M,k} - \frac{h_{c,k}}{2} \tag{6.10}$$

Finally the points $(x_{d1,k}, y_{d1,k})$ and $(x_{d2,k}, y_{d2,k})$ are calculated. These points represent the tangent between the circumference at the airgap $C_{T,k}$ and the boundary circumference $C_{b1,k}$ and $C_{b2,k}$, as shown in Fig 6.5a.

6.2.3   Segment geometry

This geometry presents three degrees of freedom per flux barrier. The inputs in the design process are represented by the position of the flux barrier at the airgap $\Delta\alpha_k$, the width of the barriers $h_{c,k}$, and the translation of the barriers along the q axis, Δx. The Circ-geo construction starts, as shown in Fig 6.6a, using as input $\Delta\alpha_k$ and $h_{c,k}$. With (6.8) and (6.9) are evaluated the position of the flux barriers at the airgap and along the q axis. The next step consists in evaluating with (6.11) the points $(x_{p,k}, y_{p,k})$, these points as illustrated in Fig 6.6b, represent the extreme points of the flux barriers near to the airgap, (the top of the flux barriers).

$$x_{p,k} = \frac{(r - w_{rib})^2 - r_{M,k}^2 + x_0^2}{2\,x_0^2} \qquad y_{p,k} = \sqrt{\frac{(r - w_{rib})^2\,\left(2\,x_0 - 1\right) + r_{M,k}^2 - x_0^2)}{2x_0}} \tag{6.11}$$
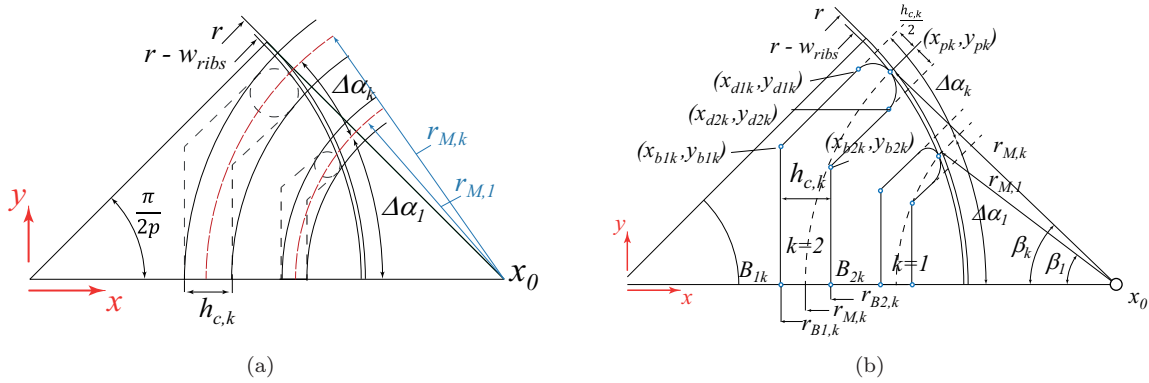
FIGURE 6.6: Segment geometry design rules; (a) Segment geometry construction
from Circular geo; (b) Main construction points

The lines $l_{b1,k}$ and $l_{b2,k}$ represent the upper border of the flux barriers. As reported in Fig 6.6a this lines are evaluated considering fixed distance from $(x_{p,k}, y_{p,k})$. The translation impact on the barrier design In Fig is evidenced 6.7. Considering this additional constraint is possible to express the $l_{b1,k}$ $l_{b2,k}$ line equation as reported in (6.12).

$$l_{b1,k} : \qquad y = tan\left(\frac{\pi}{2\,p}\right) x + \left(\frac{B}{2} - \sqrt{\frac{B^2}{4} - C1}\right) \tag{6.12}$$

Where

$$B = x_{p,k} - tan\left(\frac{\pi}{2\,p}\right) x_{p,k} \tag{6.13}$$

$$C1 = y_{p,k}^2 + tan^2\left(\frac{\pi}{2\,p}\right) x_{p,k}^2 - 2\,tan\left(\frac{\pi}{2\,p}\right) x_{p,k}\,y_{p,k} - \left(\frac{h_{c,k}}{2}\left(1 - \Delta x\right)\right)^2 \left(1 + tan^2\left(\frac{\pi}{2\,p}\right)\right) \tag{6.14}$$

The equations for $l_{b2,k}$ is equal to (6.12), the only difference is related to C1 that becomes C2 and is expressed in (6.15)

$$C2 = y_{p,k}^2 + tan^2\left(\frac{\pi}{2\,p}\right) x_{p,k}^2 - 2\,tan\left(\frac{\pi}{2\,p}\right) x_{p,k}\,y_{p,k} - \left(\frac{h_{c,k}}{2}\left(1 + \Delta x\right)\right)^2 \left(1 + tan^2\left(\frac{\pi}{2\,p}\right)\right) \tag{6.15}$$

$$r_{B1,k} = r_{M,k} + \frac{h_{c,k}}{2}\left(1 - \Delta x_k\right) \qquad r_{B2,k} = r_{M,k} - \frac{h_{c,k}}{2}\left(1 + \Delta x_k\right) \tag{6.16}$$

After the calculation of $l_{b1,k}$ and $l_{b2,k}$ it is possible to calculate points $(x_{b1,k}, y_{b1,k})$ and $(x_{b2,k}, y_{b2,k})$, that represents the corner point between the vertical and traversal lines of the flux barriers. This points are find substituting in (6.12) the coordinate $x = B_{1,k} = r - r_{M,k} - \frac{h_{c,k}}{2}(1 - \Delta x)$ and $x = B_{2,k} =$
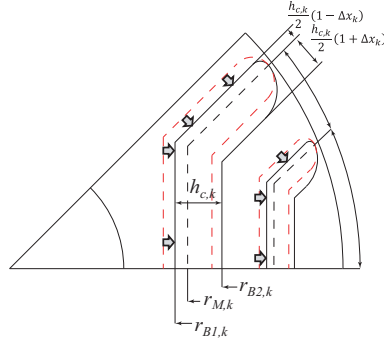
FIGURE 6.7: Segment geometry, example of the flux barriers translation

$r - r_{M,k} - \frac{h_{c,k}}{2}(1 + \Delta x)$. Finally $(x_{d1,k}, y_{d1,k})$ and $(x_{d2,k}, y_{d2,k})$ are calculated as the tangent points between the circumference at the airgap and respectively the $l_{b1,k}$ and $l_{b2,k}$ lines.

6.2.4 IxU geometry
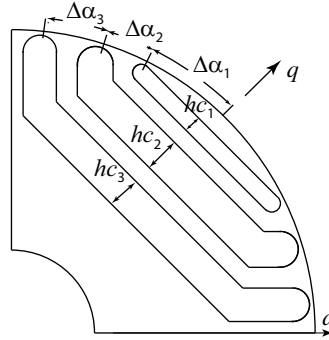
FIGURE 6.8: IxU geometry detail

This geometry can be considered a special case of the Segment geometry. Lower degrees of freedom respect to the Segment geometry are used. Flux barriers are symmetric respect to the central line, no horizontal translation, consequently the degrees of freedom are equal to the circular geometry. It presents better magnetic behavior than Circ-geo and better mechanical strength. This is related to the fact that as shown in Fig 6.8, flux barriers do not go inside the rotor like in Circ-geo, the volume of the flux guides (the iron segments between the flux barriers) is lower and consequently also the centrifugal stress is reduced respect to the Circ-geo. The construction rules comes from the segment geometry setting $\Delta x = 0$ the horizontal translation is not used in this geometry. In the construction process the iron width of the flux guide is the same as for the Circ-geo, see Fig 6.9b. The position of the center of the circumference at the airgap, $C_{T,k}$, represented by points $(c_{c,k}, y_{c,k})$ is evaluated using (6.17).

$$x_{p,k} = \frac{(r - w_{rib} - h_{c,k}/2)^2 - r_{M,k}^2 + x_0^2}{2\,x_0^2} \qquad y_{p,k} = \sqrt{\frac{(r - w_{rib} - h_{c,k}/2)^2\,(2\,x_0 - 1) + r_{M,k}^2 - x_0^2)}{2x_0}}$$

(6.17)

It is evident from Fig 6.9 that the first flux barrier is designed with the center of the barrier along the coordinate $x_{c,1}$ than the two border of the barrier B_{11} and B_{21} are equally spaced around the central point, $B_{11} = x_{c,1} - h_{c1}/2$ and $B_{21} = x_{c,1} + h_{c1}/2$. Passing to the internal flux barrier, the related position is obtained maintaining the same width of the iron guide of the equivalent circular geometry (6.18).

$$B_{1,k} = B_{1,k-1} - h_{fe,k-1} - h_{c,k} \qquad B_{2,k} = B_{1,k-1} - h_{fe,k-1}$$

(6.18)
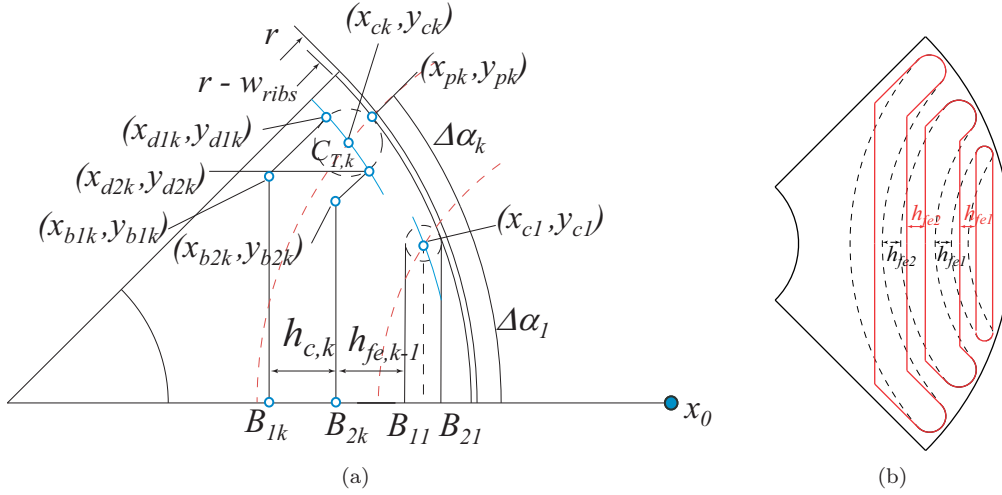
FIGURE 6.9: (a) IxU design rules; (b) Comparison between circular and IxU geometry

6.2.5   Fluid geometry
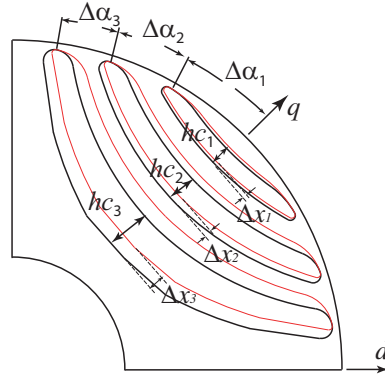
FIGURE 6.10: Fluid Geometry cross section

The profile of the new barriers, Fig.6.10 is inspired to the field lines in a virtual solid rotor, represented in Fig.6.11. This solution was originally used and explained by Reza [41]. A closed-form expression of such field lines can be derived from the conformal mapping theory and the Joukowski air-flow potential formulation. This was originally developed to describe the fluid flow paths channeled by two infinite plates forming an angle π/p and with a plug centered into the origin of the reference frame. In the solid rotor context, the plug represents the nonmagnetic shaft. The equation expressing the magnetic field potential lines of Fig 6.11 is.

$$C = sin(p\theta)\frac{\left(r/a\right)^{2p} - 1}{\left(r/a\right)^{p}} \tag{6.19}$$

where r and θ (radius and polar angle) are the polar coordinates of each point of the plane, p is the number of pole pairs of the machine, a is the shaft radius and C defines which field line is considered: the lower is C, the closer the field line is to the shaft. So each field can be selected with continuity by the proper selection of C. For instance, to pick up the field line that intercepts the airgap at the angular coordinate α_k defined in Fig 6.11a, the value C_k is determined by substitution of the coordinates of point $E_k(r_k, \theta_k)$ in (6.19), where E stands for the end-point of the barrier. Once C_k is known, the explicit equation of the field line, in polar coordinates is:

$$r(\theta, C) = a\left(\frac{C + \sqrt{C^2 + 4sin^2(p\theta)}}{2sin(p\theta)}\right)^{1/p} \tag{6.20}$$
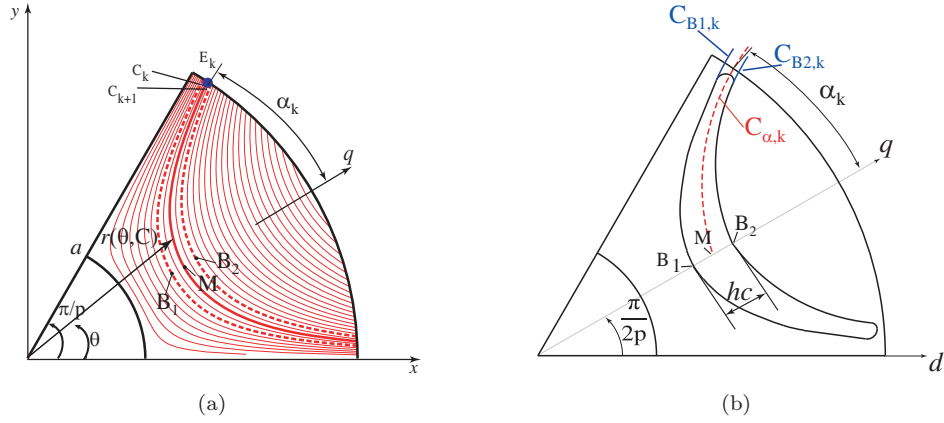
FIGURE 6.11: (a) Fluid geometry flux lines; (b) Fluid geometry main design rules

The MODE algorithm selects three parameters that define the k-th barrier (k = 1 to n_{lay}): the end angular position α_k, the height of the barrier cavity h_{ck} and the new parameter Δx_k, that is the offset of the cavity with respect to the α_k-defined center line. At first, the α_k–driven line is traced with the procedure described in the previous subsection. The value of C_k is obtained via (6.19); then the radial coordinate r_M of the mid-point M defined in Fig 6.11b is determined by substitution of C_k and $\theta = \pi/2p$ into (6.20). From M, the mid-points of the inner and the outer bounds B_1 and B_2 are determined.

$$\begin{cases} r_{B1,k} = r_{M,k} - \frac{h_{c,k}}{2}\left(1 - \Delta x_k\right) \\ r_{B2,k} = r_{M,k} + \frac{h_{c,k}}{2}\left(1 + \Delta x_k\right) \end{cases} \tag{6.21}$$

The positions of B_1 and B_2 depend on the two parameters h_{ck} and Δx_k, where the per-unit offset factor Δx_k varies in the range [-1, 1]. The inner and outer profiles of the k-th barrier are the field lines passing by B_1 and B_2. The substitution of the coordinates of B1 and B2 into (6.19) and the application of (6.20) permits to trace the flux barrier sides. The procedure is graphically summarized in Fig.6.11. From the analysis of (6.21) and (6.21) it comes out that the barrier is h_{ck} thick along the q-axis, and offset radial-wise outwards or inwards by $\Delta x_k, h_{ck}$, with respect to the virtual midline defined by the barrier-end position α_k. For example, with $\Delta x_k = 1$ the barrier is all outwards (B1 = M); vice-versa with $\Delta x_k = -1$ ($B_2 = M$). If $\Delta x_k = 0$ the barrier is 50-50 split around the nominal midline. The tangential ribs connecting the flux guides at the air-gap are traced using two circular segments tangent to the barrier side lines and to the rotor external circumference. Their thickness is minimized off-line, according to mechanical constraints (centrifugal stress) and steel cut tolerances.

6.3 Optimal number of rotor parameters for the Automatic Design of Synchronous Reluctance Motor

When multi-barrier rotors are considered, the input data of the different barriers must be coordinated to avoid that some combinations of the inputs lead to overlapping barriers and unfeasible rotors. At this purpose, the angles and thicknesses are expressed in normalized quantities, so that their respective sums do not exceed the available angular span ($\pi/2p$) and the available space along the q-axis, respectively. The base values of the p.u. angles and heights are the total angle of height available for all the layers. The p.u. thicknesses $h_{c1,2,3}$ are interpreted as follows: if they are all 1 p.u. then the air barriers are all thick the same and occupy as much radial space as they can. The upper limit to the barriers space occupation is a minimum steel thickness of 1 mm radial-wise that is guaranteed between two adjacent barriers, to ensure that the rotors are feasible manufacturing wise. A width of 0.4 mm is used for the tangential structural ribs, connecting the flux-guides at the barriers ends. All the designed machines have been verified towards centrifugal stress via structural FEA, at the maximum speed of 8000 rpm, after the optimization. The barrier offsets $\Delta x_{1,2,3}$ introduced before can vary between -1 and 1. The limits of the search space are summarized in 6.2.

TABLE 6.2: Steady State Operation of the two Prototypes

Parameter	Min value	Max value	Units
$h_{c,k} k = 1 \quad to \quad n_{lay}$	0.2	1	p.u.
Δx_k	-1	1	p.u.
$\Delta \alpha_k$	0.33	0.67	p.u.
γ	20	80	degrees

The main parameters and target ratings of the machine example are reported in Tab.6.3. Multi-Objective Differential Evolution (MODE) and FEA are used in the following to design SyR rotors giving maximum torque and minimum torque ripple. The MODE algorithm was chosen after the comparative analysis of [11], where it showed to lead to the same rotor designs of other multi-objective optimization algorithms, but with a number of FEA calls which is consistently lower.

TABLE 6.3: Main Parameters of the Prototypes

Quantity	Value
Stator slots	24
Pole pairs	2
Rotor diameter	58.58 mm
Stator diameter	101 mm
Stack length	65 mm
Airgap	0.5 mm
Rated current	14.29 A
Rated voltage (dc link)	300V
Maximum speed	5000rpm

A single current vector in dq synchronous coordinates is simulated for each candidate machine, with the output torque evaluated in five rotor position over one stator slot pitch. The current amplitude level used in the optimization is more than twice the continuous operation current. Preliminary investigations showed that the use of the overload conditions during the optimization guarantees the torque ripple minimization also at lower loads, and not vice-versa. The current phase angle γ (phase angle of the current vector respect to the d axis) should possibly be the one giving the maximum torque per Ampere (MTPA) condition, γ_{MTPA}, because this would maximizes also the torque per Joule loss and then, in a way, the efficiency. The phase angle γ is directly optimized by the MODE at once with the torque maximization.

The potential of the higher degrees of freedom represented by the Fluid geometry was investigated via several MODE runs stopped at progressive numbers of iterations, to establish a relationship between the output performance and the computational time. A first set of 10 runs was stopped after 1200 function calls (1200 candidate machines evaluated). Other 10 runs were stopped at 3000 calls and, finally, a last set of 10 runs was stopped at 10000 evaluations. In Fig 6.12 the three groups of ten Pareto fronts are summarized and directly compared with the ones obtained with the same MODE procedure and the simpler I2U geometry of Fig 6.4. Such geometry is representative of the two degrees of freedom per flux barrier case.

The Pareto fronts in Fig 6.12a and Fig 6.12b put in evidence that after 1200 calls and also after 3000 calls the performance of the two geometries is still comparable. The aggregate of ten fronts of one geometry is fairly superimposed to the 10 fronts of the other geometry. In both figures, there are two mild but consistent trends: 1) the I2U rotors tend to have solutions with very lower ripple values, 2) the fluid barrier rotors tend to have solutions with higher torque values. At 10000 calls, in Fig 6.12c, the new fluid geometry has a clear advantage in terms of average torque, and the performance of the I2U solutions did not improve respect to the situation at 3000 calls. In other words, the further calls from 3000 to 10000 (Fig 6.12b,c, blue markers) are unnecessary for the I2U rotors. In turn:

- The $2 \, x \, n_{lay}$ parameters geometry (I2U) converges to its maximum performance in a shorter time.

- Coherently, the $3 \, x \, n_{lay}$ parameters geometry (fluid barriers) can give a better performance, at the expense of a longer computational time.

- Comfortably enough, the performance obtainable with the new geometry and quick runs (1200 and 3000 calls) is not worse than the one obtained before.
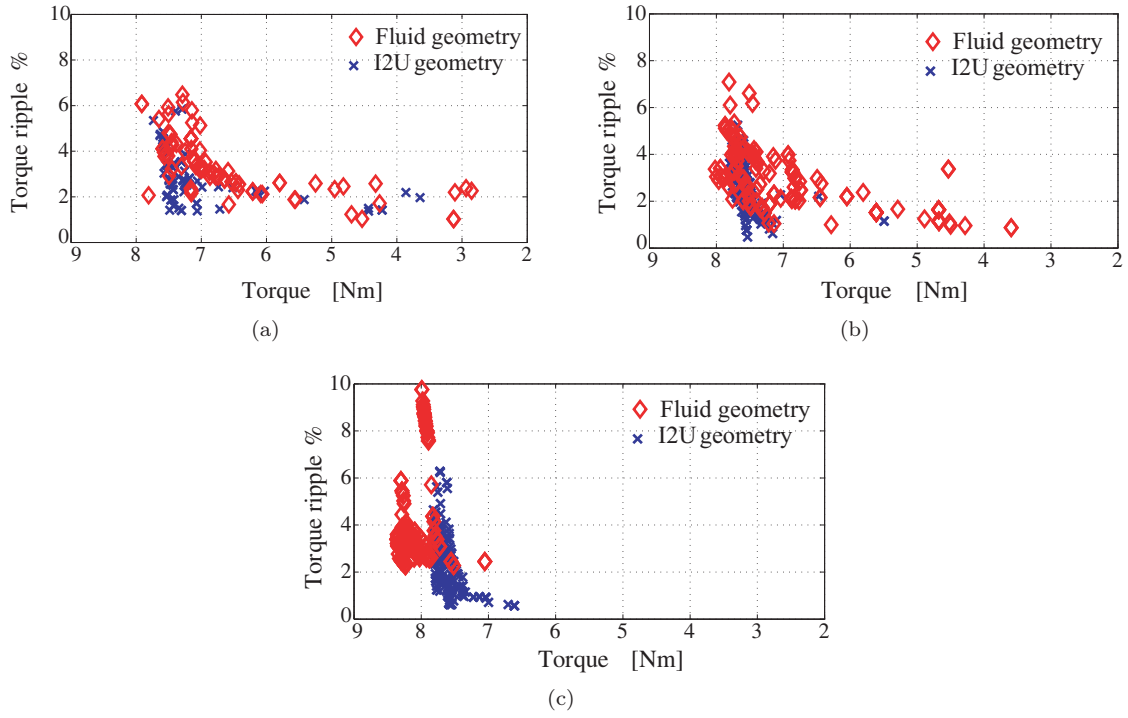
FIGURE 6.12: Summary of the Pareto fronts of 10 MODE runs for the fluid geometry (red) and the I2U geometry (blue). a) Stop after 1200 calls; b) 3000calls; c) 10000 calls

6.3.1 Non-Dominated Solution

The non-dominated solutions taken from the sets of Pareto fronts of Fig.6.12 are considered in this section and summarized in Fig.6.13. One solution to a multi-objective optimization problem is defined non-dominated when there is no other solution performing better in both (or all, for n-objectives) the cost functions. Each set of 10 MODE runs is considered time by time as a whole to produce a front of non-dominated solutions representative of those 10 runs. Fig.6.13a for example, the non-dominated solutions of the 10 runs stopped at 1200 calls are represented along with the non-dominated fronts stopped at 3000 and 10000 calls. This for the fluid barrier rotors. In Fig.6.13b the same is done for the I2U rotor geometry. The evolution of the non-dominated fronts in Fig.6.13 confirms the conclusions of the previous subsection, in a form that is easier to visualize:

- 3000 calls are enough for the I2U geometry but not for the fluid barriers;

- with enough computational time, the fluid barriers can give more torque.

Returning to the analysis of the aggregated Pareto front estimates, they evidence a not-perfect repeatability of the final result. In particular for the earlier stops, the number of calls is insufficient for full convergence. Second, there is noise in the evaluation of the cost functions, so some solutions are found by coincidence and not repeated on the other fronts. Third, stochastic algorithms are always at risk of a false convergence, i.e. of converging to local minimum, so one or more fronts out of ten can be non-optimal.

6.3.2 Results discussion

Two optimal designs, one per geometry, are extracted from the Pareto fronts to be prototyped and compared. The criterion for selecting one solution from the MODE results is to set a maximum target ripple value of 2% and choose from the Pareto fronts accordingly, with some flexibility. For example: for the fluid barrier case the 3000 calls front in Fig 6.13a would produce a solution with 7.8 Nm and 2% ripple, whereas the 10000 calls front of non-dominated solutions would give no solution within the 2% ripple. Nevertheless, the machine of the front which is closer to 2% ripple has a torque of 8.2
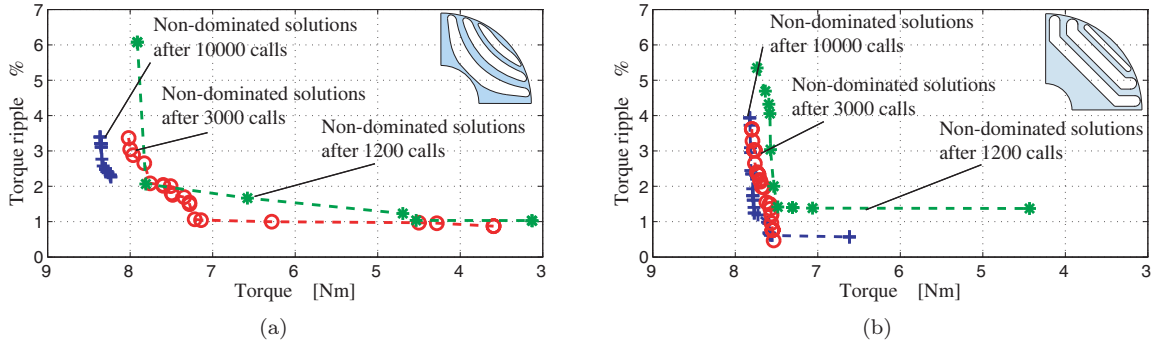
FIGURE 6.13: Envelope of non-dominated solutions of the 10 Pareto front groups of
Fig. 4 for the two geometries: a) fluid barriers, b) I2U.

Nm and it is than selected as final design of the fluid barrier case. So the final design is expected to give 8.2 Nm and 2.2% ripple at maximum current. About the I2U rotor solutions, the selection of the exact 2% ripple machine would produce 7.7 Nm after 3000 calls and 7.8 Nm after the 10000 calls. However, the front of the 10000 call solutions in Fig 6.13b includes many solutions with a lower ripple and nearly the same torque. So a very promising machine advocated of 7.8 Nm and 1.2% ripple by the FEA was selected for being prototyped. The cross sections of the final designs, selected from the MODE results in Fig.6.13, are represented in Fig 6.14. The blue circles indicate the positions of the barrier ends at the airgap. It is evident in both cases that the MODE found that the torque ripple is minimized by means of equally spaced equivalent rotor "slots".
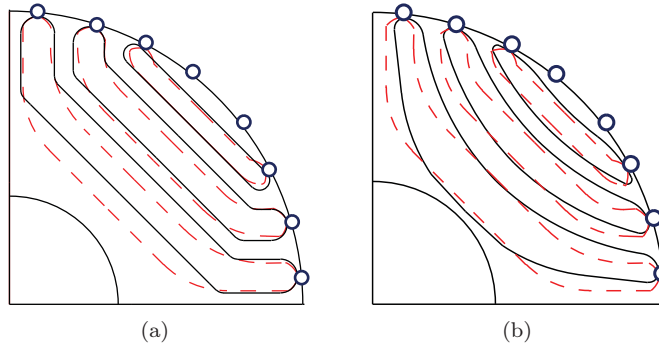
FIGURE 6.14: Final MODE designs (black continuous lines) superimposed to the
state of the art (SOA) rotor pole (red dashed lines). a) I2U, b) fluid.

The red dashed traces superimposed to the MODE designed cross sections are representative of the State of the Art (SOA) rotor prototype used for comparison in the following, designed according to the principles of [42]. Besides the same rotor slot positions, common to all three rotors, the fluid geometry (Fig 6.14b) shows a good agreement with the SOA also in terms of the distribution of the flux barrier and flux channel thicknesses along the q-axis. The flux density maps, FEA evaluated at rated current conditions, are reported in Fig. 6.15 for the three machines under comparison: the fluid and the I2U automatic designs and the SOA design. It is evident that the same current loading produces different grades of saturation in the rotor, for the three. The machines with more degrees of freedom (Figs.6.15b and 6.15c) see their flux guides being less loaded. This thanks to the possibility of optimizing the thickness of the flux guides separately from the thickness of the flux barriers. The I2U geometry has no possibility in this sense, and its flux guides are more loaded already at continuous current (while the optimization was run at overload current). The earlier saturation justifies the lower output torque obtained with the I2U rotor, a problem that is overcome with the fluid barriers.

FIGURE 6.15: Flux density maps for the three motors under analysis, at continuous current and MTPA conditions. a) I2U; (b) Fluid barrier; (c) SOA.

6.4 Experimental Results

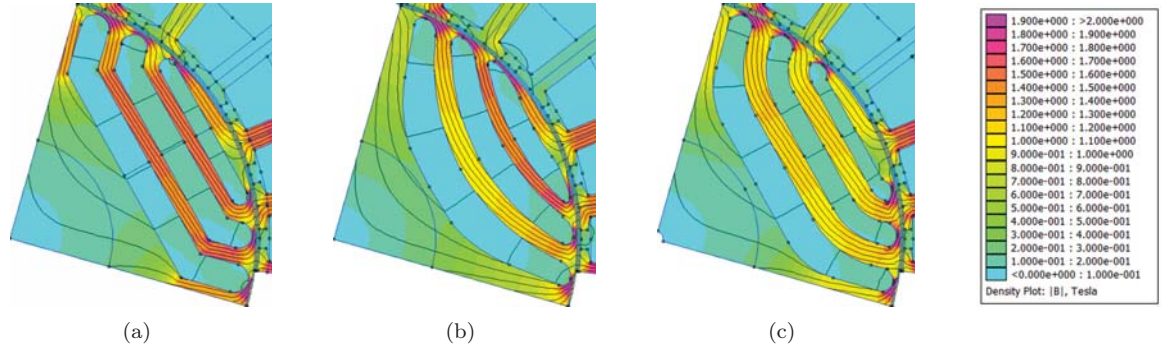Three rotor prototypes were realized, wire-cut, and accommodated on three identical shafts to be replaced into a common stator. The pictures of the laminations are reported in Fig.6.16.
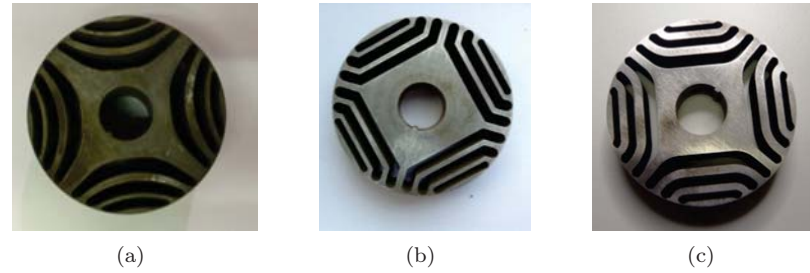

FIGURE 6.16: Rotor laminations. a) Fluid barriers; b) I2U; c) SOA.

A dedicated test bench was used to measure the torque waveforms of the prototypes in many different i_d, i_q current combinations. A speed-controlled DC motor having very low torque ripple drives the motor under test via a reduction gearbox. The speed is set to 10 rpm. The torque is measured via a high precision torque meter. The motor under test is vector-controlled, using a dSPACE 1104 R&D controller board. The i_d, i_q reference sequence and the acquisition of the torque signal during one motor revolution are automatically handled by means of a Matlab script using the commands of the MLIB/MTRACE dSPACE library (https://www.dspace.com/en/inc/home.cfm) for dSPACE experiments automation. The torque-meter rating imposes to stay under 10 Nm which corresponds to an area of operation of 20 A per 30 A in the i_d, i_q plane. The test setup is depicted in Fig 6.17.

At first, the average torque performance is considered. The measured torque values are represented for the three prototypes as a function of the current phase angle in Fig.6.17. Three current amplitudes are represented, corresponding to 44%, 117% and 227% of the continuous current amplitude. Phase angle zero means that the current vector is aligned to the d-axis, whereas phase angle 90° corresponds to the q-axis. The 32.5 A condition is also the one used by the MODE for producing the automated designs. In Fig 6.18, the three torque curves at low current are identical. As the current grows, the "fluid" machine has a progressive advantage over the SOA prototype, which has an advantage over the I2U prototype. This confirms that the latter machine is the one suffering more from progressive steel saturation. The torque improvement from the $2xn_{lay}$ parameters geometry (I2U) to the $3xn_{lay}$ parameters fluid geometry is confirmed by the experiments. Plus, the new geometry can have more torque that a standard design. It is important to remark that the SOA machine was not specifically optimized for maximum torque, and also that a human design cannot explore all the space of the design parameters to find the exact maximums of all the design goals. So to say that the better torque obtained with the fluid barrier geometry here indicates that the torque obtainable with three parameters per flux barrier is comparable to the one obtainable with no restrictions to the rotor barriers description. The MODE-designed machine then has a higher torque thanks to the application of the
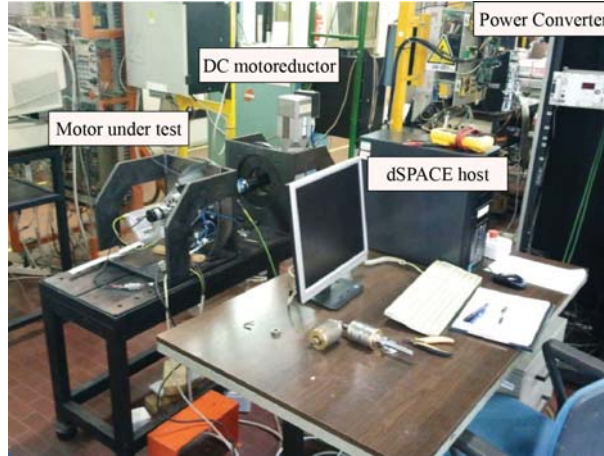
FIGURE 6.17: Test bench used for the identification of the prototypes.

optimization algorithm. In conclusion, the proposed approach defines a description of the SyR rotor geometry that is arguably the simplest form of obtaining the maximum possible torque performance.
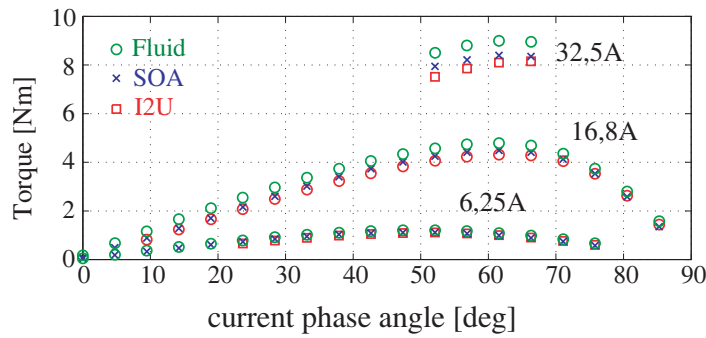
FIGURE 6.18: Comparison of the measured average torque as a function of the current phase angle at current amplitudes 6.5 A (44%), 16.8 A (117%) and 32.5 A (227%).

6.4.1   Torque Ripple Comparison

The measured and FEA calculated torque waveforms are reported in Fig.6.19 for the three machines. One electrical period (half mechanical revolution) is represented. The same three current levels used in the previous figures are used here, in the respective MTPA conditions. The FEA and measured values are directly compared. The experiments confirm that the torque ripple of the fluid barrier is fairly minimized and lower than the one of the SOA design (Fig.6.19). This again is due to the application of the optimization algorithm. This work demonstrates that an automatic designed SyR rotor described with three geometric parameters per flux barrier can perform better than a human-designed prototype, which has no limits to the degrees of freedom for the description of its rotor geometry. The proposed fluid-barrier geometry improves the results obtained in the previous works dedicated to the automatic design of SyR machines and will be the pivot of a fully automated, time competitive design procedure for this class of synchronous machines, to the benefit of the industrial world.

6.4.2   Effect of Steel Cutting Process

The steel cutting process can have key implications on the performance of SyR motor prototypes. For mass production, punch cutting is used, whereas for prototypes laser cutting is much more flexible and convenient. However, it is well known that the local heating produced by the laser in the cut area damages a portion of material, with negative effects on the B-H properties of the final lamination. An

(a)

(b)

(c)

FIGURE 6.19: Torque waveforms at 6.5 A (48%), 16.8 A (123%) and 32.5 A (239%) on the MTPA, FEA (blue line), EXP (black line), a)Prototype I2U, b) Fluid, c) SOA
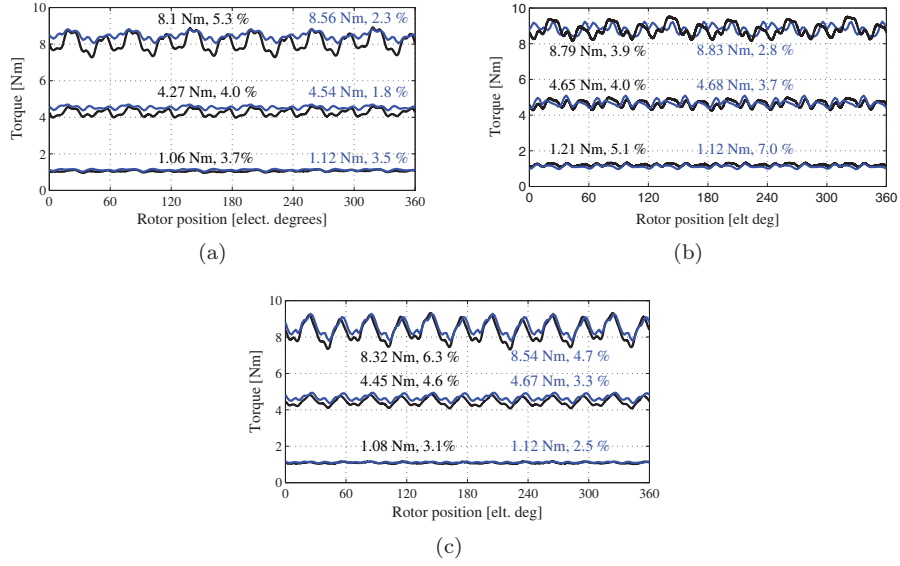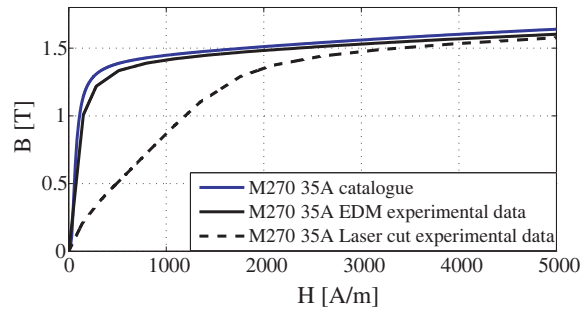

(a)

(b)

FIGURE 6.20: B-H characteristic of non-oriented steel grade M270-35A: blue) datasheet, black continuous) EDM cut sample, black dashed) Laser cut sample

high-quality alternative to laser cutting is Electro Discharge Machining (EDM), that has no side effect but way less available than laser. All prototypes tested so far are EDM cut, for the sake of consistency with the ideal steel used in FEA based design. However, real life prototypes often have to deal with laser cut. Therefore, a second Fluid rotor prototype has been fabricated, this time with laser cut laminations, to give evidence of the effects of cutting. Moreover, two samples of the same laminations (grade M270-35A) have been realized, one laser cut and one EDM cut, to measure the respective B-H curves. Fig 6.20a, reports the results of the B-H measurement and one of the sample toroids. It is clear that the laser cut deteriorates the permeability of the steel in the non-saturated area, whereas EMD cut is harmless. The laser cut prototype is compared to the EDM cut one, in terms of measured torque waveforms. The results are reported in Fig 6.21a. Progressively with current load, the laser cut rotor gives less torque than the EDM cut competitor does. It is a limited effect (-4% at overload), but it stands for the detrimental effect of cutting on the B-H characteristic. Moreover, torque ripple is slightly different, too. It is therefore quite risky to run an automatic design session without taking into account the actual B-H curve of the laminations. The results of FEA optimization and prototypes could be disappointingly far from each other. The Fluid machine is FEA simulated a second time, this time using the experimental B-H curve measured on the laser cut sample, reported in Fig 6.21b. As for other cases, in overload conditions the match of calculated and measured curves is less satisfactory than at lower loads.
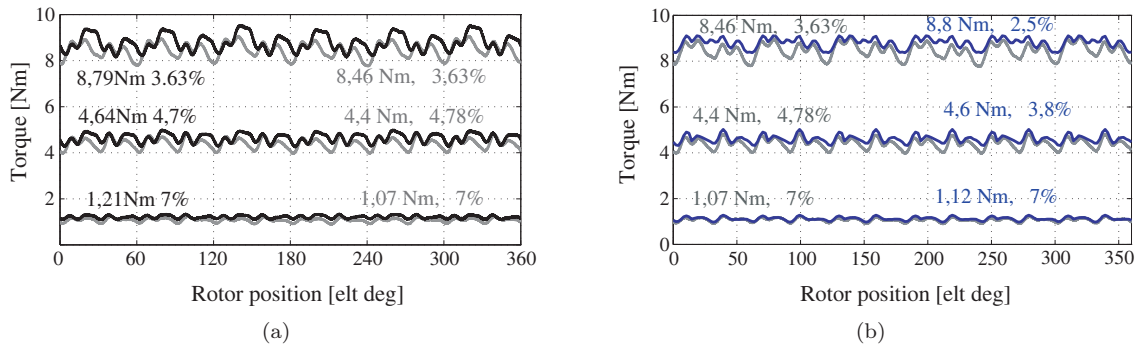
FIGURE 6.21: a) Fluid prototypes: experimental comparison between EDM cut (black) and laser cut (grey); b) Fluid prototypes: FEA (blue, like in Fig 6.19) versus laser cut (grey lines).

6.5   Simplified Thermal Model

Based on [43] and [44]. It is implemented a simplified thermal network suitable for the estimation of the over-temperature respect to the frame temperature. In [45] are summarized many problems in the estimation of the correct heat flow in electrical machine. Really problematic are the convention coefficients and the heat flow in the slot. The developed model is not intended to be used for a careful temperature estimation in the various part of the machine, but for obtaining a quantitative estimation of the over-temperature respect to the frame temperature. This in the preliminary design procedure can help the designer also in the correct choice of the pole and slot combination. In fact when passing from a distributed winding machine to a concentrated one, heat flow in the slot is affected by higher radial length (slots are bigger than in a distributed winding, see Fig.6.22) and the inner slot surface is lower. All this conditions leads to higher copper temperature. The estimation of this temperature variation, between different windings configuration, is used in the next Chapters for choosing the number of poles that in combination with the efficiency reduce the discrepancy between FSW-SyR and distributed winding SyR motors. The model compute the over-temperature in steady state condition for this reason thermal capacities are neglected. The following hypothesis have been assumed:

- Only stator joule losses are considered.

- Only radial heat transfer is considered, no 3D effects are taken into account. End winding connections are considered in Joule losses computation.

- heat exchange through the axial dimensions is neglected, only radial heat flow is considered.

- Frame temperature is assumed constant and imposed as a parameter.

The steps of the network simplification are shown in Fig. 6.22. Assuming that the electromagnetic phenomena are faster than the thermal ones is possible to assume that the Joule losses are equally distributed in the stator slots. The first simplification as shown in Fig.6.22a,b leads that all the joule losses flow in one direction, for symmetric reason. The next simplification is model all the machine by one equivalent slot tooth and yoke, see Fig.6.23a. Looking in Fig.6.22b points t_1, u_s,u_t present the same potential for all the slots. This is related to the fact that all slots presents the same geometry and the thermal power generators are the same for all the slots, than all the slots are in parallel. The model of the slot presents very simple division into two portions. This division, especially in the case of fractional slot machines, where the slot is bigger compared to DW, permits to have a more accurate estimation of the temperature variation between frame and slots. The slot is supposed divided into two portions, with an inner area $A_{cu,1}$, and an outer area $A_{cu,2}$. The power production is divided according to the area.

(a)

(b)
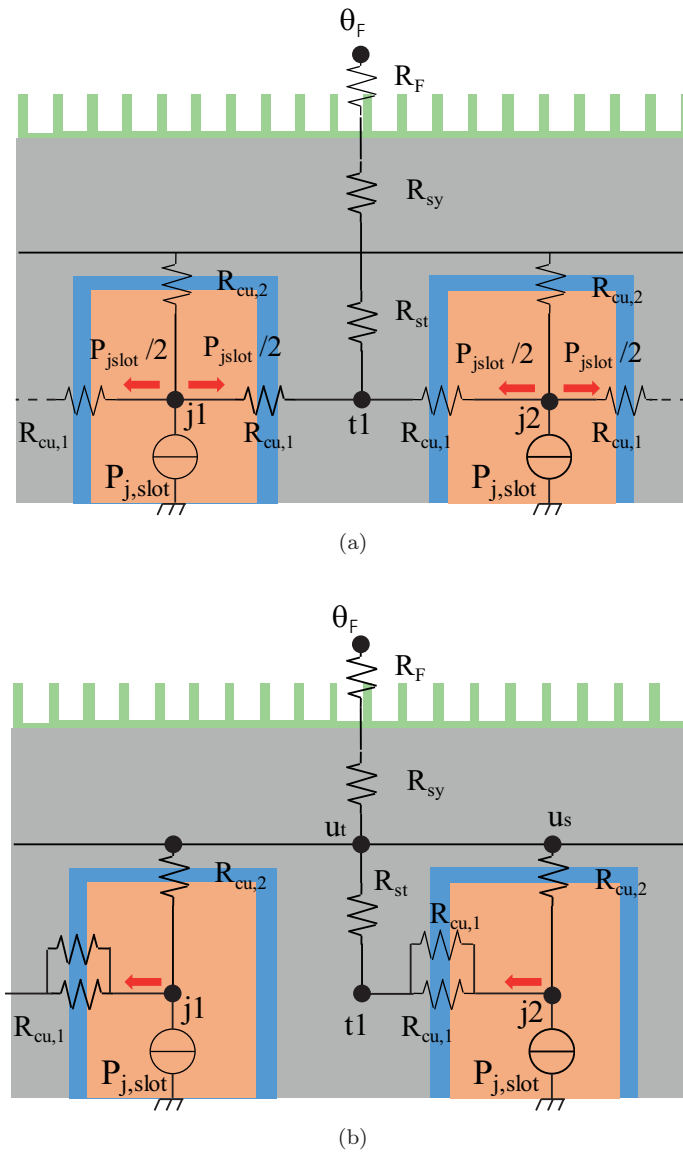
FIGURE 6.22: a)Slots Thermal network, b) One side radial thermal flow
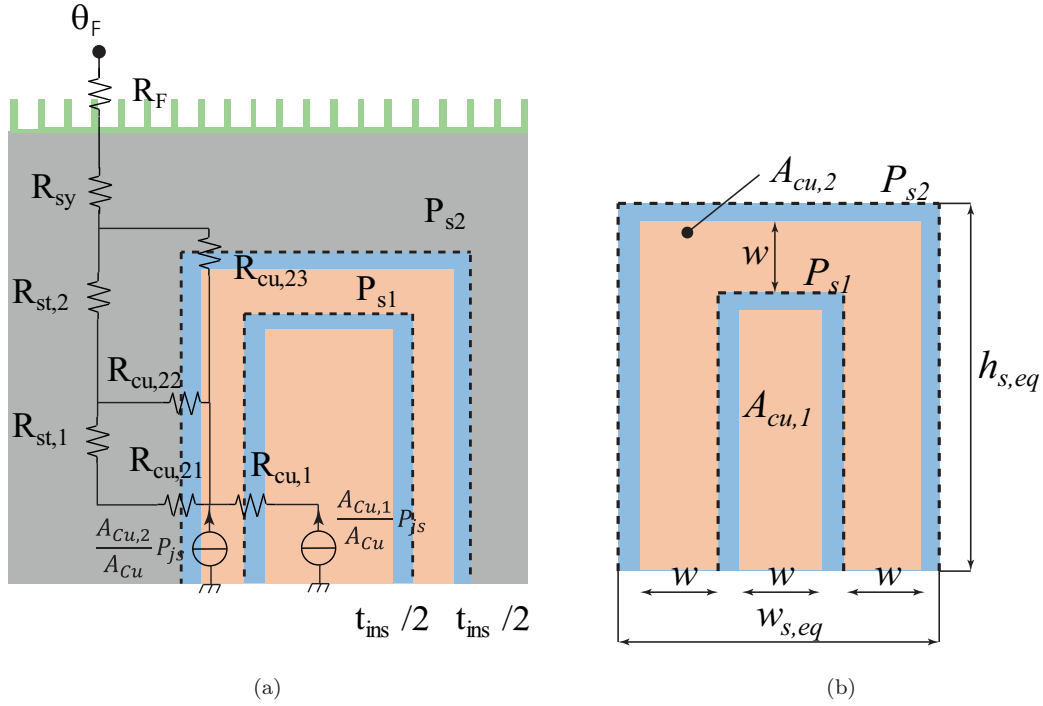
FIGURE 6.23: a)Thermal network, b) zoom of slot subdivision

Stator yoke thermal resistance can be expressed by (6.22):

$$R_{sy} = \frac{1}{2\,\pi\,\lambda_{fe}\,L}\left(\frac{R}{r+g+l_t}\right) \tag{6.22}$$

The tooth resistance is divided into two components, one, $R_{st,1}$, representing temperature drop at the middle of the tooth, and $R_{st,2}$, representing the drop between the middle and the end of the tooth.

$$R_{st,1} = \frac{1}{2\,\pi\,\lambda_{fe}\,k_{pth}\,L}\left(\frac{r+g+l_t/2}{r+g}\right) \qquad R_{st,2} = \frac{1}{2\,\pi\,\lambda_{fe}\,k_{pth}\,L}\left(\frac{R}{r+g+l_t/2}\right) \tag{6.23}$$

Where λ_{fe} is the iron thermal coefficient generally equal to $25\mathrm{W}/(\mathrm{m\,K})$, r is the rotor external radius, L is the stack length, g is the airgap length, l_t is the tooth length ; k_{pth} represents the ratio between the iron volume and total volume (iron+slot) without the yoke (6.24).

$$K_{pth} = \frac{iron\ teeth\ volume}{total\ stator\ volume} = \frac{6pq\,w_t\,l_t}{6pq\left(w_t\,l_t + A_{slot}\right)} \tag{6.24}$$
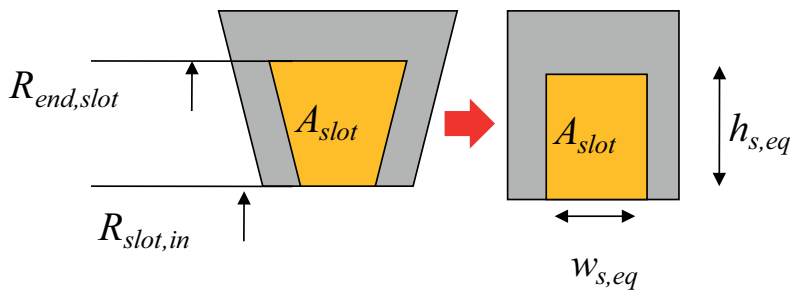
FIGURE 6.24: slot equivalent rectangular size

The slot is modeled according to the simplification introduced in Fig.6.24. The slot area is respected and the size of the slot is changed with an equivalent rectangular area. The slot length is calculated according to (6.25).

$$w = \frac{w_{s,eq} - 2\,t_{ins}}{3} \tag{6.25}$$

Where t_{ins} is the insulation thickness present in the slot. In the real machine this air quantity is quite uniformly distributed over the slot area. In the model it is assumed that this air represents a thin layer on the border on the two slices of the slot. in (6.26) it is shown how to evaluate this thin layer.

$$t_{ins} = \frac{(1 - k_{cu})\,A_{slot}}{P_s} \tag{6.26}$$

Where A_{slot} is the stator slot surface, P_s is the external slot perimeters, see Fig 6.22 . The insulation thickness is divided into two portions with equal thickness $t_{ins,1} = t_{ins,2} = t_{ins}/2$.

Than the inner perimeter P_{s1} and the slot area are calculated with (6.27)

$$P_{s1} = 2\big(h_{s,eq} - t_{ins}/2 - w\big) + w + t_{ins} \qquad A_{s1} = w\big(h_{s,eq} - t_{ins} - w\big) \tag{6.27}$$

With the geometric constraint previously defined. The slot resistance for the inner slice is shown in (6.28).

$$R_{cu,1} = \frac{t_{ins,1}}{P_{s,1}\,\lambda_{ins}\,L}\,\frac{1}{6pq} \tag{6.28}$$

$P_{s,1}$ is evaluated over the all slot, taking into account left and right side. By this way it is possible to consider the parallel of the two resistances like in Fig.6.22b. The thermal insulation coefficient is assumed $\lambda_{ins} = 0,3$, this value is an equivalent insulation coefficient that takes into account the use of thermal resins in the slots. The external border of the slot and the top are modeled with (6.29) and (6.30). In equation (6.29) the $1/2$ at the beginning of the formula is for taking into account the parallel of the resistances on the left and right of the slot, see Fig.6.22b.

$$R_{cu,21} = R_{cu,22} = \frac{1}{2}\,\frac{t_{ins,2}}{h_{s,eq}/2\,\lambda_{ins}\,L}\,\frac{1}{6pq} \tag{6.29}$$

The upper portion of the slot is modeled by a single resistance directly connected to the yoke.

$$R_{cu,23} = \frac{t_{ins,2}}{w_{s,eq}\,\lambda_{ins}\,L}\,\frac{1}{6pq} \tag{6.30}$$

The network shown in Fig 6.23a, re-organized in Fig.6.25 can be solved in a simple way by system solution (6.31). Some assumption are done in order to rapidly calculate the winding temperature. The frame temperature is assumed constant and equal to $65°C$, that represents an experimentally verified temperature for IE4 motor.
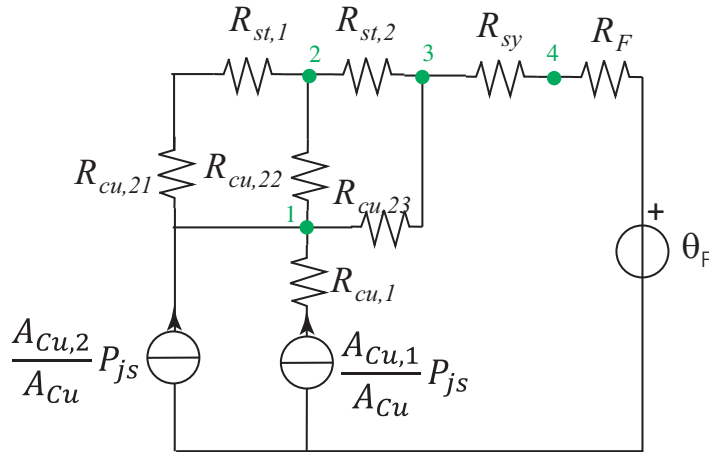
FIGURE 6.25: linear simplified thermal network

$$[R] [\theta] = [P] \tag{6.31}$$

Where

$$R = \begin{bmatrix} \frac{1}{R_{cu,21}+R_{st,1}} + \frac{1}{R_{cu,22}} + \frac{1}{R_{cu,23}} & -\frac{1}{R_{cu,21}+R_{st,1}} - \frac{1}{R_{cu,22}} & \frac{1}{R_{cu,23}} \\ -\frac{1}{R_{cu,21}+R_{st,1}} - \frac{1}{R_{cu,22}} & \frac{1}{R_{cu,21}+R_{st,1}} + \frac{1}{R_{at,2}} + \frac{1}{R_{cu,22}} & -\frac{1}{R_{st,2}} \\ -\frac{1}{R_{cu,23}} & -\frac{1}{R_{st,2}} & \frac{1}{R_{cu,23}} + \frac{1}{R_{st,2}} + \frac{1}{R_{sy}+R_F} \end{bmatrix} \tag{6.32}$$

$$[\theta] = [\theta_2, \theta_3, \theta_4]^T \qquad P = \left[P_{js}, 0, \frac{\theta_F}{R_F + R_{sy}}\right]^T \tag{6.33}$$

The comparison between the results of the model and 2D FE are shown in Fig.6.26. The different points exhibited in Fig.6.26 are related to different stator geometries, obtained in the bx plane maintaining constant b and moving x.
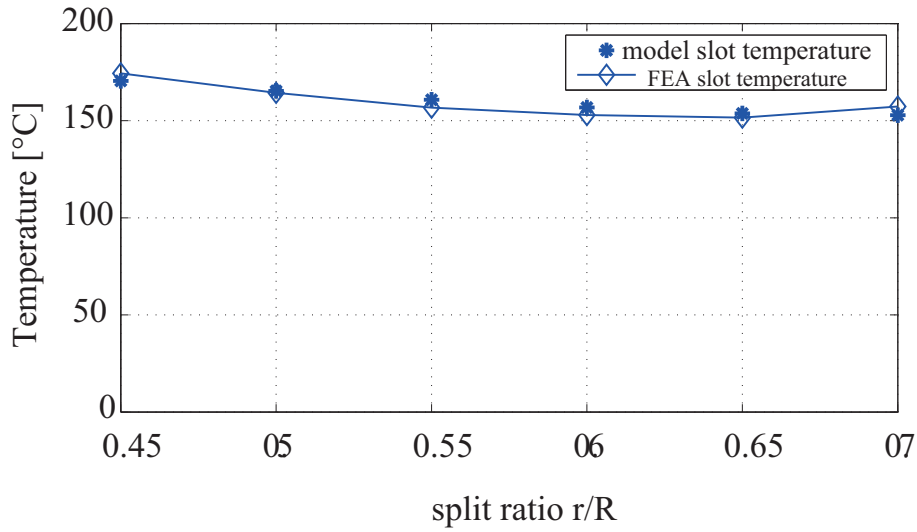
FIGURE 6.26: FE vs Model for a given geometry motor, varying the tooth length

The thermal model previously described will be used in Chapter 7.2 for the evaluation of the thermal behavior and Joule losses of different fractional slot motors.

6.6   Publications

- M. Gamba; G. Pellegrino; F. Cupertino (2014) , Optimal number of rotor parameters for the automatic design of Synchronous Reluctance machines. In: 2014 International Conference on Electrical Machines (ICEM), Berlino, Settembre 2014. pp. 1334-1340.

Chapter 7

Fractional Slot SyR Machine

7.1 Single tooth coils advantages and drawbacks

Polyphase distributed windings have long end connections that do not contribute to torque production, only Losses and weight. Fractional Slot winding solutions in SyR motors are intended to minimize the end turn length, proposing stator coils with a span of one tooth non overlapped, see Fig.7.2b. The feasible Fractional Slot configurations for a three phase machines are summarized in Fig.7.1, [46]. The validity of the configuration is related to the winding factor that should be higher than 0.8.

Number of poles

		2	4	6	8	10	12	14
	3	1/2	1/4		1/8	1/10		1/14
		0,866	0,866		0,966	0,866		0,866
	6		1/2		1/4	1/5		1/7
			0,866		0,866	0,866		0,866
	9			1/2	3/8	3/10	3/12	3/16
				0,866	0,945	0,945	0,866	0,945
	12				1/2	2/5		2/7
					0,866	0,966		0,966
	15					1/2		5/14
						0,866		0,866
	18						1/2	3/7
							0,866	0,945
	24							1/2
								0,866

Number of slots

FIGURE 7.1: applicable Slot-Pole Combination

With the associated benefits of FSW, challenges also arise when applying FSW to SyR rotor structure. The cause of this is the high space harmonic content due to the discrete placement of coils around the airgap periphery. FSW can be categorized by the number of slots/pole/phase (7.1)

$$q = \frac{Q_s}{2mp} = \frac{z}{n} = \begin{cases} tooth\ winding\ < 1, \\ Fractional\ > 1, \\ Positive\ Integer, \end{cases} \tag{7.1}$$

Where Q_s is the number of stator slots, p the pole pairs, m is the number of phases, in this work $m = 3$. The harmonic content can be rapidly evaluated with (7.2), this formulation can show the harmonic orders that are present in the various configurations, but not the amplitude.

$$h = \begin{cases} \pm \frac{1}{n}\left(6g + 2\right) & n = even, \\ \pm \frac{1}{n}\left(6g + 1\right) & n = odd, \end{cases} \tag{7.2}$$
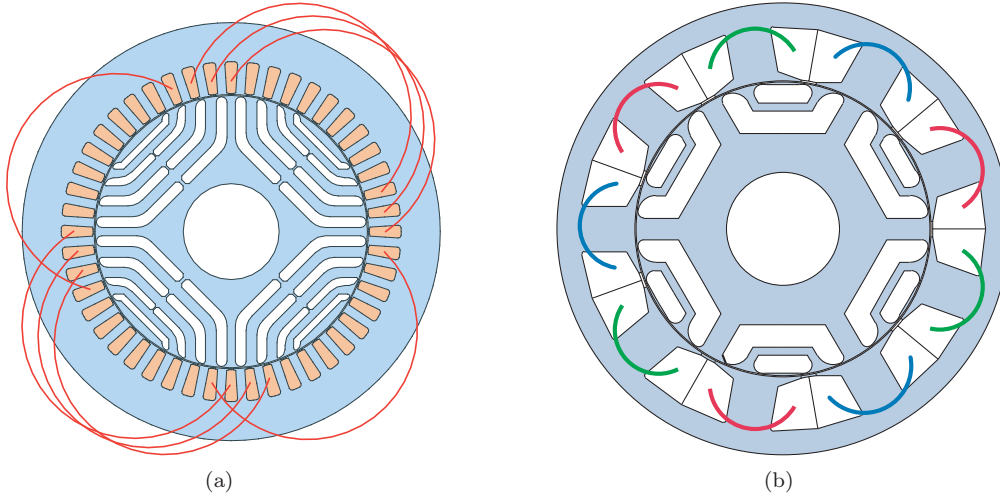
Where $g = \pm 1, 2, 3...$

FIGURE 7.2: Cross section of a) DW SyR motor b) q=1/2 motor

Considering Fig.7.1 solutions with $q = 1/2$ are present for all the combinations of slots and poles. Higher winding factor is reached by solutions $q = 2/5$ and $q = 2/7$. This solutions are also the most used in literature. The main problem is represented by the fact that $q = 2/5$ requires 10 poles, value quite big for common industrial applications. An investigation carried out with SyRE on 10 poles machines will be shown in the following . Torque density and torque ripple are compared between a DW (q=3), FSW (q=1/2) and q=2/5. Fig.7.3 shows the Pareto front for winding solutions: DW, FSW q=1/2 and FSW q=2/5. The same motor frame is used, [47], machines are designed for direct drive solutions, for example in elevator applications under VSI supply. The Pareto results show that the torque density of the DW is higher compared to the fractional slot winding solutions. By increasing the number of rotor flux barriers it is possible to improve the torque density without penalizing the torque ripple. FSW solutions with q=1/2 show higher torque density compared to q=2/5. This is related to the fact that q=1/2 machines present comparable magnetizing behavior of q=2/5 and higher anisotropy with benefit on torque density and power factor. FSW q=2/5 presents lower performance compared to the other solutions in terms of torque density. This configuration seems to be quite insensible to flux barriers variation, ripple and torque are quite constant varying the number of flux barriers. Torque ripple is lower and in general comparable to the DW motors. The $d - q$ linked fluxes are shown in Tab.7.1 and 7.2.
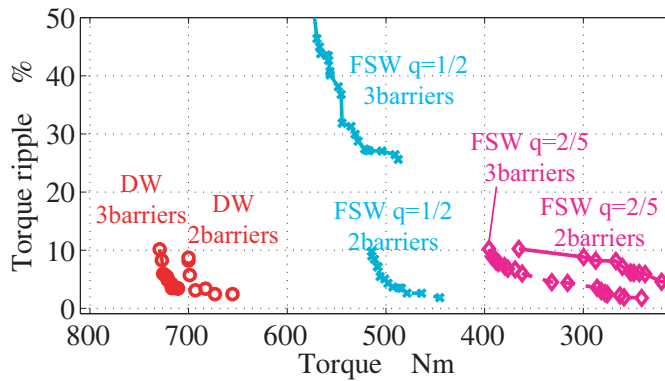
FIGURE 7.3: Pareto front of 10poles motor for different winding configuration and rotor flux barriers at $1.4\,i_0$

It is possible to see in Tab.7.1 and 7.2 that solutions with q=1/2 present higher anisotropy respect to q=2/5. Anisotropy is defined according to (7.3). By (7.4) increasing anisotropy also the power factor increase. In solutions with q=1/2 the λ_d component is lower compared to q=2/5. This is mainly related to the lower k_w. On the other hand, the difference $(L_d - L_q)$ for q=1/2 is bigger than q=2/5 and this, justifies the higher torque density of q=1/2.

TABLE 7.1: Machine anisotropy at rated current 120A

	DW	FSW q=1/2	FSW q=2/5
$\lambda_d[Vs]$	1.05	0.86	0.9
$\lambda_q[Vs]$	0.233	0.3	0.42
ξ	4.52	2.8	2.19

TABLE 7.2: Machine anisotropy at two times the rated current 240A

	DW	FSW q=1/2	FSW q=2/5
$\lambda_d[Vs]$	1.21	0.96	1.1
$\lambda_q[Vs]$	0.373	0.455	0.64
ξ	3.2	2.1	1.71

$$\xi = \frac{L_{md} + L_\sigma}{L_{mq} + L_\sigma} \tag{7.3}$$

where L_{md} and L_{mq} are the d-q purely magnetizing components, L_σ is representative of the leakage components.

$$cos(\phi_{max}) = \frac{\xi - 1}{\xi + 1} \tag{7.4}$$

The MMF of the three machines under comparison are shown in Fig.7.4a,b,c. The solutions refer to equal current loading for all the machines under test. The corresponding harmonic behavior is shown in Fig.7.5, [48]. Solution with $q = 1/2$ does not present sub-harmonics. On the other hand it presents an harmonic spectrum composed by odd and even harmonic orders. Solutions with $q = 2/5$ instead presents sub-harmonics, this winding topology shows only odd harmonic orders.

(a)

(b)

(c)
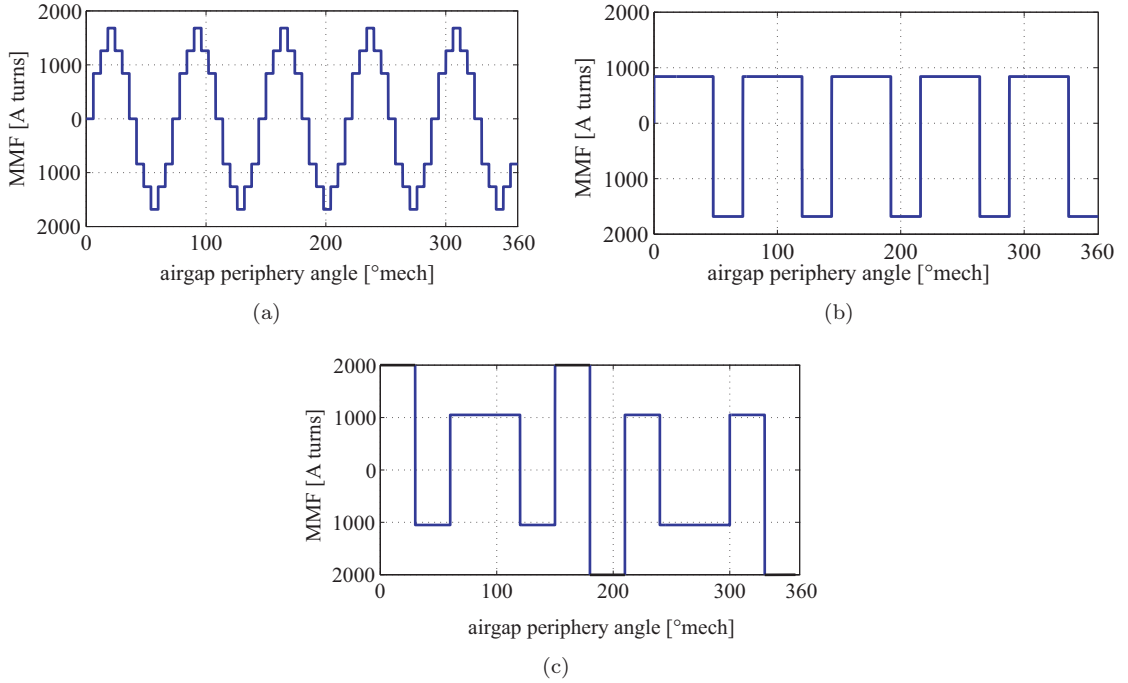
FIGURE 7.4: MMF; a)q=2; b) q=1/2; c) q=2/5

7.1.1   Mathematical Model for Torque Ripple estimation

The mathematical model used for a preliminary estimation of the torque ripple is based on the permeance network shown in Fig 7.6, [49], [50]. The simplified hypotheses are ideal iron $\mu_{Fe} \to inf$,

(a)

(b)

(c)
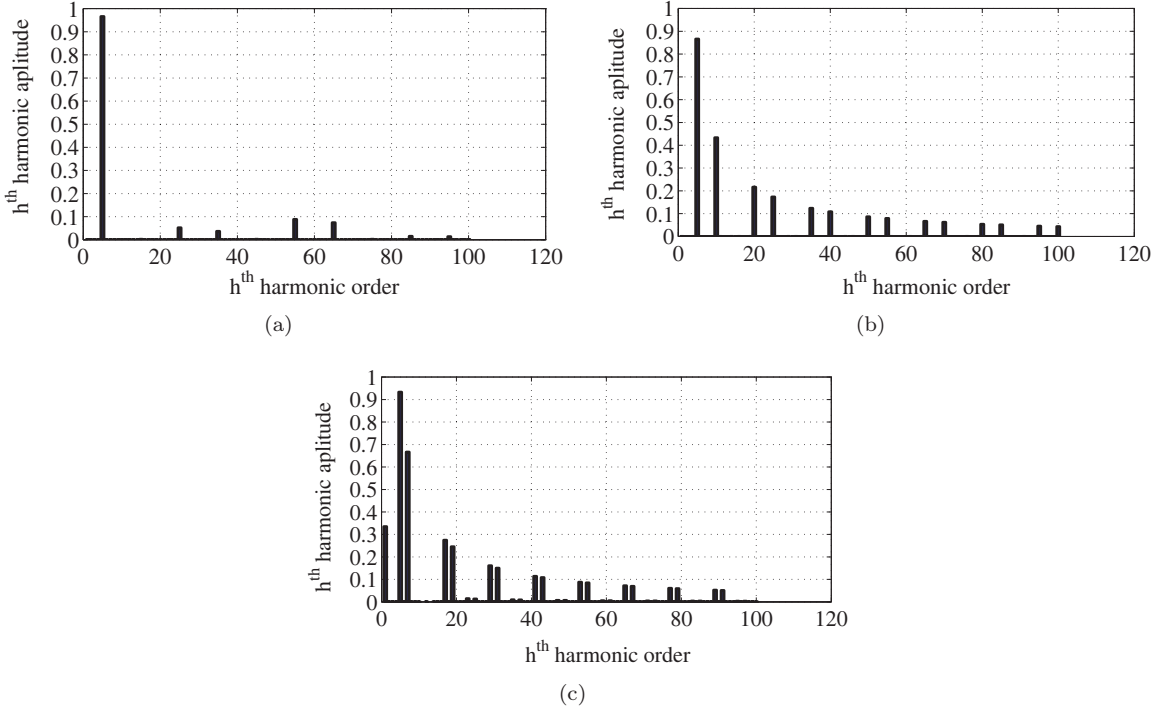
FIGURE 7.5: Harmonic order and amplitude; a)q=2; b) q=1/2; c) q=2/5

no ribs at the airgap or inside the rotor. Considering the symmetry of the network in Fig 7.6, it is possible to solve an equivalent half pole network, see Fig 7.7. This simplification permits to reduce the size of the matrix for the numeric resolution, with faster implementation.
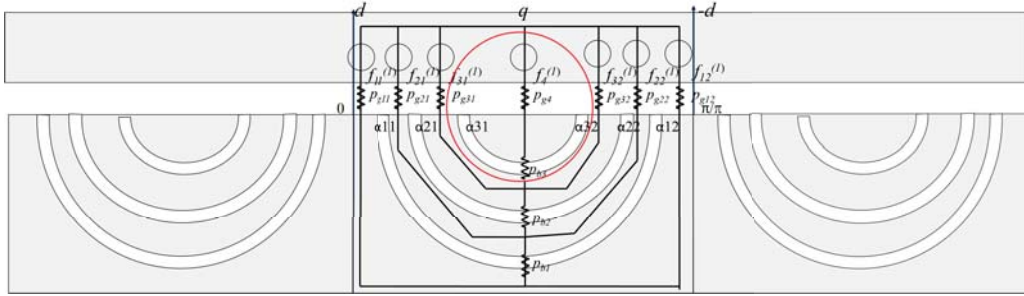
FIGURE 7.6: Equivalent permeance circuit of all poles

The equivalent MMF generator $f_1^{(1)}$, represents the generator for the first pole first flux guide. The upper number in round brackets represents the selected pole, the lower number: the flux guide. The mean value of the MMF applied to a flux guide can be expressed as in (7.5), (7.7), where $F_{s,r}$ is the MMF on the rotor reference frame.

$$f_1^{(k)} = f_{21}^{(k)} + f_{22}^{(k)} = \frac{1}{2\,\Delta\alpha}\left(\int_{\alpha_{11}^{(k)}}^{\alpha_{21}^{(k)}} F_{s,r}(\alpha)\,d\alpha + \int_{\alpha_{22}^{(k)}}^{\alpha_{12}^{(k)}} F_{s,r}(\alpha)\,d\alpha\right) \tag{7.5}$$

$$f_2^{(k)} = f_{21}^{(k)} + f_{22}^{(k)} = \frac{1}{2\,\Delta\alpha}\left(\int_{\alpha_{21}^{(k)}}^{\alpha_{31}^{(k)}} F_{s,r}(\alpha)\,d\alpha + \int_{\alpha_{32}^{(k)}}^{\alpha_{22}^{(k)}} F_{s,r}(\alpha)\,d\alpha\right) \tag{7.6}$$
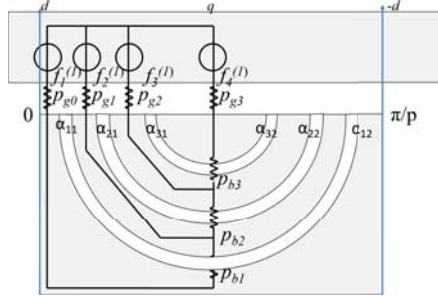
FIGURE 7.7: Equivalent permeance circuit of 1 pole with the equivalent Thevenin simplification
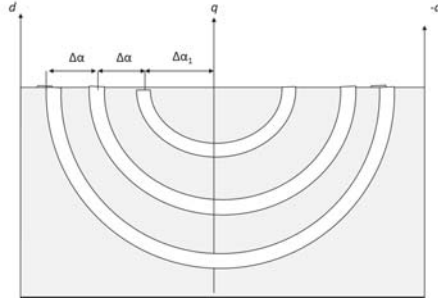
FIGURE 7.8: angle at the arigap between flux barriers

$$f_3^{(k)} = \frac{1}{2\,\beta} \int_{\alpha_{31}^{(k)}}^{\alpha_{32}^{(k)}} F_{s,r}\, d\alpha \tag{7.7}$$

The equivalent permeance shown in Fig. 7.7 can be obtained considering the equivalent Thevenin permeance, along the red circle in Fig. 7.6. Flux barriers are assumed uniformly distributed at the airgap, like in Fig. 7.8.

$$P_{g0} = \frac{\mu_0\, r\, L}{g} \tag{7.8}$$

$$P_{g,i} = \frac{\mu_0\, r\, L}{g} 2\Delta\alpha \qquad i = 1 : n_{lay} - 1 \tag{7.9}$$

$$P_{g,n_{lay}} = \frac{\mu_0\, r\, L}{g} 2\Delta\beta \tag{7.10}$$

$$P_{b,k} = \frac{\mu_0\, S_k\, L}{l_i} \tag{7.11}$$

Where r is the airgap radius, L the stack length, g the airgap length, S_i flux barrier length, l_i flux barrier width. In a FSW motor the spider potential is not always zero. For solving the network, it is necessary to solve the spider potential, first. This is obtained solving the first row and column from the matrix system (7.14). At this point applying the Millman Theorem to the X-Y points according to Fig 7.10 is possible to evaluate r_0 and than r_1, r_2, n_{lay}.

$$r_0 = \frac{P_{eq} \sum_{=1}^{n_{lay}} f_{eq}^{(k)} + P_{g,0} \sum_{k=1}^{n_{lay}} f_0^{(k)}}{n_{lay}\, P_{eq} + n_{lay}\, P_{g,0}} \tag{7.12}$$

In matrix foorm the solution system is

$$[A]\, r = [B]\, f \tag{7.13}$$
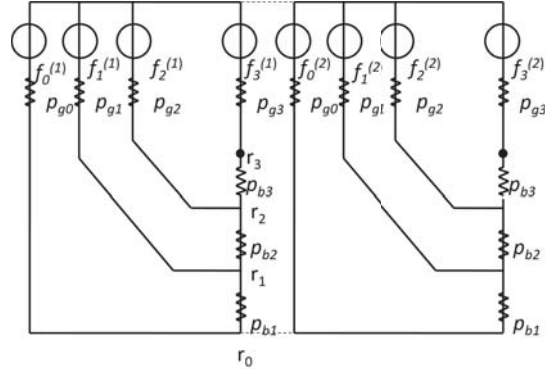
FIGURE 7.9: permeance network of two consecutive poles

In this formulation $[r]$ and $[f]$ are matrices and not only vectors, because their contributions change over the different poles of the machine.

$$A = \begin{bmatrix} P_{b1} + P_{g,0} & -P_{b,1} & 0 & 0 \\ -P_{b,1} & P_{b,1} + P_{b,2} + P_{g,1} & -P_{b,2} & 0 \\ 0 & -P_{b,2} & P_{g,2} + P_{b,2} + P_{b,3} & -P_{b,3} \\ 0 & 0 & -P_{b,3} & P_{b,3} + P_{g,3} \end{bmatrix} \qquad A = [n_{lay} + 1 \; x \; n_{lay} + 1] \tag{7.14}$$

$$r = \begin{bmatrix} r_0^{(1)} & \cdots & r_0^{(nlay)} \\ r_1^{(1)} & \cdots & r_1^{(nlay)} \\ \cdots\cdots \\ r_{n_{lay}}^{(1)} & \cdots & r_{n_{lay}}^{(nlay)} \end{bmatrix} \tag{7.15}$$

$$f = \begin{bmatrix} f_0^{(1)} & \cdots & f_0^{(2p)} \\ f_2^{(1)} & \cdots & f_2^{(2p)} \\ \cdots\cdots\cdots\cdots\cdots \\ f_{n_{lay}}^{(1)} & \cdots & f_{n_{lay}}^{(2p)} \end{bmatrix} \tag{7.16}$$

$$B = \begin{bmatrix} P_{g,0} \\ P_{g,2} \\ \cdots\cdots \\ P_{g,n_{lay}} \end{bmatrix} \tag{7.17}$$
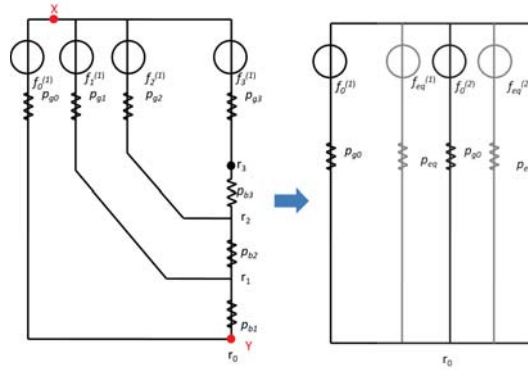
FIGURE 7.10: permeance network configuration for the evaluation of r_0

Once is known the rotor magnetic potential is possible to evaluate the flux density at the airgap, (7.18).

$$B_g = \frac{\mu_0}{g}\left(F_{s,r} - r\right) \tag{7.18}$$

Than the instantaneous torque can be calculated by

$$T = r\,L\int_0^{2\pi} B_g\,\frac{dF_{s,r}}{d\alpha}d\alpha \tag{7.19}$$

The torque ripple function of the equivalent number of slots per pole pairs n_r for q=1/2 solution is shown in Fig.7.11.
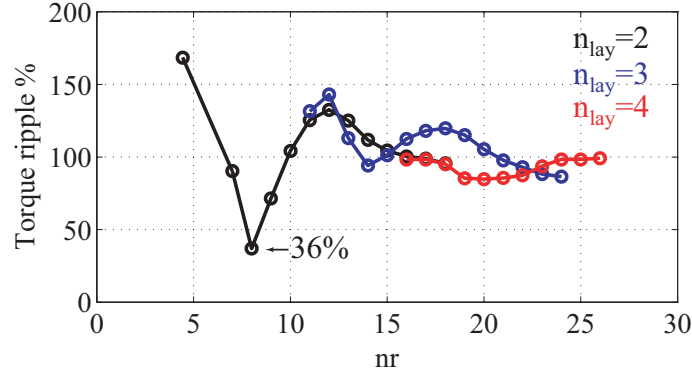
FIGURE 7.11: Torque ripple results with the mathematical model for q=1/2

The torque waveform function of rotor position and FFT are shown in Fig.7.12. The evaluation of the torque is at the same current loading, moving in a combination of feasible machines, with constant distribution of the flux barriers at the airgap in agreement with design rules shown in Fig 7.8. The parametric investigation permits to understand that only the two layers motor is able to presents a strong reduction of the torque ripple, see Fig.7.11. This reduction is related to the minimization of the six-th and twelve-th harmonics in the torque spectrum as shown in Fig 7.12a,b.
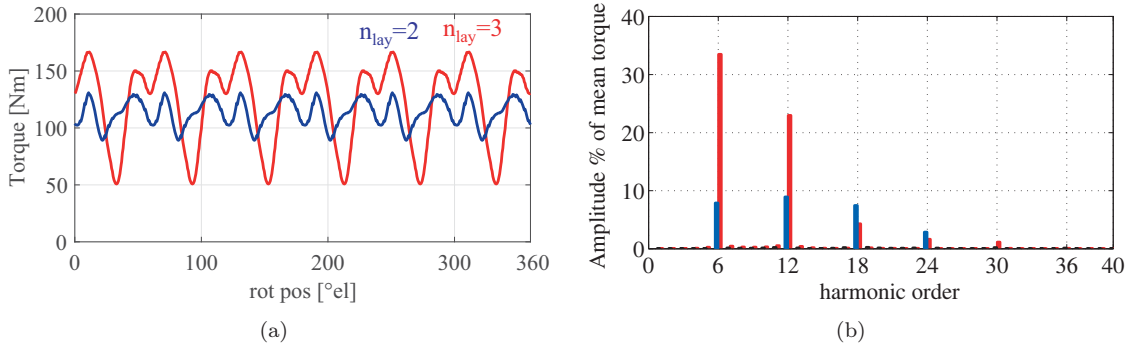
FIGURE 7.12: a) Torque vs rotor position; b) FFT of the torque waveform

7.1.2 Mathematical Model Bottom Line

The simplified mathematical model is able to estimate the harmonic interaction between stator and rotor. On the other side, the method is not able to give a reliable prediction of the mean torque between different rotors and stator configurations. This is related to the hypothesis of linear iron with $\mu_{Fe} = inf$. Instead it is possible to observe that the torque ripple estimation is quite good. The iron saturation puts in evidence that for the torque ripple reduction, it is important the position of the flux barriers at the airgap, but also the barriers width and the iron islands width. A ripple around or over 100% for all machine except the solution with $n_{lay} = 2$ and $n_r = 8$ is shown in Fig.7.11. Due to the higher ripple a systematic optimization procedure is carried on with the help of SyRE.

7.2   Design of the FSW-SyR Prototype

The machine was designed according to data reported in Tab.7.3. A three phase, q=3 SyR motor like
the one shown in Fig 7.2 is used as a benchmark. This machine is used in industrial environments:
pumps, funs... It is self ventilated, with non magnetic aluminum frame. Data reported in Tab7.3, are
maintained constant also during the optimization process. For simplifying the comparison between
motors, the airgap radius is considered constant and also the external frame (external stator diameter
and stack length).

TABLE 7.3: Machine Specification

Stator outer diameter [mm]	100
Rotor outer diameter [mm]	65
Airgap length [mm]	0.5
Stack length [mm]	215
Number of series turns per phase N_s	87
Nominal Power [kW]	7,5
Nominal Speed [rpm]	1500
Maximum Speed [rpm]	5000

7.2.1   Temperature Estimation

the over-temperature for the DW and FSW motors are summarized in Tab.7.4. The DW solution
presents better thermal behavior respect to the FSW motors. This is related to the higher inner slot
surface and lower radial area of the slots for the DW motor. For FSW motors, it is evident that
passing from $p = 2$ to $p = 3$ the over-temperature is reduced of one half. The reduction, increasing
the number of poles become lower and lower. This is related to the increment of the inner slot surface
necessary to the heat dissipation and to the lower cross section of the slot. In Tab.7.4 FSW motors
present $k_{cu} = 0,6$ this value is quite reasonable for this winding solution. Instead it is not acceptable
for the DW (q=3) motor, where a value of $k_{cu} = 0,44$ is considered.

TABLE 7.4: Temperature of the machines under comparison @ same output power
7,5kW (1500rpm)

q	p	$R_s(20°C)\,[\Omega]$	$P_{js}(20°C)\,[W]$	$\Delta\theta\,[°C]$
3	2	0,348 ($k_{cu} = 0,44$)	300	7
1/2	2	0,164 ($k_{cu} = 0,6$)	301,35	40
1/2	3	0,106 ($k_{cu} = 0,6$)	241,84	20
1/2	4	0,09 ($k_{cu} = 0,6$)	279	16,5
1/2	5	0,079 ($k_{cu} = 0,6$)	284	13,5

7.3   Selection of the optimal number of poles

The number of pole pairs must be preliminary choice. An investigation is carried on, from the efficiency
point of view. A simplified design procedure is used, also validated by FEA in order to find the optimal
number of poles that minimizes losses in the machine. The general torque equation is:

$$T = \frac{3}{2}\,p\left(\frac{\xi-1}{\xi}\right)L_{md}\,i^2\,\frac{sin(2\gamma)}{2} \qquad (7.20)$$

L_{md} is the magnetizing inductance, that for a general machine can be expressed by:

$$L_{md} = \frac{6}{\pi}\,\frac{r}{g}\,\mu_0\,L\,\frac{\left(k_w N_s\right)^2}{p^2} \qquad (7.21)$$

In the model is assumed that the saliency ratio $\xi = L_{md}/L_{mq}$ is constant. This hypothesis is
confirmed by FE investigation as will be shown in Fig.7.13. γ is the current vector angle. In a linear

case, the current angle along the MTPA is 45°el. Writing the Joule losses as a function of torque, equation (7.22) is obtained.

$$P_{js} = T \frac{4\pi}{\mu_0} \frac{g}{r} \frac{\xi}{\xi - 1} \frac{1}{\sin(2\gamma)} \rho \frac{p \, K_{end}}{k_w^2 \, K_{cu} \, A_s} \tag{7.22}$$

K_{end} is the end winding factor whose formulation is detailed in (6.6),(6.7). A_s is the total slots surface.

$$A_s = \pi \, l_t \left(2R - l_y - l_t\right) - 6pq \, w_t \, l_t = 2b\pi \left(r^2 - rR\right) + \pi\left(R^2 - r^2\right) + \frac{(b\pi r)^2}{3pq} - \frac{\pi^2 br}{3pq}\left(\frac{R + r}{2}\right) \tag{7.23}$$

Summarizing the various geometric parameters into two main geometric constant A and B, the slots area function of p is shown in (7.26).

$$A = \frac{(b\pi r)^2}{3pq} - \frac{\pi^2 br}{3pq}\left(\frac{R + r}{2}\right) \tag{7.24}$$

$$B = 2b\pi \left(r^2 - rR\right) + \pi\left(R^2 - r^2\right) \tag{7.25}$$

$$A_s = B + \frac{A}{p} \tag{7.26}$$

The end winding factor is defined as $K_{end} = L + l_{end}$; substituting (6.7) in K_{end} definition, it is possible to obtain the end winding factor function of the pole pairs (7.27):

$$C = \frac{\pi}{3\,q\,L}\left(b\,r + \pi\left(\frac{r + R}{4}\right)\right) \quad D = \frac{b\,r}{2\,L}\left(\frac{\pi}{6\,q}\right)^2 \quad K_{end} = 1 + \frac{1}{2\,L}\left(\frac{C}{p} - \frac{D}{p^2}\right) \tag{7.27}$$

Substituting (7.26) and (7.27) in (7.22) and deriving it, (7.28) shows the pole pairs that minimize losses.

$$\frac{\partial P_{js}}{\partial p} \longrightarrow p_{min} = \frac{1}{2B}\left(\sqrt{2\left(2A^2 - CAB - DB^2\right)} - 2A\right) \tag{7.28}$$

In Fig.7.13 is shown the results of previous formulation and the FEA results. A discrepancy exist related to the no exact estimation in the model of the anisotropic factor ξ and L_{md}. On the other side qualitatively the results are equivalent. Considering only Joule losses, solution with $p = 3$ is the best one, introducing the iron losses (green line in Fig7.13), the discrepancy between $p = 2$ and $p = 3$ become lower; but three pole pairs remain the solution at minimum losses. The Joule losses evaluated in Fig7.13 take into account the different copper temperature varying the number of poles summarized in Tab.7.4.
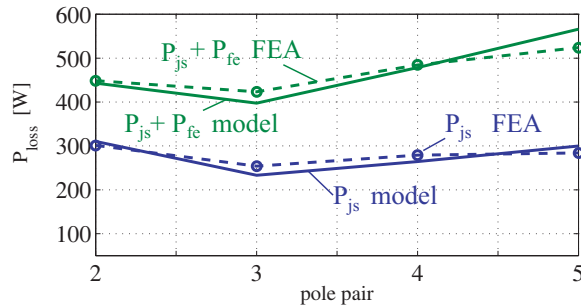

FIGURE 7.13: Losses function of pole pair, the output torque is constant and equal to 50Nm @ 1500rpm

7.3.1 Poles selection according to Thermal and Loss results

All the machines shown in Fig.7.13 rotate at the nominal speed set to 1500rpm and are loaded at the same output torque. The designed machine is selected with 6 poles. The reason of the choice is related to the combined thermal and electrical considerations. The six poles represent a minimum of the total losses, the Joule losses reduction is due not only to the end winding length reduction but also to the copper temperature reduction. The Iron Losses presents an opposite trend. Losses increase with pole pair due to the increment of the electrical frequencies.

7.3.2 Optimization variables

The Segment geometry (Seg), whose construction rules are described in previous Chapters, is used to design the motor. The optimization procedure was executed over 4CORE PC, with 10000 functional calls,with four repetitions of the optimization procedure. All the machine generated during the optimization algorithm are evaluated at constant Joule losses. The selected joule losses $P_{j,s} = 320W$ is the same generated by q=3 motor for producing 60Nm that correspond to an overload of 20%, respect to the nominal value reported in Tab.7.3. The total number of variables used in the optimization are seven, and the feasible range of variation is shown in Tab 7.5. A sensitivity analysis is conducted varying the number of flux barriers. In Fig 7.14a it is possible to see that solutions with 3, 4 flux barriers in the rotor, are not able to produce a consistent reduction of the torque ripple. The two flux barriers solution presents two different front. One with similar ripple to the other cases and one where is present the selected machine with ripple comparable to the DW. The torque ripple profile for the benchmark (q=3), the selected low ripple solution (q=1/2 nlay=2) and a q=1/2 3lay is shown in Fig7.14b. It is evident that the ripple exhibited by q=1/2 3lay is not acceptable for common application.

TABLE 7.5: Optimize variables

| | Constraint | |
variable	min	max
$\Delta\,\alpha_{pu}$	0,3	0,6
$\Delta\,h_{c,pu}$	0,3	0,6
$\Delta\,x_{pu}$	0,3	0,6
γ	40	70
l_t	40	70
w_t	5	10
$w_{so,pu}$	0,1	0,5

7.3.3 The Armchair Optimal Machine

The selected Low ripple solution over the Pareto Front, in Fig7.14a, presents the geometric shape shown in Fig7.15. This solution presents a quite thin flux guide, between the two flux barriers. The position of the flux barriers at the airgap is quite regular, and an equivalent number of rotor slots per pole pairs could be defined: $n_r = 8$. The equivalent n_r is shown in Fig.7.15, by blue dot on the periphery of the rotor. A summary of the main geometric data of this machine are reported in Tab 7.6. The tooth width w_t is 44% of the slot pitch $\tau_s = \pi\,r/(3pq)$, the yoke length l_y is 52% of the tooth width, w_t; $w_{so,pu}$ is the slot opening in pu to the slot pitch.

TABLE 7.6: Armchair Data

variable		value
w_t		20 $(0,44\,\tau_s)$
l_y		10,31 $(0,52\,w_t)$
$\Delta\,h_{c,pu}$	$k = 1\,to\,n_{lay}$	[0.65 , 0.68]
$\Delta\,x_{pu}$		[0 0,39]
$\Delta\,\alpha_{pu}$	$k = 1\,to\,n_{lay}$	[0.3 , 0.47]
$w_{so,pu}$		0,15
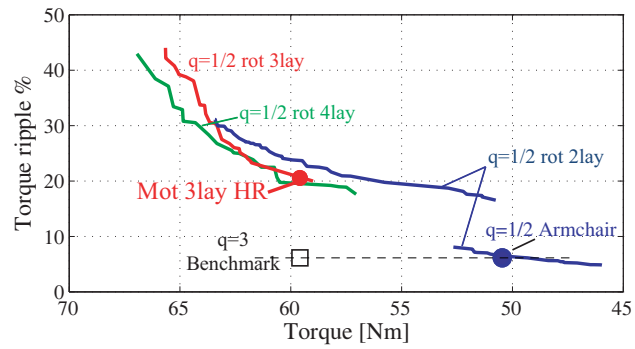
(a)
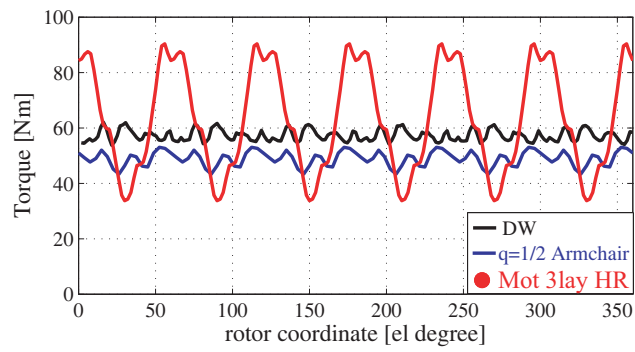
(b)

FIGURE 7.14: a) Pareto Front; b) Torque ripple comparison; machines are supplied in order to produce same Joule losses Pjs = 320W

FIGURE 7.15: rotor cross section of the Armchair Solution

7.4   3D Effect in anisotropic machine

This section put in evidence a 3D effect that penalizes the torque density and power factor. The reasons that will become clear in the next chapters are related to the fact that in an anisotropic machines, like synchronous reluctance or IPM motors, the field behavior of the machine change from the d axis to the q axis configuration. This is related to the equivalent m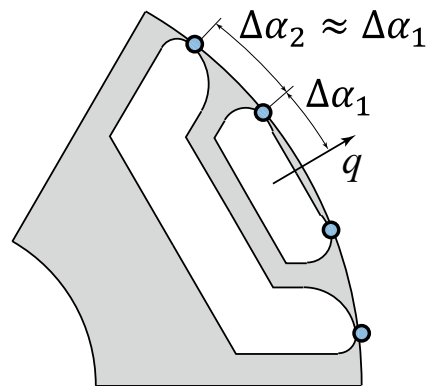agnetic airgap that increases passing from the d-axis to the q-axis. The increment of the equivalent airgap increases the magnetic field along the border of the machine, see Fig 7.16. This higher fringing effect along the q-axis improve the linked flux respect to the one expected from the 2D-FEA. The higher q-axis flux reduces the machine anisotropy with bad consequences on torque density and power factor. In the following it will be show that for simple end winding configuration, like tooth winding solutions, a mathematical model can be used to take into account this 3D effect. Finally 3D and 2D-FEA results are compared with experimental tests on a prototype showing that 3D-FEA are necessary to accurately modeling the q-axis behavior.

7.4.1   Mathematical evaluation of the end turn and fringing inductance

The magnetic field in the end winding region of a radial machine can be subdivided into two components:

1. Fringing flux (λ_{fr})

2. Field produced by the end coil (λ_{coil})
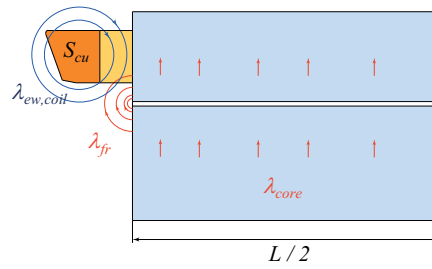
FIGURE 7.16: Flux component along the axial length of the machine

In order to model the fringing flux component in the airgap region, it is considered the simplified permeance network, shown in Fig7.17. In the model, iron is considered linear and no magnetic drop is taken into account, the fringing flux lines are modeled with circular geometry, see Fig.7.17a.

Due to symmetry reasons is possible to focus the analysis to a half of the core length. The permeance network, Fig.7.17 models only the flux lines in air, due to the initial hypothesis is not considered the magnetic drop in the core. The permeance at the airgap was modeled by (7.29).

$$P_g = \frac{\mu_0\, L/2\, \tau_{slot}}{g} \tag{7.29}$$

Where L is the axial length of the machine,g is the airgap length, τ_{slot} the slot width. The fringing flux lines shown in Fig7.17a, are modeled as flux guide with circular shape. The formula (7.30), describes the k-element. The fringing effect is analyzed assuming a number of elements higher than one, for having an indication of the slope of the reduction of the flux density, increasing the distance from the core.

$$P_{gf,k} = \frac{\mu_0\, \tau_{slot}\, \Delta r}{\pi\, r_k} \qquad k = 1 : n_{element} \tag{7.30}$$

The value Δr represents the width of the flux guide. It is evaluated, defining the number of elements at the airgap, $n_{element}$, (es. $n_{element} = 10$), $\Delta r = \frac{Y}{n_{element}}$, where Y is the upper limit in the xy coordinates of Fig.7.17a; than $r_k = \frac{g}{2} + \frac{2k-1}{2}\Delta r$.

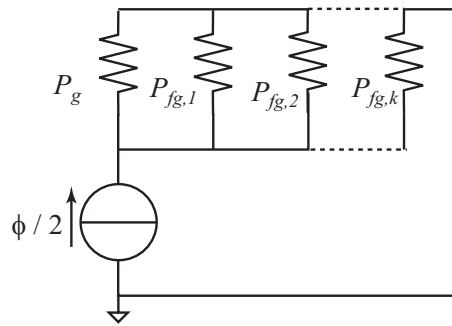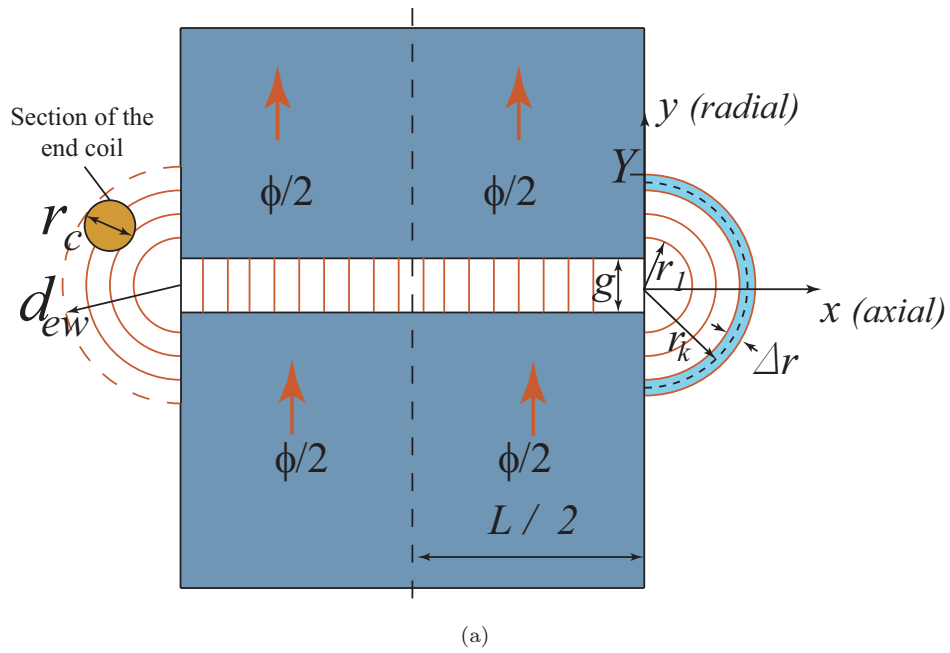FIGURE 7.17: (a) flux lines geometry for the simplified mathematical model, (b) axial permeance network

The formula (7.31), is quite general and valid for reluctance and induction motor. After some manipulation it is possible to evaluate the flux at the airgap (7.33) over a slot width. It represents the supply condition shown in Fig7.17b.

$$\lambda_d = \frac{6}{\pi^2} \mu_0 \frac{\tau_p}{pg} L \left(k_w N_s \right)^2 \tag{7.31}$$

$$\lambda_d = k_w N_s \phi_{pole} \tag{7.32}$$

Solving the network shown in Fig.7.17b, it is possible to evaluate the fluxes in each flux tube on the border area. For doing this, with (7.33), it is evaluated the core flux over an end winding turn, see Fig.7.18a. Than the flux density related to the $k - element$ is calculated with (7.34). Finally the flux density on the border area is calculated with (7.35).

$$\phi = \frac{\lambda_d}{k_w N_s} \frac{\tau_{slot}}{\tau_p} \tag{7.33}$$

$$\phi_{fg,k} = \frac{\phi}{2} \frac{P_{fg,k}}{P_g + \sum_{k=1}^{n_{element}} P_{fg,k}} \tag{7.34}$$

$$B_{fg,k} = \frac{\phi_{fg,k}}{\Delta r \, \tau_{slot}} \tag{7.35}$$

The result of (7.35) is shown in Fig7.18b. For the correctness of the comparison, it is assumed to move along the same flux lines, see Fig.7.17a. By this way, increasing the airgap, (7.29) is reduced and consequently is reduced the denominator in (7.34). Than the flux components that represent the fringing effect contribution increases.

In Fig.7.18b it is evident that increasing the airgap, the flux density in the space near the core increases and consequently it is higher the flux linked with the end turns. The trend of this phenomena is also verified by FEA, see Fig.7.19, where it is possible to appreciate that in q-axis configuration the flux density in the region near the core it is higher than in the d-axis situation. This considerations are related to the fringing effect (not to the Carter analysis). The first conclusion is that the the end winding inductance is higher in the q axis.

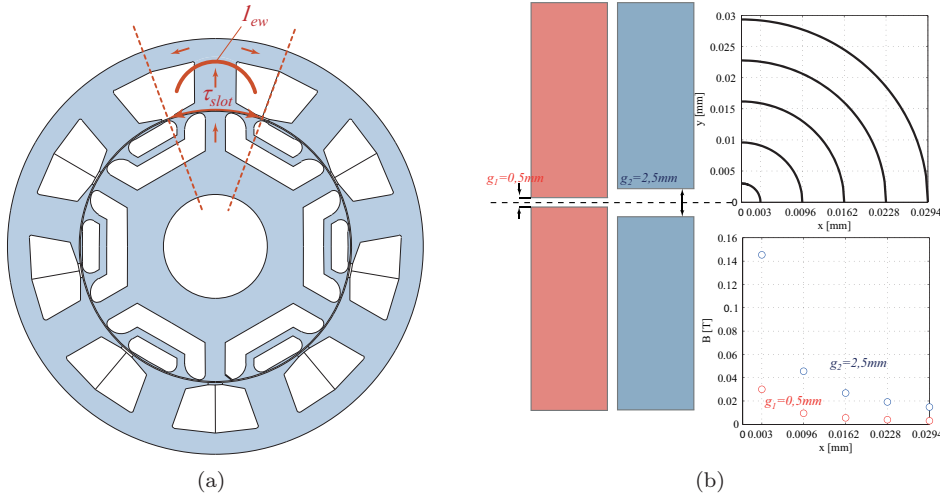(a)   (b)

FIGURE 7.18: (a) slot geometry and end winding turn (b) fringing effect and flux density value

7.4.2   Flux linkage components

The phase flux linkage component can be split as in (7.36).

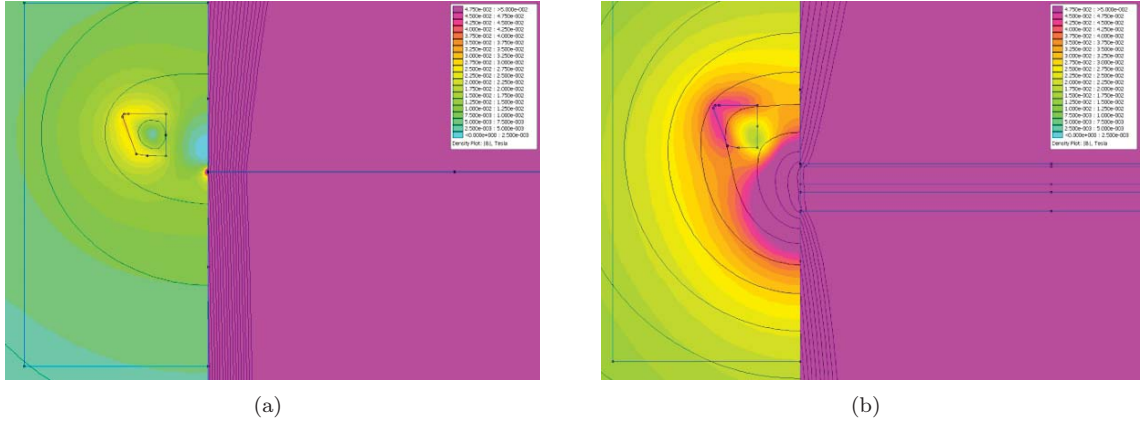$$\lambda_{phase} = \lambda_{c,L} + \lambda_{slot} + \lambda_{ew} + \lambda_{fr} \tag{7.36}$$

FIGURE 7.19: 2D FEA of the axial section of the machine, (a) d-axis configuration;
(b) q-axis configuration

where λ_{phase} is the total flux linked with the a phase, $\lambda_{c,L}$ is the core flux related to the mechanical axial length of the machine, λ_{slot} the slot leakage component, λ_{ew} end winding leakage flux, λ_{fr} additional flux component linked with the coil due to border fluxes. The flux component $\lambda_{c,L}$ and λ_{slot} can be evaluated with 2D FEA. Components λ_{ew} and λ_{fr} must be evaluated with 3D FEA. It is possible to take into account the 3D effect by simple formulation. In (7.37) it is assumed that the fringing flux components are linked with all the coil turns, even if most part of the symbols are just detailed in previous chapter. N_s is the number of turns in series per phase, p is the pole pairs, q the number of slots per pole per phase, I is the phase current, d_{ew} is the distance of the end turn from the core, B_g represents the flux density in the region near the core evaluated in (7.35) with the procedure previously detailed.

$$\lambda_{fr} = 2p\,q \left(\frac{N_s}{2pq}\right) \tau_{slot} \int_0^{d_{ew}} B_g(l)\,dl = 2\,N_s\,\tau_{slot} \int_0^{d_{ew}} B_g(l)\,dl \qquad (7.37)$$

The self inductance of the end turn winding can be really complicate to evaluate if is considered a trapezoidal section of the end turn. A more simple way is to approximate the self inductance of the end turn with the inductance of a finite length conductor with circular section. In (7.38), τ_{slot} is the slot width and r_c is the coil external radius.

$$\lambda_{ew} = \frac{\mu_0}{2\,\pi} \left(\frac{N_s}{2pq}\right)^2 I \left[l_{ew} \ln\left(\frac{l_{ew} + \sqrt{l_{ew}^2 + r_c^2}}{r_c}\right) + r_c - \sqrt{l_{ew}^2 + r_c^2}\right] \qquad (7.38)$$

7.4.3 3D FEA Setup

In order to evaluate the 3D effect a transient with motion 3D FEA is used. The computational time is quite long, this mean that is not feasible investigate all the $i_d\,i_q$ plane. Only the no load flux curves are calculated. Knowing the 3D effects it is possible, by difference between 3D FEA results and 2D FEA, to estimate the end winding and the fringing effect, see (7.39). Formula (7.39) is used in the following to validate (7.38) and (7.37).

$$\lambda_{ew} + \lambda_{fr} = \lambda_{3D,FEA} - \lambda_{2D,FEA} \qquad (7.39)$$

flux density in the end winding region is shown in Fig 7.20. It is possible to appreciate the higher flux density in the lower portion of the end turn in Fig.7.21 respect to Fig.7.20. This higher value of the flux density is related to the higher fringing effect.

The results between the FEA and the model are summarized in Tab 7.7. The model with equations (7.38) and (7.37) shows a good estimation of the 3D-FEA results. The error between the model and the FEA is around 10%, this is reasonable, considering the simplified formulation used in the estimation of the phenomena. On the other side, the model permits to predict, in a rapid way, the difference between the d and q axis that is important in the estimation of the torque and power factor reduction due to this phenomena.
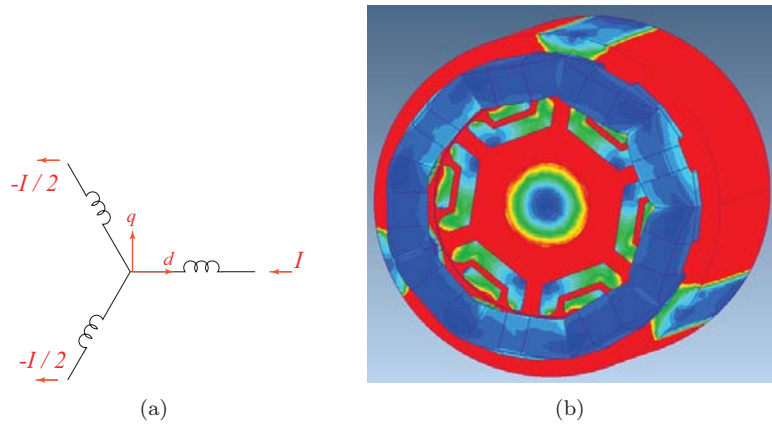
(a)   (b)

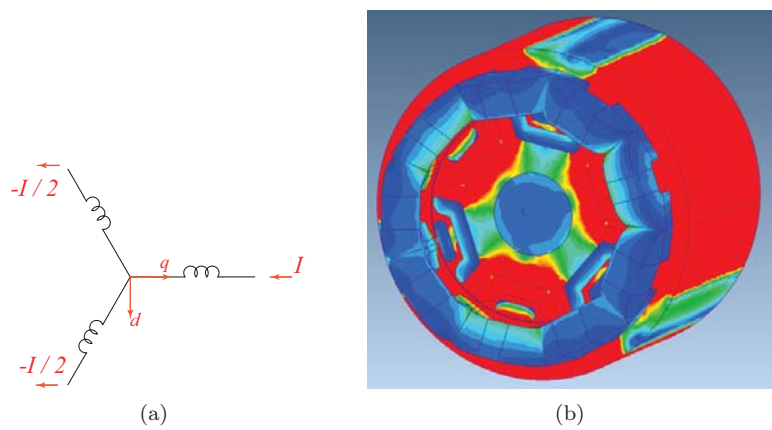FIGURE 7.20: 3D FEA d axis configuration

(a)   (b)

FIGURE 7.21: 3D FEA q axis configuration

TABLE 7.7: Comparison of the 3D effect between the model and the FE results

	3D leakage Inductance μH			
	Model		$\lambda_{3D,FEA} - \lambda_{2D,FEA}$	
$L_{ew} + L_{fr}@I = 50A_{pk}$	d	q	d	q
	215	719	240	800

Comparing the 2D FEA with experiments it is evident a discrepancy on the q-axis, see Figs.7.22. FEA underestimate the q axis inductance. The 3D FEA permits to reduce the difference between the numerical solutions and experiments. This phenomena is related to the border effect of the field in the machine that presents an higher value of the fringing phenomena on the q axis configuration. In Fig. 7.22b it is shown that the 2D FEA overestimate the torque production with an amount of +11%, considering the border effect, the overestimation of torque by 3D FEA is reduced to +4%.
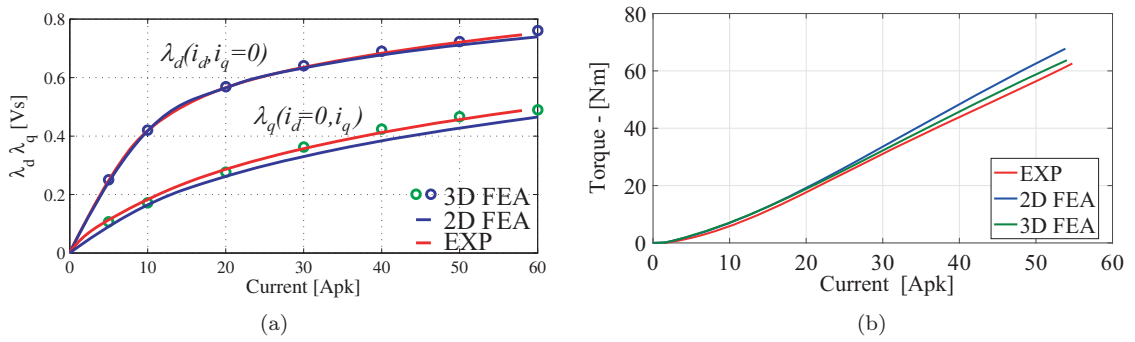
FIGURE 7.22: Comparison between Experimental Results, 2D and 3D FEA; (a) Flux linkage curve, (b) Torque vs current

7.5 Prototype and Experimental Results

As an indication of the level of performance that can be achieved applying FSW to synchronous reluctance motors. A machine according to the design process previously described is prototyped. The electric machine specifications are summarized in Tab.7.8. The machine was designed for pumps applications. The phase RMS voltage is 400V, so it is reasonable consider a DC link of 550V; phase resistance and end winding connections are lower than the distributed motor.

In Fig.7.23 are shown some pictures of the prototype. The manufacturing is close to the designed solution. A main discrepancy is on the slot filling factor, in the design was initially considered a filling factor of 0,6, however finally the filling factor of the prototype is 0,45. A second prototype is built with the designed filling factor but for time reasons, it arrived too late. Torque ripple performances are the same. The efficiency behavior is different and it will be shown in the following for both the filling factor values.

TABLE 7.8: Prototype main electric data

DC link Voltage [V]	550	550
winding factor	0,45	0,44
Phase resistance [Ohm]	0.134	2
End winding length [mm]	45	–

7.5.1 Test Bed Description

The test procedure was divided into three steps, the first one is represented by the magnetic model identification procedure, accurately described in [24], the second step is the efficiency estimation,and

(a)

(b)

(c)

FIGURE 7.23: Foto of FS-SyR prototype

the third step is the torque ripple identification. A brief description of the test procedures are summarized in the following:

1. *Magnetic Model Identification*: The drive machine (DM) shown in Fig 7.24 and in Fig 7.25a, is a 4 pole 15kW @ 9000rpm motor, driven in speed control mode, in order to impose constant speed. The machine under test (MUT) is current controlled, a grid of current values is imposed. Voltages, currents, torque and speed are measured by HBM data-logger (gen3i) [21], and than manipulate like in [24] for estimate fluxes.

2. *Efficiency Test*: The configuration is the same of the Magnetic Model Identification, in this case the MUT machine is torque controlled by Direct Flux Vector and Torque algorithm (DFTC).

3. *Torque ripple identification*: The MUT is shaft connected to a gear box, like in Fig 7.25b, the gear ratio is 1/10, the motors rotate at 10rpm and waveforms are sampled at 2MSamples/second. The measured torque oscillation represents the torque ripple of the synchronous motor.

In both cases the MUT is driven by a IGBT three phase inverter controlled by dSpace board 1103.
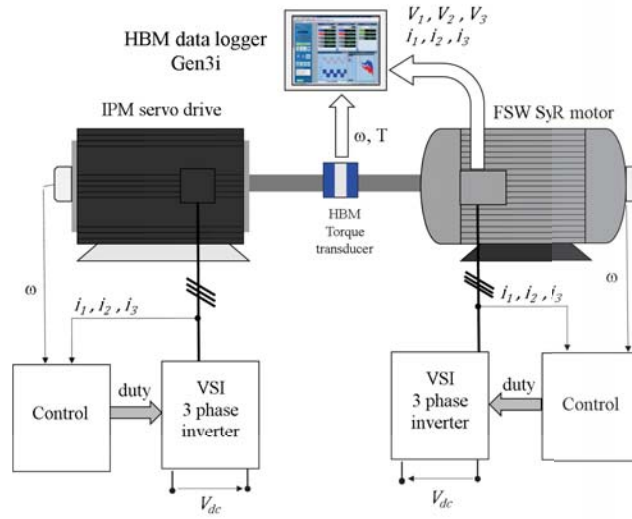
FIGURE 7.24: Test bed setup

| (a) | (b) |
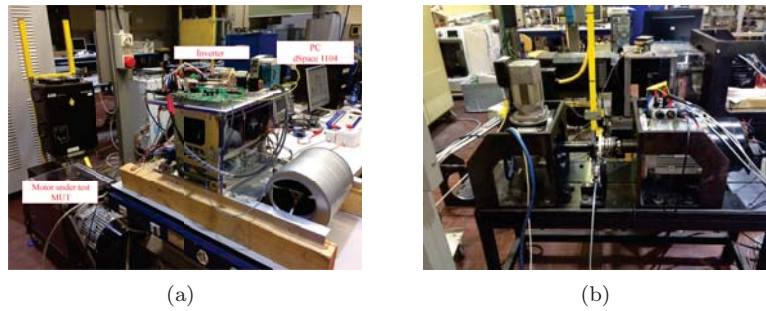
FIGURE 7.25: a) Photo of test bed for magnetic model identification; b)Test bed for torque ripple identification

7.5.2 Torque Ripple profile

The torque ripple profile is shown in Fig.7.26, a minimum of the torque ripple exist along the MTPA. FEA and empirical results presents a good match. The ISO-ripple line in Fig.7.26c,d presents a quite flat behavior with a peak to peak ripple around 20Nm at lower current angle. Reduction of the d-axis component and increment of q-axis current leads to higher increment in torque ripple. This effect is evidenced in Fig 7.27, that shows the torque profile for the three points: A,B,C (see Fig 7.26c).

(a)

(b)

(c)

(d)
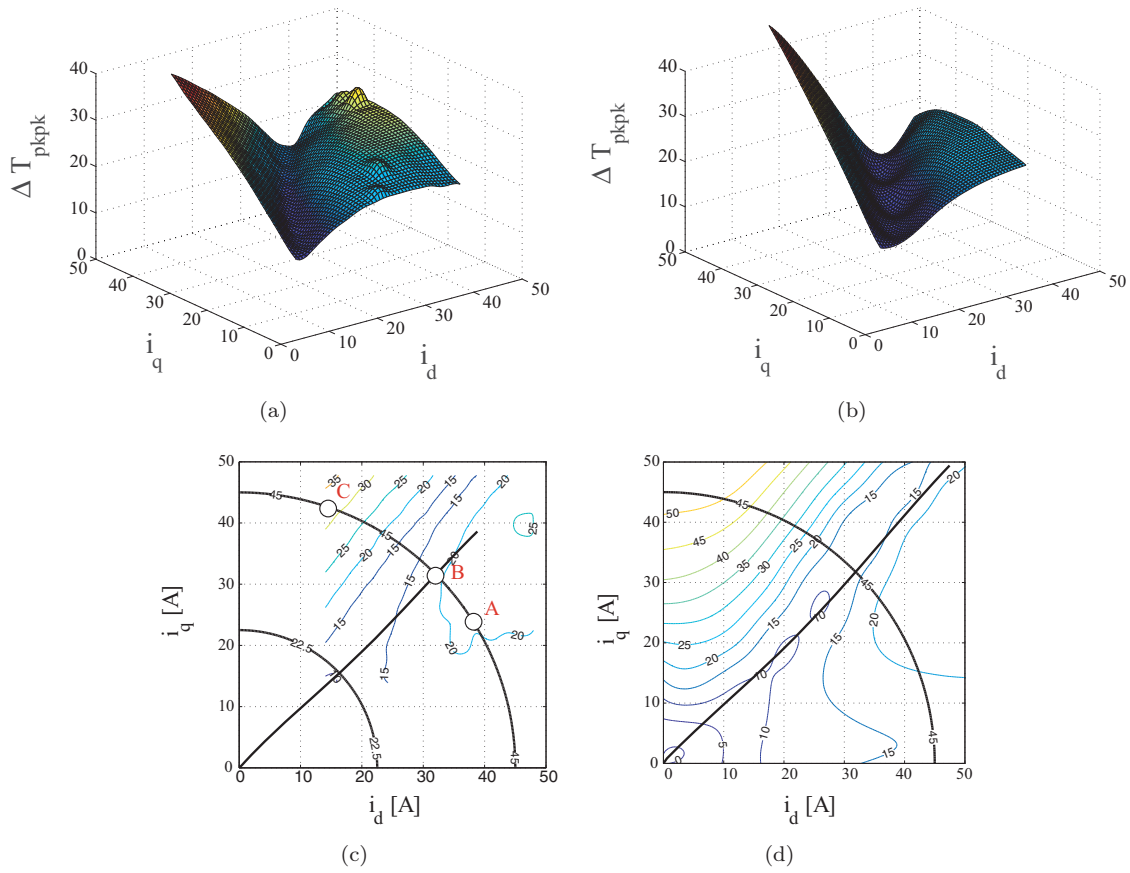
FIGURE 7.26: Torque ripple surface and contour in $i_d\,i_q$ reference frame; (a) Experimental torque ripple surface (b) FEA torque ripple surface; (c) Experimental torque ripple contour; (d) FEA torque ripple contour

(a)

(b)

(c)
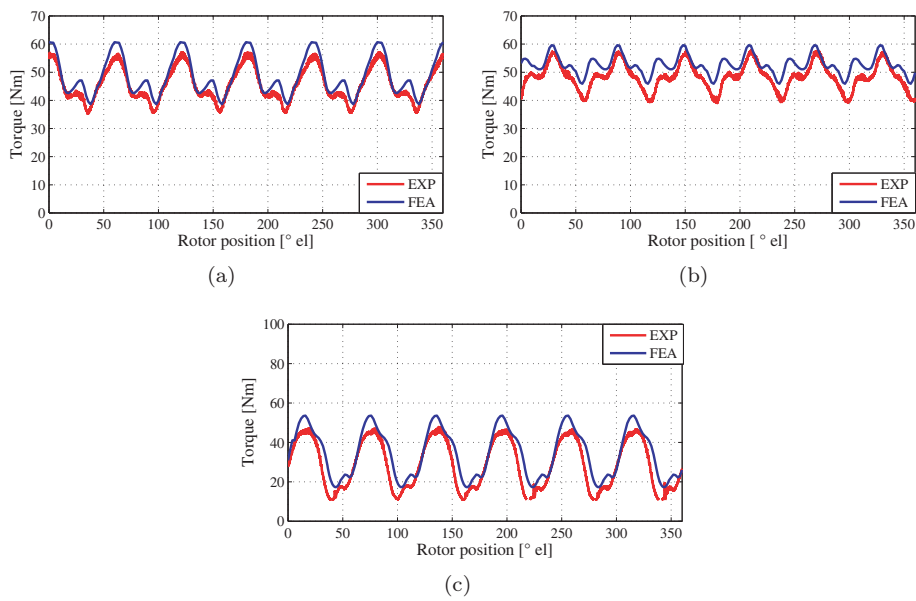
FIGURE 7.27: Torque ripple, a) 45A 35°el, b)a) 45A 45°el, a) 45A 65°el

Another representation of the torque ripple is shown in Fig 7.28.With this charts are evident that at higher current angle the ripple increases. On the other hand, current angle over $60°\,el$ does not represent a real working point, for this machines. This is related to the lower anisotropy of this motor and to the fact that they do not present a constant power profile, because are designed for pump applications. A minimum of the torque ripple in the FEA results is obtained at the maximum torque (along the MTPA). Experimental results confirm this trend, showing that the minimum of torque ripple is close to the maximum of torque.


(a)

(b)

(c)
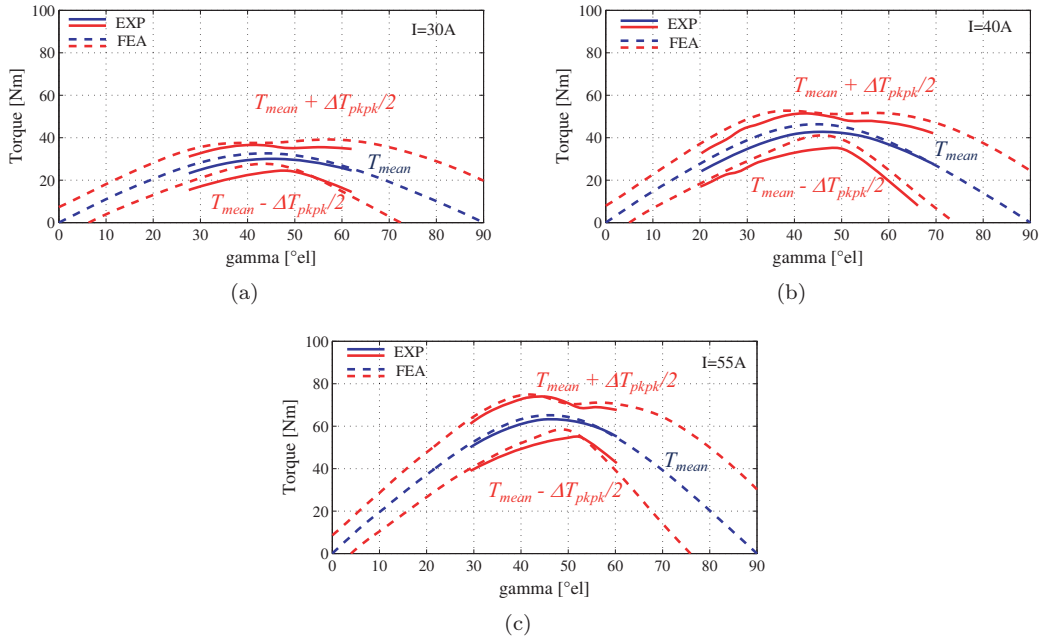
FIGURE 7.28: Mean torque and torque ripple at imposed current value, varying the current angle $i_d\,i_q$ reference frame

7.5.3 Efficiency Results

The efficiency calculation is realized according to the procedure described in Chapter 4. After the magnetic model identification a DFTC control strategy was implemented on the machine under test and using the test bed previously described are measured the mechanical data at the shaft and the electric quantity absorbed by the machine.

Efficiency result is illustrated in Fig 7.29. The experimental points are the black dots. In blue are shown the FEA results with the correction of the 3D effect illustrated in the previous chapter, green line represents the IE4 target. It is possible to see that at lower load, the IE4 target is reached. The efficiency results are always bigger than the induction motor [22]. The application of this machine as explained in the first part of the Chapter is for pumps and funs. Recent studies in the industrial applications [22] have shown that mots of the working hours of an electric motors in pump applications are not at the rated power, see Fig.7.29. Machines work for 44% of their life at 25% of rated power and only for 6% at the rated ones. Considering this distribution it is possible to say that the machine under test works in IE4 for the most part of its working life.

the comparison between the distributed winding benchmark and the prototyped fractional slot motor is summarized in Tab.7.9. The efficiency is slightly smaller. However much bigger is the difference in power factor, this lower power factor negatively impacts on the electric drives sizing and its costs.

TABLE 7.9: Motor performance comparison

FIGURE 7.29: Efficiency vs output Power at constant speed @ 1500rpm

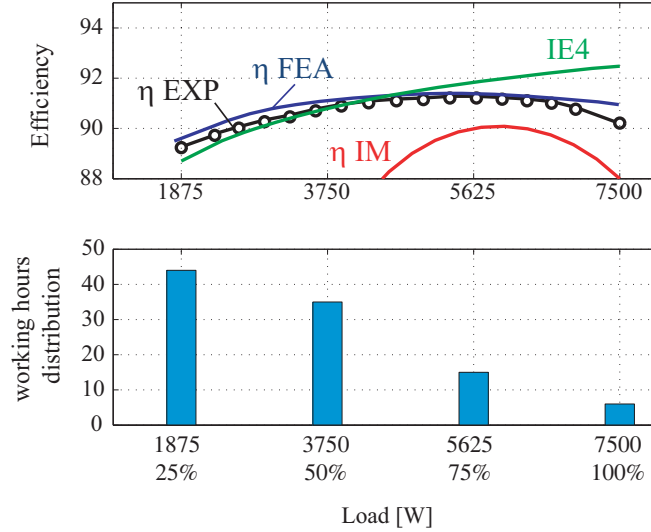|	Dist-SyR	FS-SyR
Voltage	100%	100%
Current	100%	162%
P_{shaft} [W]	7500	7500
PF	0,727	0,45
Copper θ	$65\,^{\circ}C$	$100\,^{\circ}C$
η	0,95	0,90

7.5.4   Increased fill factor

In the prototype motor a slot fill factor of 45% was achieved. It is possible to increase the fill factor with modular stator construction, by this way the fill factor could be increased up to 0,6. The improvement in the fill factor would produce benefits in terms of stator resistance, steady state temperature and consequently Joule losses reduction. With benefit on efficiency. Tab.7.10 shows that the stator resistance reduction is in proportion to the filling factor increment. Efficiency reach value of 0,92, close to the IE4 target. The estimated winding temperature for the solution with $k_w = 0,6$ it is evaluated with MotorSolve thermal solver (Infolytica program). The value referred to $k_w = 0,45$ it is the experimentally calculated. Fig.7.30 illustrates that comparing $q = 3$ and q=1/2 with close fill factor even with the lower end winding length.

Fractional Slot solution presents higher copper quantity respect to the distributed one. In Fig.7.30 it is the lower iron quantity that reduce the costs. FS-SyR with $k_w = 0,45$ is 8,6% cheaper than $q = 3$ motor with a power density per cost of 129W/\$ respect to a value of 121W/\$ for q=3 motor. Increasing the fill factor from 0,45 to 0,6 the copper cost push the total costs up to 72\$, with a power density of 104W/\$.

TABLE 7.10: Increased Fill Factor

Fill Factor	Copper Mass [kg]	$R_s\,22°C$	θ_w	η %	$P_{shaft}[W]$
0,45	6,65	0,134	100	0,9	7500
0,6	9,27	0,103	83	0,92	7500

Results show that FS-SyR motor are capable of higher power density per cost respect to the distributed winding solutions, even if with lower efficiency. The increment of the filling factor on one side, increases the efficiency, leading to efficiency close to the IE4 target, but on the other side increases the costs of the motor, overcoming the cost of a distributed machine.
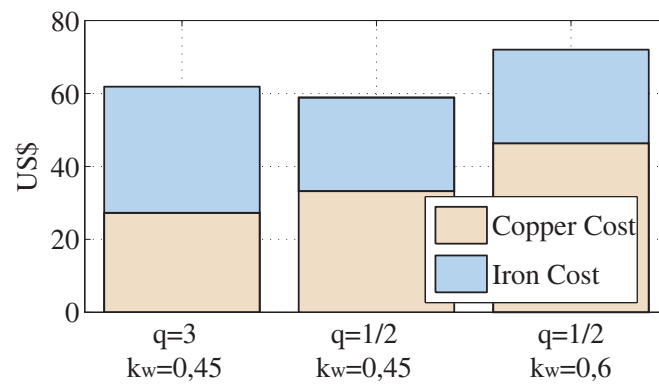
FIGURE 7.30: Cost comparison between a) q=3 distributed winding; b) FS-SyR with filling factor 0,45; c) FS-SyR with filling factor 0,6

Chapter 8

SyR Designs with Non Conventional Fractional Slot per Pole Combination

8.1 Mild Overlapped overview

Fractional-slot concentrated-winding permanent magnet (PM) machines are appreciated for their ease of manufacturing and short end connections. Modular construction can increase the slot filling factor resulting in very high torque density [51]. Different slot-versus-pole combinations and rotor configurations have been investigated and commercially applied [46], with rotors of the surface-mounted PM (SPM) or interior PM (IPM) [52] types. With fractional slots the armature flux linkage can be calibrated by design to match the PM flux linkage and obtain an infinite constant power speed range [53]. However, it has also been noticed that salient IPM rotors associated to fractional slot windings do not retain the expected reluctance torque contribution [54]. Thus, it is very rare in the literature that the Synchronous Reluctance (SyR) and the PM-assisted SyR (PM-SyR) machines have been realized with fractional-slot windings, because of such reluctance-killing effect of fractional slot configurations. The combination q = 0.5 is the only exception, being q the number of slots per pole per phase, which maintains saliency ratios sufficient for application to PM-SyR machines [55]. This chapter presents a new PM-SyR machine with a nonconventional 24 slot/10 pole fractional configuration. This machines as shown in Fig.8.1 represent the overlapped and mild -overlapped solution. The number of slots per pole per phase is lower than one, but the end turns cross more than one slots. The 24/10 combination (q = 4/5) was recently proposed for SPM motors application [56]. It is derived from the popular 12 slot/10 pole combination (q = 2/5), aiming at reducing the harmonic content of the magneto-motive force (MMF) distribution. The 12/10 combination was chosen in [56] and here as the starting point because it is very popular in the literature, but similar transformations apply to other concentrated-winding configurations. The proof of principle presented here shows that the 24/10 PM-SyR machine preserves the most of the reluctance torque of the salient rotor, opening the stage to a new class of FS-SyR and FS-PM-SyR solutions. In turn, the 24/10 PM-SyR machine retains most of the ease of manufacturing of fractional slots together with the advantages of PM-SyR rotor topologies, such as PM cost reduction, uncontrolled generator voltage reduction [57], higher power overload [57], [58]. Three PM-SyR machines are compared, all having the same 10-poles rotor and the same stack outer dimensions. The first machine has 90 stator slots and standard distributed windings (q = 3). The second one has 12 slots with 12 tooth-wound coils (q = 2/5, double side), and the third machine is the new one, with a double layer winding housed in 24 slots and the end turns mildly overlapping (q = 4/5).
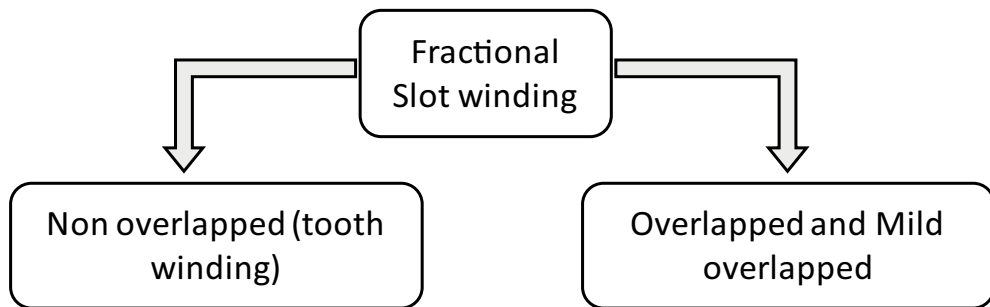

FIGURE 8.1: different category of Fractional Slot Winding

8.2   Armature Reaction MMF Analysis

The MMF distribution of the 12 slots 10 poles winding is determined in a simple way using some rules and relation of Fourier transformation for periodic signal. For simplifying the mathematical elaboration, the MMF is set in a even periodicity respect to y-axis, as reported in Fig 8.2a. Than it is possible to express the Fourier series with only $cos(f(x))$ terms. In Fig 8.2b is reported the conductors density distribution, see (8.1).

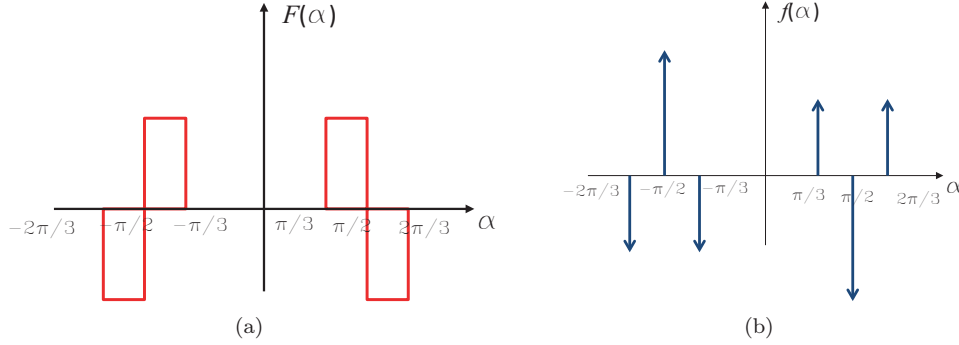$$F(\alpha) = \int \cos(\alpha)d\alpha \tag{8.1}$$

FIGURE 8.2: a) MMF distribution of 12slots 10 poles, b) conductor density distribution function

It is possible to determine the Fourier series passing from the conductors density distribution. Using the rules of the Fourier transform (8.2).

$$j\omega F_0 = \delta\left(\alpha + \frac{2\pi}{3}\right) + 2\delta\left(\alpha + \frac{\pi}{2}\right) - \delta\left(\alpha + \frac{1\pi}{3}\right) + \delta\left(\alpha - \frac{\pi}{3}\right) - 2\delta\left(\alpha - \frac{\pi}{2}\right) + \delta\left(\alpha - \frac{2\pi}{3}\right) \tag{8.2}$$

The Fourier transform of delta Dirac is

$$\delta(\alpha - k\,2\pi) \longrightarrow e^{-jk\,2\pi\,\omega} \tag{8.3}$$

Where $\omega = v\omega_0$; $\omega_0 = 1$. Using formula (8.3) and substituing it into (8.2) it results:

$$F_0 = \frac{1}{v}\left[-2\sin(v\frac{2\pi}{3}) + 4\sin(v\frac{\pi}{2}) - 2\sin(v\frac{\pi}{3})\right] \tag{8.4}$$

The coefficient of the Fourier Transform is $H_v = \omega_0\,F_0$ where $\omega_0 = 1$. Next, the relation between the coefficient of the Fourier transform and the Fourier series is $C_v = H_v/2\pi$. The Fourier coefficient results:

$$C_v = \frac{1}{\pi\,v}\left[-sin\left(v\frac{2\pi}{3}\right) + 2sin\left(v\frac{\pi}{2}\right) - sin\left(v\frac{\pi}{3}\right)\right] \tag{8.5}$$

The value under square parenthesis is the vector sum of EMF of half winding. Using the function $sin()$ is possible to take into account the spatial position of the corresponding EMF phasors. Considering that the elementary block of 1 phase per pole is composed by four emf vectors, the corresponding winding factor of q=2/5 is evaluated in (8.6).

$$k_w(v) = \frac{1}{4}\left[-sin\left(v\frac{2\pi}{3}\right) + 2sin\left(v\frac{\pi}{2}\right) - sin\left(v\frac{\pi}{3}\right)\right] \tag{8.6}$$

With trigonometric formulation it is also possible to express the winding factor in the following manner:

$$k_w(v) = \frac{1}{4}\left[-sin\left(v\frac{2\pi}{3}\right) + 2sin\left(v\frac{\pi}{2}\right) - sin\left(v\frac{\pi}{3}\right)\right] = sin\left(v\frac{\pi}{2}\right)sin^2\left(v\frac{\pi}{12}\right) \tag{8.7}$$

From the resolution of the harmonic orders of (8.7) to zero, it is possible to find that only odd harmonics exist. Finally the MMF of q=2/5 can be expressed by:

$$MMF_{2/5} = \sum_v \frac{8}{\pi v} K_w(v) Z_q I \cos(v\alpha) \tag{8.8}$$

where Z_q is the number of conductors in slot per winding layer (es: in this case there are 2 layers), I is the peak value of the phase current, v is the harmonic order. The three phase MMF can be expressed by

$$MMF = \sum_v \frac{3}{2}\left(\frac{8}{\pi v} K_w(v) Z_q I\right) \cos(v\alpha - \omega t - \gamma) \tag{8.9}$$

The number of conductors in slot can be expressed as $Z_q = N_s/pqa$ where N_s is the number of turns in series per phase, q is the number of slots per pole per phase, p the pole pairs, a the number of slot layer. Than (8.9) becomes:

$$MMF = \sum_v \frac{3}{2}\left(\frac{8}{\pi v} K_w(v) \frac{N_s}{pqa} I\right) \cos(v\alpha - \omega t - \gamma) \tag{8.10}$$

In the specific case of $q = 2/5$ it is possible to write the MMF distribution:

$$MMF_{q=2/5} = \sum_v \frac{3}{2}\left(\frac{4}{\pi v} K_w(v) \frac{N_s}{a} I\right) \cos(v\alpha - \omega t - \gamma) \tag{8.11}$$

Considering forward and backward harmonics, (8.11) can be written as in (8.12).

$$MMF_{q=2/5} = \frac{3}{2}\frac{4}{\pi v}\left[\sum_{v\neq 3+4k v\neq 3,6,9} K_w(v)\frac{N_s}{a}I \cos(v\alpha-\omega t-\gamma) + \sum_{v=3+4k v\neq 3,6,9} K_w(v)\frac{N_s}{a}I \cos(v\alpha+\omega t+\gamma)\right] \tag{8.12}$$

8.2.1   Mild overlapped solution

The mild hybrid solution [56] is obtained doubling the number of stator slots and placing into the slots two equal winding configurations properly translated between each others. In the following it will be described the case of 10 poles 12 slots motors. The winding is duplicated and the two half windings are phase-shifted by 2.5 slot pitches and then connected in series [56]. The phase shift of 2.5 pitches is chosen for the compensation of the 7-th harmonic. To make the half pitch displacement possible the slots are doubled and become 24. Than in the final configuration of 24 slots phase shift is 5 pitches. The process is graphically described in Fig.8.3. The 24 slots/10 pole machine has q = 4/5. It is still a fractional slot/pole combination, but its end turns are mildly overlapped. The MMF spectrum of the q = 4/5 winding is reported in Fig.8.5. The 7-th order is practically canceled, along with orders 17, 31 and 41. Also the 1st order sub-harmonic is partially attenuated. Plus, the 24 slots stator has much smaller slot openings, and this enforces the d-axis flux linkage and increases the reluctance torque capability.

The mathematical formulation for the results shown in Fig 8.3 is exhibits in (8.13)

$$MMF_{24s} = MMF_{12s}(v\alpha - \omega t - \gamma) + MMF_{12s}(v\alpha - \alpha_{trasl} - \omega t - \gamma) \tag{8.13}$$

Expanding (8.13) and using the Prosthaphaeresis Formulas:

$$MMF_{24s} = \sum_v \frac{3}{2}\left(\frac{16}{\pi v} Z_q I\right) K_w(v) \cos(v\frac{\alpha_{trasl}}{2}) \cos(v\alpha - \alpha_{trasl}/2 - \omega t - \gamma) \tag{8.14}$$

Finally considering the forward and backward harmonics:

FIGURE 8.3: Construction of the 24 slots windings starting form two 12-slot windings.

$$MMF_{24s} = \frac{3}{2}\frac{4}{\pi v} K_w(v) \cos\left(v\frac{\alpha_{trasl}}{2}\right)\left[\sum_{v\neq 3+4k v\neq 3,6,9} \frac{N_s}{a} I \cos(v\left(\frac{\alpha - \alpha_{trasl}}{2}\right) - \omega t - \gamma) + \right.$$
$$\left. + \sum_{v=3+4k v\neq 3,6,9} \frac{N_s}{a} I \cos(v\left(\frac{\alpha - \alpha_{trasl}}{2}\right) + \omega t + \gamma)\right] \tag{8.15}$$

The new winding solution is shown in (8.14). The winding factor can be expressed in (8.16) in function of the number of slots of translation, $\alpha_{trasl} = n_{slot}\frac{\pi}{Q}$. Where n_{slot} is the number of slots of translation, Q is the total number of slots on the stator, v is the harmonic order of the MMF spectrum.

$$K'_w(v) = K_w(v) \cos\left(v\frac{\alpha_{trasl}}{2}\right) = K_w(v) \cos\left(vn_{slot}\frac{\pi}{Q}\right) \tag{8.16}$$
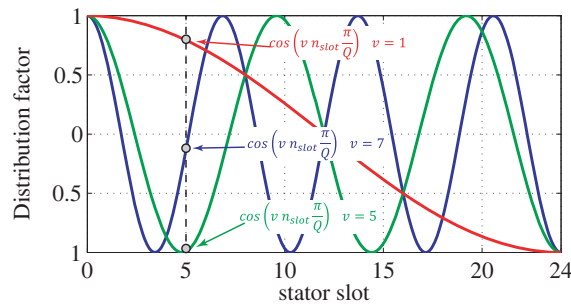
FIGURE 8.4: Distribution factor of Q=24 slots

The MMF spectrum of the q = 4/5 is reported in Fig. 8.5. The 7-th order is practically canceled, along with orders 17, 31 and 41. Also the 1st order sub-harmonic is partially attenuated. The 24 slots stator has much smaller slot openings, and this enforces the d-axis flux linkage and increases the reluctance torque capability.

8.3   Performance of 10 poles solution

The cross sections of the three machines are reported in Fig. 8.6. The green colored barriers account for the presence of the PM material. The PMs fill the rotor saliency completely, as if plastic bonded
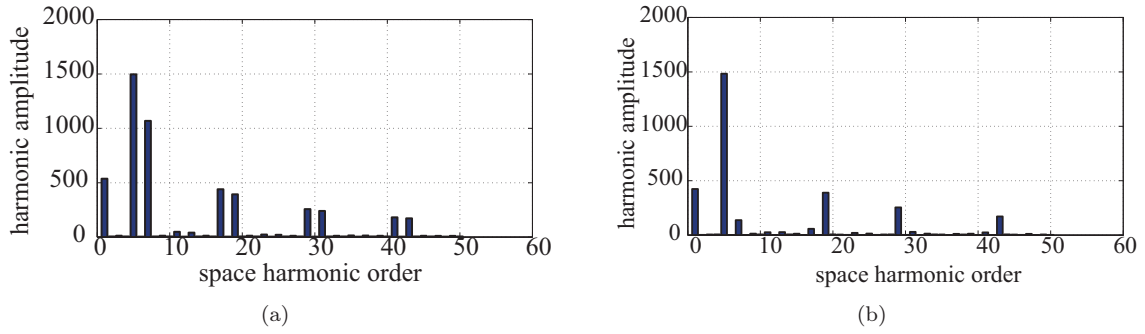
FIGURE 8.5: MMF spectrum of the a) q = 2/5 machine and the b) q = 4/5 windings at 120 Apk

magnets were used, but this is not necessarily the case in reality. The main data of the three machines are reported in Tab 8.1. At first, it is analyzed the reluctance torque performance, with no magnets in the rotors, to put in evidence the reluctance bases of the three configurations. Secondly, the PMs are inserted and the performance of the final PM-assisted machines is assessed and compared via finite element analysis (FEA) computation. As the reluctance effect is different for the three machines, also the PM quantity will be different for the three rotors, as will be commented. In this section, the machines are FEA simulated with no magnets in the rotors in order to segregate the reluctance torque and the armature dq flux linkages. The common 3-layer rotor was chosen for its good match with the q = 3 stator [4], but the conclusions of the analysis are valid also for other number of layers. The same current level (120 Apk) and the same number of turns in series per phase are used in this section for the three SyR machines. It must be considered that the q = 3 machine has a higher winding factor (kw = 0.96 versus 0.933 and 0.925), and that conversely the q = 2/5 machine has the shortest end turns. This to say that with the same current the q = 3 has a higher fundamental MMF, but the q = 2/5 recovers in terms of lower Joule losses. The results presented in this section show a first clear trend in terms of reluctance torque.
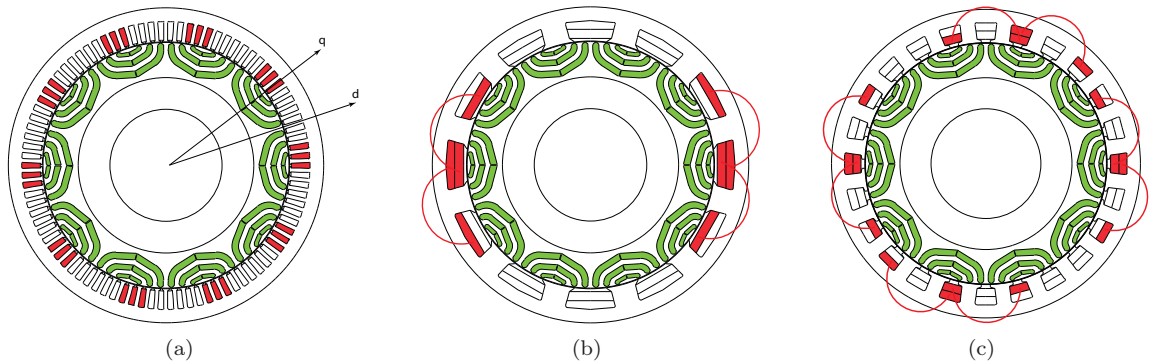

FIGURE 8.6: Cross sections of the three PM-SyR machines under analysis: a) q=3, distributed windings; b) q=2/5, concentrated windings; c) proposed q=4/5 solution, with mildly overlapping windings. The red areas in the slots indicate one phase. The end turns are also evidenced.

TABLE 8.1: Main Figures of the three machines under comparison

Slots/pole/phase	3	2/5	4/5
number of phases		3	
Stator slots	90	12	24
Pole pairs		5	
Turns in series per phase		70	
Outer diameter		380	
Stack Length		280	
Airgap		0.75	
Slot filling factor		0.4	
End winding length	0.117	0.100	0.114
Phase resistance @ $130°C$	0.151	0.081	0.135
End winding resistance	0.0393	0.0205	0.0354

8.4 Synchronous reluctance Performance

In this section will be illustrated the comparison between the three machines in terms of reluctance performances, attention will be given to the torque density, torque ripple profile and power factor. As will be seen the Mild overlapped solution is a reluctance saving solution, the reduction of the harmonic content in the MMF permits to improve the performance of the machines.

8.4.1 Reluctance torque

At first, the benchmark q = 3 motor and the concentrated windings configuration q = 2/5 are considered. The SyR rotor is designed according to the state of the art: the reluctance torque is maximized by the alternation of air barriers and steel segment widths. The barrier ends are regularly displaced at the airgap, for torque ripple minimization. The rotor pitch was optimized for the q = 3 stator.
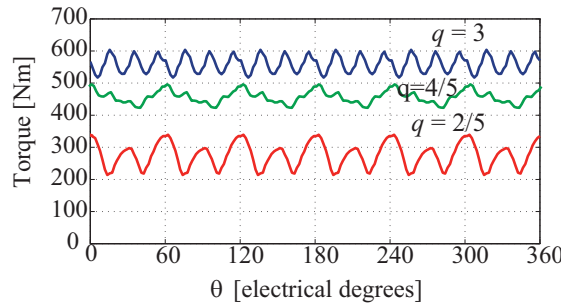

FIGURE 8.7: Torque waveforms of the q = 3 q = 2/5 and q=4/5 machines at same current (120 Apk), over one electric period.

The torque waveforms at 120 Apk are reported in Fig.8.7 for the three machines. The respective maximum torque per Ampere (MTPA) conditions were considered, FEA evaluated. The average torque values are 560 Nm for q=3 and 275 Nm (49 %) for q=2/5. The peak to peak ripples are 80 Nm and 110 Nm (138%), respectively for the q = 3 and 2/5 machines. The torque ripple of the q = 3 has 18 cycles per electrical period, from the stator slots periodicity. The main torque ripple harmonics of the q = 2/5 case are the 6th and the 12th orders, referred to one electrical period. The 12th order comes from the lowest common multiple of slots and poles, whereas the 6th order is expected when a salient rotor associated to this slot/pole combination [52]. The rotor was not specifically designed for the q = 2/5 stator, so the ripple could be mitigated with specific countermeasures [59]. However, the result of this section is the drastic difference in terms of average torque, that impacts the performances of the final PM-assisted machines. The reluctance torque waveform of the q = 4/5 machine is also compared with the q = 3 and q=2/5 machines, see (Fig.8.7). The average torque is 457 Nm which is 82% of the q = 3 benchmark, and 169% of the 270 Nm output by the q = 2/5 machine. The reluctance torque increase is encouraging. The peak to peak torque ripple amplitude is comparable to the q = 3 one, and its main component is the 6th harmonic in the electrical domain, 30th in the mechanical domain.

8.4.2 Flux linkage curves

The dq flux linkage curves of the two machines are represented in Figs.8.8. The q = 2/5 curves show lower values of d-flux linkage and higher values of q-flux linkage and a more evident cross-saturation. The dq reference frame is defined in Fig. 8.6a according to the SyR machine conventions, and will be used also for the PM-assisted machines. The comparison of Figs. 8.8a,b gives important insights on the worse torque performance of the fractional slot machine. Respect to the distributed windings machine (Fig. 8.9a), the fractional slot machine has a lower d-axis and a higher q-axis flux linkage components (Fig. 8.9b). Both factors lower the output torque. The flux linkage amplitude λ_{SyR} is in fact smaller than the one of the benchmark machine λ_{SyR}, from the smaller d-component. The increase of the q- flux linkage component increases the flux phase angle δ' with respect to δ, thus reducing the PF and then, again, the torque, see Fig.8.9.
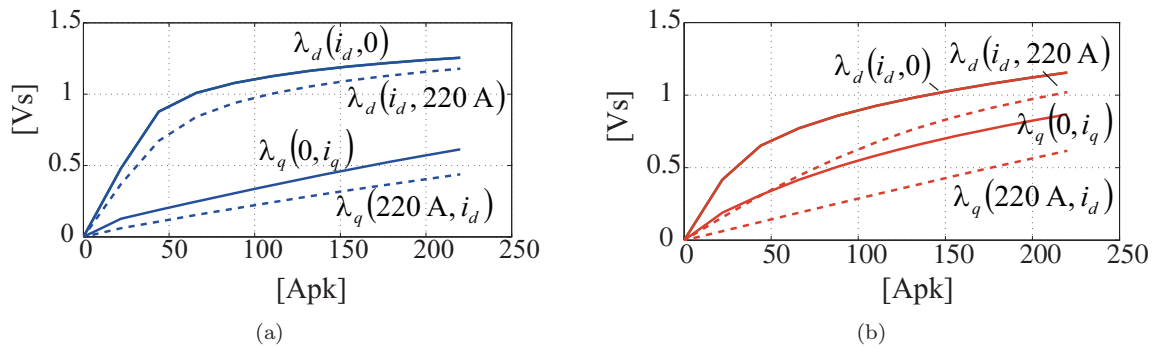

FIGURE 8.8: a) dq flux linkage curves of the q = 3 motor, b) dq flux linkage curves of the q = 2/5 motor.
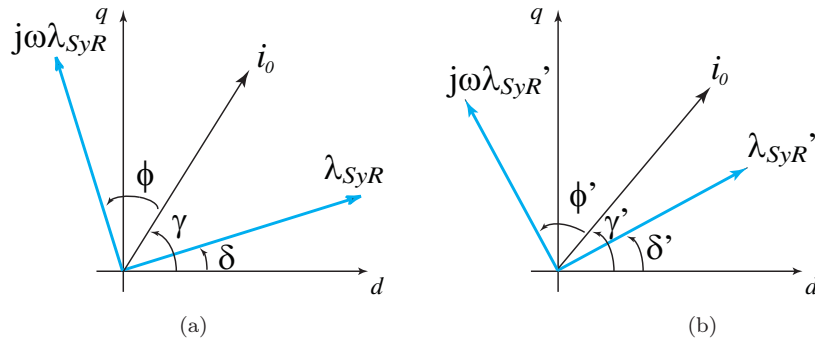

FIGURE 8.9: Steady-state dq vector diagram. a) q = 3 machine; b) q = 2/5 machine, with reduced d- and augmented q- flux linkages.

The lower d-axis flux linkage is to a minor extent related to the lower winding factor and primarily to the large slot openings of the 12-slot stator. If the slots were fictitiously made very narrow and with the same slot currents in, the d-flux linkage values of the q = 2/5 machine would become very close to the ones of the q = 3 machine, at least at zero i_q. Of course this is not feasible in practice because of the thermal constraints. The large q-axis flux linkage of the q = 2/5 machine is a direct consequence of the fractional slot/poles combination, that vanishes the magnetic insulation effect of the multi-barrier rotor. When the phase currents are supplied according to the q-axis only, yet some rotor poles are offset from the insulation situation and subjected to MMF values that drive non-negligible flux through their flux guides. In other words, while the fundamental MMF component is synchronous to the rotor and then correctly aligned with the rotor q-axis at all times, all non-synchronous MMF harmonics leak flux through the high-permeance flux guides. The insulation potential of the multi-barrier rotor is practically neutralized. The flux leakage situation is exemplified in Fig. 8.10, where a q-axis only MMF is applied to the q = 2/5 machine. Poles 1 and 5 face the maximum MMF values and guarantee a good insulation, whereas poles 2 and 4 let the flux stream through their flux guides. Pole 3 is not subjected to MMF. As for the average torque, the behavior of the flux linkages is intermediate

between the q = 3 and q = 2/5 situations, but promisingly closer to the former one. The d-axis flux linkage can reach the same levels of the distributed winding solution, but with a greater cross saturation effect that imposes larger i_d values to recover from the i_q related loss of excitation (d-axis) flux. The q-axis flux linkage is worse than in the q = 3 case and only slightly better than in the q = 2/5 case as shown in Tab.8.2.
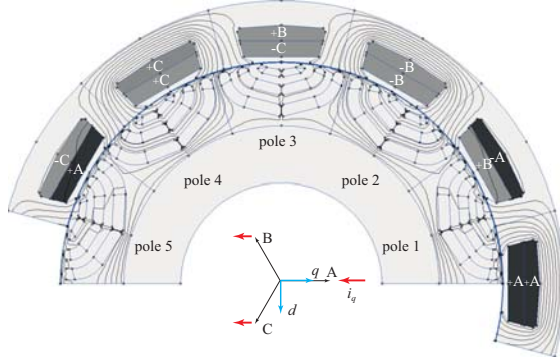
FIGURE 8.10: Field contour lines when q-axis mmf only is applied to 2/5 machine

TABLE 8.2: SyR performance of the machines under test

Slots/pole/phase	3	2/5	4/5
Current Amplitude		120	
Current phase angle	58	50	55
Test speed		500	
d-axis flux linkage (λ_d)	0.9	0.72	0.87
q-axis flux linkage (λ_q)	0.28	0.39	0.36
Torque	560	275	457
Line to line voltage	441	379	438
Power Factor	0.68	0.40	0.57

The dq flux linkage curves of the 24/10 SyR machine are illustrated in Fig.8.11. As for the average torque, the behavior of the flux linkages is intermediate between the q = 3 and q = 2/5, but promisingly closer to the former one. The d-axis flux linkage can reach the same levels of the distributed winding solution, but with a greater cross saturation effect that imposes larger i_d values to recover from the i_q related loss of excitation (d-axis) flux. The q-axis flux linkage is worse than in the q = 3 case and only slightly better than in the q = 2/5 case.
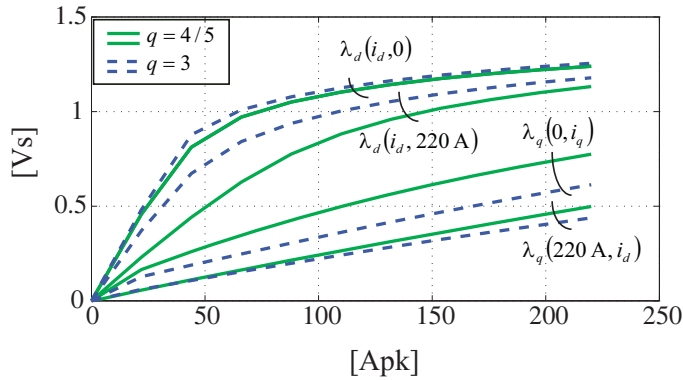

FIGURE 8.11: dq flux linkage curves of the q = 4/5 motor and q = 3 benchmark.
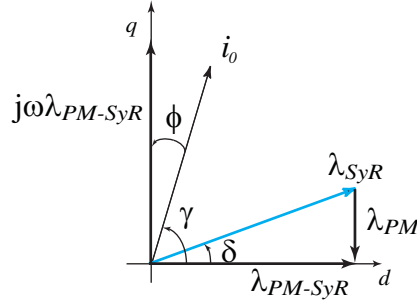
FIGURE 8.12: Vector diagram of the PM-SyR motor in natural compensation condition.

8.5 Permanent Magnet SyR performance

The PMs are designed in natural compensation condition. The PM quantity and grade are chosen so that the PM flux linkage ideally compensates the q-axis component of the armature flux linkage at rated current. The SyR style dq axes are adopted, as shown in Fig.8.6a. For the sake of modelling simplicity the flux barriers are filled with a plastic bonded PM material, whose remanence can be decided on a continuous basis by the designer. The remanence of the PM material is then a single design input able to trim the grade of PM assistance readily and with precision. The machines under investigation will require low values of such equivalent remanence (e.g. Br = 0.18 T, 0.25 T). When dealing with the fabrication of real machines with commercial magnets (e.g. Br = 0.36 T) the PM volumes will be reduced in inverse proportion to the increase of B_r, and machines with identical output figures will be obtained. In a way, the fictitious Br used here for the design is also a useful indicator of the PM "equivalent quantity" needed in the three cases. The principle of natural compensation is shown in Fig. 8.12. Given the vector diagram of the initial SyR motor, the PMs are set for having zero flux linkage on the q-axis at rated current, in MTPA conditions. The process requires a couple of iterations before the exact torque value is associated to the zero q- flux linkage situation. The PM remanence is first evaluated by analytical formulas and then finalized with FEA simulation, for the three machines. The values of the equivalent Br are reported in Tab. 8.3. In Fig. 8.13 the current vectors of the just designed PM-SyR machines are shown in the (i_d, i_q) current plane, each one in the respective MTPA conditions. The q = 3 and q = 4/5 cases have similar amplitudes (112 A and 121 A), whereas the q = 2/5 machine needs 158 A for its worse reluctance properties. Tab. 8.3 reports the d- and q- flux linkages figures for rated operating conditions. The q- flux linkage is close to zero by definition of natural compensation. The d- flux linkage values of the q = 3 and q = 4/5 designs are close to each other (0.954 Vs and 0.946 Vs, respectively) at the expense of a higher d-axis current for the q = 4/5 (80 A versus 62.4 A).Despite the high i_d current (120 A), the q = 2/5 machine does not reach the same d- flux linkage value of the two competitors (λ_d = 0.877 Vs). A consequence of the smaller d- flux linkage is that also the q-current component must be increased, to get to the torque target. The result is that the current amplitude is a significant 158 A. Again, the penalty in terms of Nm per Ampere of this q = 2/5 PM-SyR machine comes from the low reluctance torque

TABLE 8.3: PM-SyR performance of the machines under test

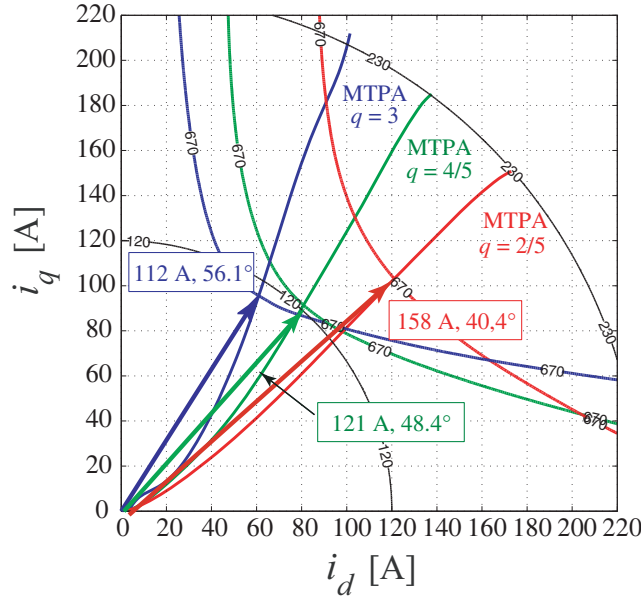| Slots/pole/phase	3	2/5	4/5
PM remanence [T]	0,18	0,25	0,25
Slots/pole/phase	112	92	107
Rated torque and speed conditions			
Corner speed [rpm]	465	500	465
Torque [Nm]	670	670	670
Current Amplitude [A_{pk}]	112	158	121
Current phase angle γ [deg]	56.1	40.38	48.4
d-axis flux linkage (λ_d)	0.954	0.877	0.946
q-axis flux linkage (λ_q)	0.011	0.0088	-0.037
DC-link Voltage [V]		400	
Power Factor	0.941	0.91	0.935

FIGURE 8.13: Current vectors of the three PM-SyR machines for the same output torque of 670 Nm. The respective MTPA curves are reported.

All the machines have 70 turns in series (Tab.8.1), and this is why the q = 2/5 ones has a slightly higher corner speed of 500 rpm versus the 465 rpm of the other two. If the former was rewound with 76 turns to have a corner speed of 461 rpm the current amplitude mismatch of Fig. 8.13 would be mitigated (146 Apk instead of 158 A, for 670 Nm). The rated torque waveforms are reported in Fig. 8.14 for the three machines, recalling the SyR ones of Figs. 8.7 and 8.11b in terms of torque ripple. The q = 3 and 4/5 machines have acceptable peak to peak ripple values, whereas the q = 2/5 one shows a very large ripple. As said, a specific rotor optimization could mitigate the problem. Yet, the proposed q = 4/5 solution is very competitive in this sense with no need for specific countermeasures, due to its improved MMF harmonic content and higher number of slots, with respect to the q = 2/5 case.

8.5.1   Power versus Speed curve

The power versus speed curves at constant current amplitude and limited inverter voltage are reported for the three PM-SyR machines in Figs.8.15. The order of the figures is q = 3, q = 2/5 and q = 4/5. Each figure reports two power curves: one referring to the rated torque current (different for the three) and the second one referring to a common maximum value of 200 A (pk). All the power curves refer to a 400V dc-link. The rated torque and corner speed condition is indicated as point A. The maximum power at maximum speed is indicated as point B, and it is different for the three. The power curves of the benchmark q = 3 and the proposed q = 4/5 machines are fairly close to each other. The maximum output power is 35 kW for the former and 30.5 kW for the latter. The maximum power conditions are 58 kW @ 500 rpm and 53 kW @ 500 rpm, respectively. According to the literature, flat power versus speed curves at constant current and limited voltage are facilitated by the presence of saliency, and vice-versa, and machines with more saliency have a higher power overload capability, with the same inverter limits [58]. The results of Fig.8.15 are consistent with the literature in both senses, as the q = 3 machine is the one with the best SyR characteristics, followed by the q = 4/5 and, last, the q = 2/5 machine.

8.5.2   Flux linkage comparison of the 24 and 12 slot machines

The dq flux linkage curves of Fig. 8.16 summarize why it is convenient to pass from the q = 2/5 winding to the q = 4/5 one is given with the help of. The key difference between the two PM-SyR machines is in their d-flux linkages (Fig. 8.16). It must be reminded that the d- component is the main flux linkage component, or the excitation one, so the one mostly influencing the output torque through the flux-linkage amplitude. In natural compensation conditions the torque is strictly proportional to the d- flux linkage, because the q- flux component is zero. The q = 4/5 machine has higher values of
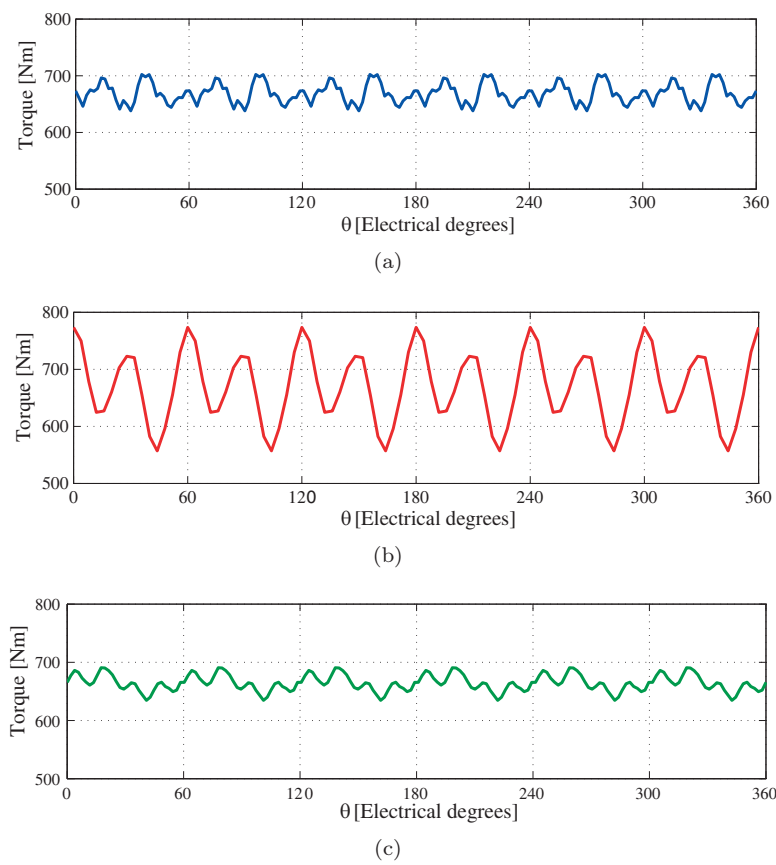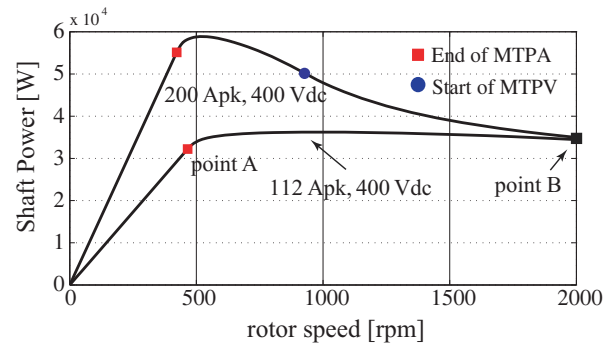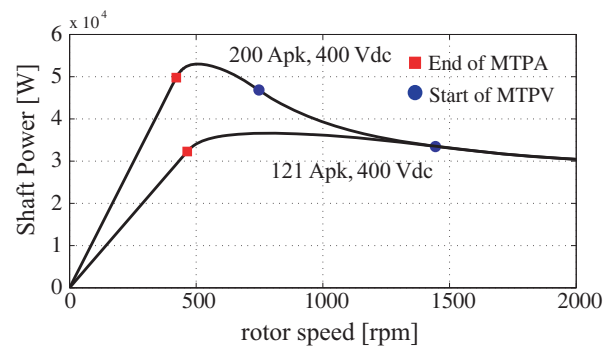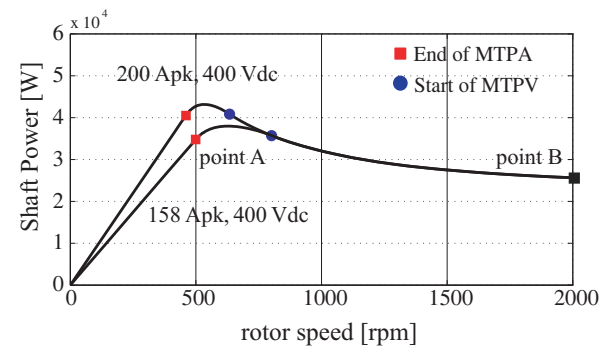
FIGURE 8.14: Torque vs rotor position for the PM-SyR solutions a) q = 3 machine;
b) q = 2/5 machine,

FIGURE 8.15: Power vs speed ; a) q=3 PMASR machines b) q=4/5 PMASR machines
c) q=2/5 PMASR machines.

d-flux linkage at all (i_d, i_q) conditions, and a higher flux in saturation. This to say that even a strong increase of the i_d current could not compensate for the lower excitation flux level of the q = 2/5.
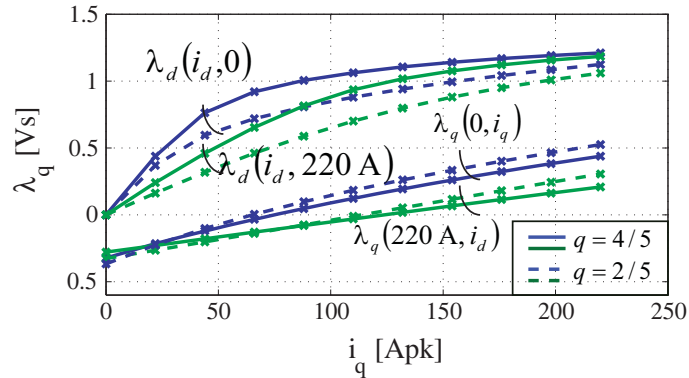

FIGURE 8.16: dq- flux linkage curves of the q = 2/5 and q = 4/5 machines.

The FEA results of Fig.8.13 give an intuitive justification of the poor d-axis magnetization condition of the tooth-wound machine (q = 2/5). The benchmark machine (Fig. 8.17a) has the rotor poles uniformly exploited. The q = 2/5 machine (Fig. 8.17b) has one rotor pole which is unexcited and other two out of 5 partially exploited. This is visible also on the stator, partially unloaded. The proposed q = 4/5 solution (Fig. 8.17c) has a good core exploitation, both on the stator and on the rotor.

8.5.3 Losses Comparison

The iron losses are FEA calculated at points A and B defined in Fig.8.15, with Magnet by Infolytica (http://www.infolytica.com). The loss components at point A are reported in Fig. 8.18a, dominated by the copper losses. Although the distributed winding machine has the higher phase resistance, its copper loss is the minimum one, thanks to the smaller current amplitude. The q = 4/5 has 13% more copper loss, from the aggregate higher current and the slightly lower resistance. The tooth-wound machine despite of the lowest resistance has 63% more copper loss than the benchmark because of the high current. This high copper loss is unlikely compatible with continuous operation, if the same cooling setup is used for the three machines. Plus, if the equal copper temperature simplification is removed, the copper loss difference is even amplified by the different copper temperatures. The thermal analysis in MotorSolve reports a maximum copper temperature of 118°C for the q = 3, 144 °C for the q = 4/5 and 240 °C for the q = 2/5 case. As said, the latter looks dramatically inadequate, from the thermal point of view. At maximum speed conditions (point B) the core loss are significant. For the fractional slot cases, also the ones on the rotor (Fig. 8.18b). The proposed q = 4/5 machine has the same rotor loss of the q = 2/5 one and the same stator loss of the q = 3 one.

8.5.4 Mild overlapped machines Conclusion

This work demonstrates that PM-SyR machines can be associated with success to specific fractional slot combinations such as the proposed 24/10 one. The presented 24/10 PM-SyR machine has torque and power figures that are comparable to the ones of the distributed windings benchmark. The proposed machine is easy to manufacture, even if not as advantageous as the tooth-wound coil ones. The points opened in the work are summarized here:

- The popular combination 12/10 is not competitive for PM-assisted SyR machine applications.

- Its poor performance mainly comes from the slot openings, that are large with respect to the rotor pole pitch. Plus, the multi-barrier rotor insulation is ineffective due to non-synchronous harmonics.

- The proposed 24/10 machine can have a performance that is close to the one of the distributed winding benchmark, provided that a greater quantity of magnets is used (+39% in the examples, according to the remanence ratio).

(a)

(b)

(c)
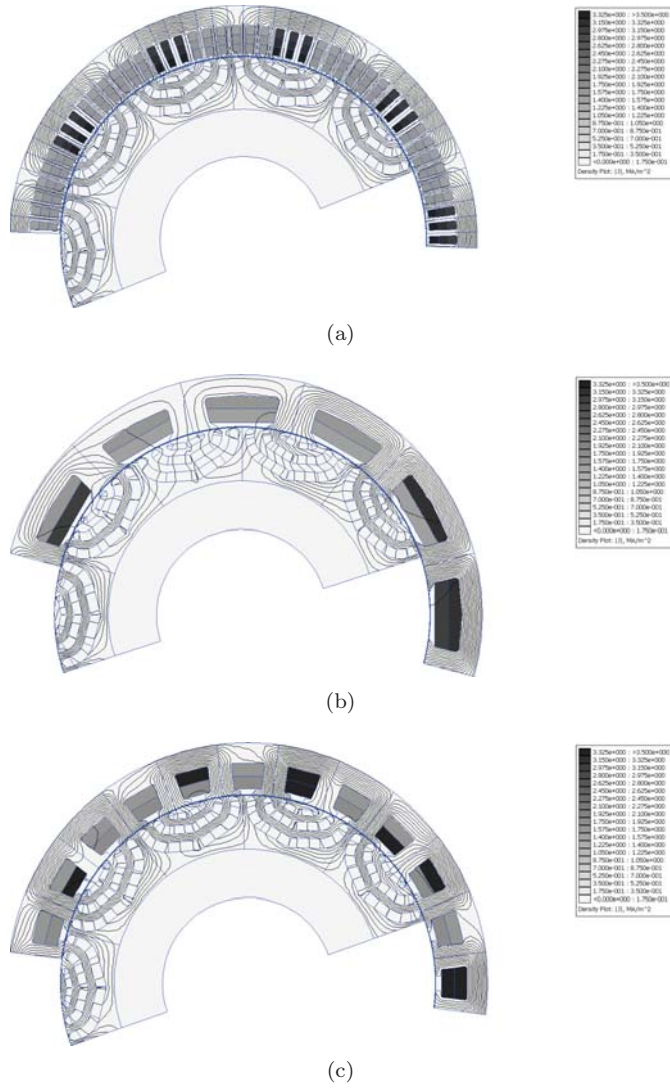
FIGURE 8.17: Flux density contours for the three PM-SyR machines supplied with d-axis current only. a) q = 3; b) q=2/5; c) proposed q=4/5 solution.
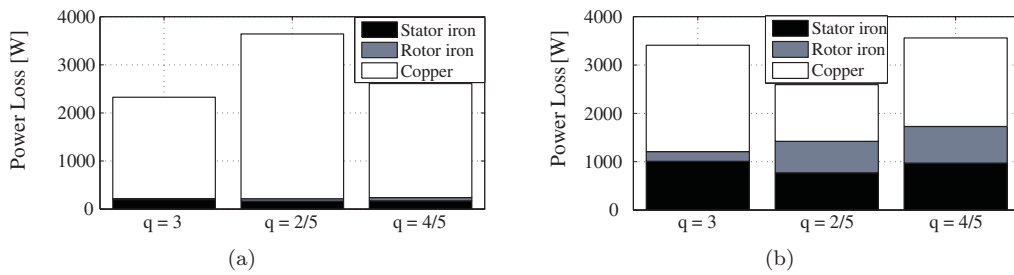
FIGURE 8.18: Segregation of the loss component of the three PM-SyR machines at a) rated torque, base speed and b) maximum speed, maximum power (different for the three).

- The improvements of the 24/10 respect to the 12/10 come from the smaller slot openings (versus the rotor pole pitch) and the polished MMF spectrum, that both increase the excitation flux linkage.The q- flux characteristic and the effectiveness of the insulation of the q-axis show minor improvements.

- The convenience in terms of end-winding length with respect to 90/10 is limited, due to the overlapping end-turns of the 24/10 windings. However, the copper loss reduction with respect to 12/10 is consistent, owing to the better Nm over Ampere coefficient.

- The core losses of the 24/10 machine are slightly worse than the ones of the two competitors.

- The proposed 24/10 machine is a promising trade-off solution in terms of performance and ease of manufacturing, still maintaining a good flux weakening behavior.

8.6 Publications

- M. Gamba; G. Pellegrino; A. Vagati ; A new PM-assisted Synchronous Reluctance machine with a nonconventional fractional slot per pole combination. In: Proceedings of, Brasov, Romania, maggio 2014. pp. 268-275

Chapter 9

Conclusions

The SyR technology was investigated comprehensively, focusing on design, simulation and testing aspects. The key contributions of the Thesis are:

- The flux barriers modelling simplification: the optimal number of parameters per barrier was investigated and validated. The findings tell that three-parameter barriers are optimal in terms of modelling accuracy versus complication, and two-parameter barriers are still acceptable. Such modelling approach is now part of SyRE.

- The design and testing of Line-Start SyR Machines. Although the machine type is not original, no design rules were reported in the literature. Besides breaking the ground of the machine design, including lumped parameters and transient FEA modelling approaches, a pivotal contribution was the prototype testing setup. A test rig was developed for the identification of load torque versus inertia pull-in capability of the two prototypes, using a load drive equipped with an angular accelerometer to emulate additional inertia of the load without adding inertial disks.

- The design and validation of non-conventional solutions, including one Ferrite-SyR Motor for light vehicular traction and one Fractional-Slot SyR machine prototype with minimized torque ripple and maximized torque.

- The original application of the mild-overlapped winding type to the SyR motor technology. This solution was accurately detailed in Chapter 8. It was shown the reluctance saving action of the new winding topology and the simplification of the winding structure, respect to the distributed ones. The higher reluctance behavior combined with the increment of the excitation flux linkage leads to improve the torque density and power factor, respect to the more popular Concentrated Winding solutions. The main disadvantage is represented by the fact that the mild solution is feasible only for higher number of poles. This means low speed machines, generally applied in direct drive solutions (elevators, wind turbines, drive wheels).

Bibliography

[1] Doherty R. E. and Nickle R. E. "Synchronous machines I — An extension of Blondel's two-reaction theory". In: *in Journal of the A.I.E.E., vol. 45, no. 10, pp. 974-987,* (Oct. 1926.doi: 10.1109/JAIEE.1926.6537307).

[2] Honsinger V. B. "Inherently Stable Reluctance Motors Having Improved Performance". In: *IEEE Transactions on Power Apparatus and Systems, vol. PAS-91, no. 4, pp. 1544-1554,* (July 1972. doi: 10.1109/TPAS.1972.293307).

[3] D. A. Staton W. L. Soong and T. J. E. Miller. "Design of a new axially-laminated interior permanent magnet motor". In: *in IEEE Transactions on Industry Applications, vol. 31, no. 2, pp. 358-367,* (Mar/Apr 1995. doi: 10.1109/28.370285).

[4] Vagati A. Franceschini G. Marongiu I. Troglia G.P. "Design criteria of high performance synchronous reluctance motors". In: *Industry Applications Society Annual Meeting, 1992., Conference Record of the 1992 IEEE, vol., no., pp.66-73 vol.1, 4-9,* (Oct 1992).

[5] N. Bianchi M. Barcaro and F. Magnussen. "Rotor Flux-Barrier Geometry Design to Reduce Stator Iron Losses in Synchronous IPM Motors Under FW Operations," in: *in IEEE Transactions on Industry Applications, vol. 46, no. 5, pp. 1950-1958,* (Sept.-Oct. 2010).

[6] N. Bianchi and S. Bolognani. "Parameters and volt-ampere ratings of a synchronous motor drive for flux-weakening applications". In: *IEEE Transactions on Power Electronics, vol. 12, no. 5, pp. 895-903,* (Sep 1997).

[7] Franceschini G. Vagati A. Fratta A. and Rosso P. "AC motors for high-performance drives: a design-based comparison". In: *IEEE Transactions on Industry Applications, vol. 32, no. 5, pp. 1211-1219* (Sep/Oct 1996. doi: 10.1109/28.536885).

[8] Soong W. L. and Miller T. J. E. "Field-weakening performance of brushless synchronous AC motor drives". In: *IEE Proceedings - Electric Power Applications, vol. 141, no. 6, pp. 331-340* (Nov 1994).

[9] IE4 – IE5 efficiency ABB and beyond without rare earth magnets. "www.abb.com". In: *Internet* (Nov 2016).

[10] NM. Degano H. Mahmoud N. Bianchi and C. Gerada. "Synchronous reluctance machine analytical model optimization and validation through finite element analysis". In: *2016 XXII International Conference on Electrical Machines (ICEM), Lausanne, pp. 585-591,* (2016).

[11] Valeria Hrabovcova Juha Pyrhonen Tapani Jokinen. "Design of Rotating Electrical Machines". In: *book, wiley ISBN: 978-0-470-74008-8* (February 2009).

[12] Barcaro M. and Bianchi N. "Interior PM machines using Ferrite to substitute rare-earth surface PM machines," in: *2012 XXth International Conference on Electrical Machines, Marseille, 2012, pp. 1339-1345.* (doi: 10.1109/ICElMach.2012.6350051).

[13] Honsinger V.B. "Permanent Magnet Machines: AsychronousOperation". In: *Power Apparatus and Systems, IEEE Transactions on, vol.PAS-99, no.4, pp.1503-1509* (July 1980).

[14] Kurihara K. Rahman M.A. "High-efficiency line-start interior permanent-magnet synchronous motors". In: *IndustryApplications, IEEE Transactions on, vol.40, no.3, pp. 789- 796,* (May-June 2004).

[15] VB Honsinger. "Synchronous Reluctance Motor". In: *US Patent 3,652,885,* (March 1972).

[16] Lawrenson P.J. Mathur R.M. "Pull-in criterion for reluctance motors". In: *Electrical Engineers, Proceedings of the Institution of,vol.120,no.9, pp.982-986,* (September 1973).

[17] Pettit R. Wagner P. Shaw K. "Synchronous AC motors for process control over wide speed ranges". In: *Textile Industry Technical Conference, 1988., IEEE 1988 Annual , vol., no., pp.6/1-6/8, 4-5,* (May 1988).

[18] Gamba M. Pellegrino G. Vagati A. Villata F. "Design of a line-start synchronous reluctance motor," in: *Electric Machines and Drives Conference (IEMDC), 2013 IEEE International , vol., no., pp.648,655* (12-15 May 2013).

[19] Boroujeni S.T. Bianchi N. Alberti L. "Fast Estimation of Line-Start Reluctance Machine Parameters by Finite Element Analysis". In: *Energy Conversion, IEEE Transactions on , vol.26, no.1, pp.1* (8 March 2011).

[20] D. Mingardi and N. Bianchi. "FE-aided analytical method to predict the capabilities of line-start synchronous motors". In: *2014 IEEE Energy Conversion Congress and Exposition (ECCE), Pittsburgh, PA, pp. 5123-5130.* (2014).

[21] https://www.hbm.com/en. In: *On-line available* (2017).

[22] KSB company. "https://www.ksb.com/," in: *Review December 2016* (December 2016).

[23] Gamba M. Armando E. Pellegrino G. Vagati A. Janjic B. and Schaab J. "Line-start synchronous reluctance motors: Design guidelines and testing via active inertia emulation". In: *2015 IEEE Energy Conversion Congress and Exposition (ECCE), Montreal.* (QC, 2015, pp. 4820-4827.).

[24] Armando E. Bojoi R.I. Guglielmi P. Pellegrino G. Pastorelli M. "Experimental Identification of the Magnetic Model of Synchronous Machines". In: *Industry Applications, IEEE Transactions on , vol.49, no.5, pp.2116,2125* (Sept.-Oct. 2013).

[25] Campbell S. Burress T. "Benchmarking EV and HEV power electronics and electric machines". In: *in Transportation Electrification Conference and Expo (ITEC), 2013 IEEE, vol., no., pp.1-6, 16-19,* (June 2013).

[26] Campbell S. Burress T. "Evaluation of the 2010 Toyota Prius hybrid synergy drive system". In: *Energy Efficiency and Renewable Energy FreedomCAR and Vehicle Technologies Vehicle Systems Team,* (March 2011).

[27] B. Guan H. Cai and L. Xu. "Low-Cost Ferrite PM-Assisted Synchronous Reluctance Machine for Electric Vehicles". In: *in IEEE Transactions on Industrial Electronics, vol. 61, no. 10, pp. 5741-5748,* (Oct. 2014).

[28] M. Sanada M. Obata S. Morimoto and Y. Inoue. "Performance of PMASynRM With Ferrite Magnets for EV/HEV Applications Considering Productivity," in: *in IEEE Transactions on Industry Applications, vol. 50, no. 4, pp. 2427-2435,* (July-Aug. 2014.).

[29] N. Bianchi S. Bolognani E. Carraro M. Castiello and E. Fornasiero. "Electric Vehicle Traction Based on Synchronous Reluctance Motors". In: *IEEE Transactions on Industry Applications, vol. 52, no. 6, pp. 4762-4769,* (Nov.-Dec. 2016).

[30] Jurkovic S. Rahman K. Bae B. Patel N. Savagian P. "Next generation Chevy volt electric machines, design, optimization and control for performance and rare-earth mitigation," in: *in Energy Conversion Congress and Exposition (ECCE), 2015 IEEE, vol., no., pp.5219-5226, 20-24.* (Sept. 2015.).

[31] Boazzo B. Vagati A. Pellegrino G. Armando E. Guglielmi P. "Multipolar Ferrite-Assisted Synchronous Reluctance Machines: A General Design Approach," in: *in Industrial Electronics, IEEE Transactions on, vol.62, no.2, pp.832-845,* (Feb. 2015.).

[32] Pellegrino G. Vagati A. Guglielmi P. and Boazzo B. "Performance Comparison Between Surface-Mounted and Interior PM Motor Drives for Electric Vehicle Application," in: *in IEEE Transactions on Industrial Electronics, vol. 59, no. 2, pp. 803-811.* (Feb. 2012.).

[33] Cupertino F. et al. "Syre - Synchronous Reluctance (machines) – evolution," in: *[Online]. Available: http://sourceforge.net/projects/syr-e/ .* (Accessed: 10- Nov- 2015).

[34] David Wenzhong Gao Chris Mi M. Abul Masrur. "Hybrid Electric Vehicles: Principles and Applications with Practical Perspectives". In: *WILEY* (23 maggio 2011).

[35] N. Bianchi and S. Bolognani. "Design optimisation of electric motors by genetic algorithms". In: *IEE Proceedings - Electric Power Applications, vol. 145, no. 5, pp. 475-483,* (Sep 1998).

[36] Kamper M.J. van der Merwe F.S. Williamson S. "Direct finite element design optimisation of the cageless reluctance synchronous machine". In: *IEEE Transactions on Energy Conversion, Vol. 11, n.3,* (Sept 1996).

[37]   Yao D. Ionel D.M. "A Review of Recent Developments in Electrical Machine Design Optimiza-
       tion Methods With a Permanent-Magnet Synchronous Motor Benchmark Study". In: *Industry
       Applications, IEEE Transactions on , vol.49, no.3, pp.1268,1275* (May-June 2013).

[38]   Pellegrino G. Cupertino F. "FEA-based multi-objective optimization of IPM motor design in-
       cluding rotor losses". In: *Energy Conversion Congress and Exposition (ECCE), 2010 IEEE ,
       vol., no., pp.3659-3666* (12-16 Sept. 2010).

[39]   Cupertino F. Pellegrino G. Armando E. Gerada C. "A SyR and IPM machine design methodology
       assisted by optimization algorithms". In: *Energy Conversion Congress and Exposition (ECCE),
       2012 IEEE , vol., no.* (15-20 Sept. 2012).

[40]   Pellegrino G. Cupertino F. Gerada C. "Barriers shapes and minimum set of rotor parameters in
       the automated design of Synchronous Reluctance machines". In: *Electric Machines and Drives
       Conference (IEMDC), 2013 IEEE International , vol., no., pp.1204,1210* (12-15 May 2013).

[41]   Rajabi Moghaddam. "Synchronous Reluctance Machine (SynRM) in Variable Speed Drives
       (VSD) Applications". In: *. (Doctoral dissertation). Stockholm: KTH Royal Institute of Tech-
       nology, [Online] http://urn.kb.se/resolve?urn=urn:nbn:se:kth:diva-33804* ([1 October 2015]).

[42]   Francheschini G. Vagati A. Pastorelli M. and Petrache S. C. "Design of low-torque-ripple syn-
       chronous reluctance motors". In: *in IEEE Transactions on Industry Applications, vol. 34, no. 4,
       pp. 758-765* (Jul/Aug 1998).

[43]   A. Boglietti A. Cavagnino M. Lazzari and M. Pastorelli. "A simplified thermal model for variable-
       speed self-cooled industrial induction motor," in: *IEEE Transactions on Industry Applications,
       vol. 39, no. 4, pp. 945-952,* (July-Aug. 2003.).

[44]   L. Alberti and N. Bianchi. "A Coupled Thermal–Electromagnetic Analysis for a Rapid and
       Accurate Prediction of IM Performance". In: *IEEE Transactions on Industrial Electronics, vol.
       55, no. 10, pp. 3575-3582,* (Oct. 2008).

[45]   D. Staton A. Boglietti and A. Cavagnino. "Solving the More Difficult Aspects of Electric Mo-
       tor Thermal Analysis in Small and Medium Size Industrial Induction Motors," in: *in IEEE
       Transactions on Energy Conversion, vol. 20, no. 3, pp. 620-628,* (Sept. 2005.).

[46]   Cros J. Viarouge P. "Synthesis of high performance PM motors with concentrated windings".
       In: *Energy Conversion, IEEE Transaction on, vol. 17, pp. 248-253, 2002.* (Jan. 2010).

[47]   M. Gamba G. Pellegrino and A. Vagati. "A new PM-assisted Synchronous Reluctance machine
       with a nonconventional fractional slot per pole combination," in: *2014 International Conference
       on Optimization of Electrical and Electronic Equipment (OPTIM), Bran,* (2014).

[48]   N. Bianchi S. Bolognani and M. Dai Pre. "Magnetic Loading of Fractional-Slot Three-Phase PM
       Motors With Nonoverlapped Coils". In: *IEEE Transactions on Industry Applications, vol. 44,
       no. 5, pp. 1513-1521,* (Sept.-Oct. 2008).

[49]   L. Alberti M. Barcaro and N. Bianchi. "Design of a Low-Torque-Ripple Fractional-Slot Interior
       Permanent-Magnet Motor". In: *IEEE Transactions on Industry Applications, vol. 50, no. 3, pp.
       1801-1808,* (May-June 2014).

[50]   M. Barcaro and N. Bianchi. "Torque ripple reduction in fractional-slot Interior PM machines
       optimizing the flux-barrier geometries". In: *2012 XXth International Conference on Electrical
       Machines, Marseille, pp. 1496-1502,* (2012).

[51]   EL-Refaie A.M. "Fractional-Slot Concentrated-Windings Synchronous Permanent Magnet Ma-
       chines: Opportunities and Challenges". In: *Industrial Electronics, IEEE Transactions on , vol.57,
       no.1, pp.107,121* (Jan. 2010).

[52]   Bianchi N. Bolognani S. Pre' M.D. Grezzani G. "Design considerations for fractional-slot winding
       configurations of synchronous machines". In: *Industry Applications, IEEE Transactions on ,
       vol.42, no.4, pp.997,1006* (July-Aug. 2006).

[53]   EL-Refaie A.M. Jahns T.M. "Optimal flux weakening in surface PM machines using concentrated
       windings". In: *Industry Applications Conference, 2004. 39th IAS Annual Meeting. Conference
       Record of the 2004 IEEE , vol.2, pp.1038,1047 vol.2,* (3-7 Oct. 2004).

[54]   Reddy P.B. EL-Refaie A.M. Kum-Kang Huh Tangudu J.K. Jahns T.M. "Comparison of Interior
       and Surface PM Machines Equipped With Fractional-Slot Concentrated Windings for Hybrid
       Traction Applications". In: *Energy Conversion, IEEE Transactions on , vol.27, no.3, pp.593,602,*
       (Sept. 2012).

[55] Tangudu J.K. Jahns T.M. "Comparison of interior PM machines with concentrated and distributed stator windings for traction applications". In: *Vehicle Power and Propulsion Conference (VPPC), 2011 IEEE , pp.1,8, 6-9,* (Sept. 2011).

[56] Dajaku G. Gerling D. "A Novel 24-Slots/10-Poles Winding Topology for Electric Machines". In: *Electric Machines and Drives Conference (IEMDC), 2011 IEEE International, pp.65,70,* (15-18 May 2011).

[57] Guglielmi P. Boazzo B. Armando E. Pellegrino G. Vagati A. "Permanent-Magnet Minimization in PM-Assisted Synchronous Reluctance Motors for Wide Speed Range". In: *Industry Applications, IEEE Transactions on , vol.49, no.1, pp.31,41,* (Jan.-Feb. 2013).

[58] Pellegrino G. Vagati A. Guglielmi P. "Design Tradeoffs Between Constant Power Speed Range, Uncontrolled Generator Operation, and Rated Current of IPM Motor Drives". In: *Industry Applications, IEEE Transactions on , vol.47, no.5, pp.1995,2003,* (Sept.-Oct. 2011).

[59] Alberti L. Barcaro M. Bianchi N. "Design of a Low Torque Ripple Fractional-slot Interior Permanent Magnet Motor". In: *in IEEE Transactions on Industry Applications, vol. 50, no. 3, pp. 1801-1808* (May-June 2014).

[60] John Lowry James Larminie. "Electric Vehicle Technology Explained". In: *book, wiley ISBN 978-0-470-09069-5* (December 2003).

[61] Miller T.J.E. "Synchronization of Line-Start Permanent-Magnet AC Motors". In: *Power Engineering Review, IEEE, vol.PER-4, no.7, pp.57-58* (July 1984).

[62] R.M. Lawrenson P.J. Mathur. "Pull-in criterion for reluctance motors". In: *Electrical Engineers, Proceedings of the Institution of,vol.120,no.9, pp.982-986* (September 1973).

[63] David Meeker. "Finite Element Method Magnetics". In: *Ver. 4.2 User's Manual, February 5, 2009, [Online] available: http://www.femm.info/Archives/doc/manual.pdf* (2009).

[64] Rajabi Moghaddam. "Synchronous Reluctance Machine (SynRM) in Variable Speed Drives (VSD) Applications". In: *(Doctoral dissertation). Stockholm: KTH Royal Institute of Technology, [Online] http://urn.kb.se/resolve?urn=urn:nbn:se:kth:diva-33804* (1 October 2015).

[65] K.J. Binns P.J. Lawrenson C.W. Trowbridge. "The analytical and numerical solution of electric and magnetic fields". In: *John Wiley and Sons* (copyright 1992).

[66] Zarko D. Ban D. Lipo T.A. "Design optimization of interior permanent magnet (IPM) motors with maximized torque output in the entire speed range". In: *Power Electronics and Applications* (2005 European Conference on).

[67] Dajaku G. Gerling D. "A novel tooth concentrated winding with low space harmonic contents". In: *Electric Machines and Drives Conference (IEMDC), 2013 IEEE International, pp.755,760,* (12-15 May 2013).

[68] Dajaku G. "Elektrische Maschine". In: *German patent application No.102008 051 047 A1* (2008).

[69] J. Cros and P. Viarouge. "Synthesis of high performance PM motors with concentrated windings," in: *IEEE Transactions on Energy Conversion, vol. 17, no. 2, pp. 248-253,* (Jun 2002.).